Title
Detonation Initiation, Propagation, and Suppression

Author
Ryu, Je Ir

Publication Date
2018

Peer reviewed|Thesis/dissertation

Detonation Initiation, Propagation, and Suppression

by

Je Ir Ryu

A dissertation submitted in partial satisfaction of the

requirements for the degree of

Doctor of Philosophy

in

Engineering – Mechanical Engineering

and the Designated Emphasis

in

Energy Science and Technology

in the

Graduate Division

of the

University of California, Berkeley

Committee in charge:

Professor Jyh-Yuan Chen, Chair
Professor Carlos Fernandez-Pello
Professor Van P. Carey
Professor Mark T. Stacey

Fall 2018

Detonation Initiation, Propagation, and Suppression

Abstract

Detonation Initiation, Propagation, and Suppression

by

Je Ir Ryu

Doctor of Philosophy in Engineering – Mechanical Engineering

with the Designated Emphasis

in

Energy Science and Technology

University of California, Berkeley

Professor Jyh-Yuan Chen, Chair

Understanding the fundamental processes of detonation is essential for both energy and safety issues. The rapid energy conversion characteristic of detonation is significantly useful in industrial and military applications, such as detonation engines and high explosives. On the other side, this characteristic of detonation is not preferred in the field of safety engineering. Detonations with violent pressure waves frequently cause catastrophic human casualties and property damages.

This dissertation presents theoretical and numerical studies on detonation initiation, propagation, and suppression. Multiple numerical tools are employed to study detonation phenomena: a toolbox to calculate the steady state homogeneous detonation properties, a simplified unsteady compressible solver for Lagrangian equations to simulate detonation behaviors as a primary stage, and a compressible multi-component reacting flow solver to perform transient simulations of the detonation phenomena in detail.

Several methods to predict the occurrence of detonation initiation and deflagration to detonation transition are developed. Transient and integral reactivity gradient methods are proposed and evaluated on the basis of the Zel'dovich reactivity gradient theory. Prediction models of detonation initiation developed from machine learning techniques are also presented. Potential applications of statistical learning models with the conventional numerical simulations are discussed.

Effects of fuel-stratification on detonation propagation are identified by detailed numerical simulations. Both the leading shock pressure and detonation propagation speed in

the fuel-stratified layer are compared to the corresponding homogeneous Chapman-Jouguet detonation properties. The shock reflection and transmission theory, and the Zel'dovich-Neumann-Döring detonation structure model are employed to describe deficits or surpluses in properties of stratified detonation. The overall mechanism of stratified detonation propagations is also proposed.

Detonation suppression in water vapor concentration gradients is investigated by the transient numerical simulations with various water vapor concentrations and thicknesses of the gradient layer. From the simulations, three combustion modes are observed: 1) normal detonation propagation, 2) detonation mitigation and re-initiation, 3) detonation suppression. The separation of leading shock and reaction front is the main cause of a detonation suppression. A regime map for limits of each mode is introduced showing that the mode depends on the normalized ignition delay time including shock reflection effect and the ratio of the gradient layer thickness to the detonation induction length. The transient reactivity gradient method is employed to understand the detonation re-initiation process after the mitigation of the initial detonation.

To my parents, Sun I and Chyung Hyeon

Contents

List of Figures

List of Tables

Nomenclature

Abbreviations

A-SURF Adaptive Simulation of Unsteady Reactive Flow

AMR Adaptive mesh refinement

CART Classification and regression trees

CFL Courant–Friedrichs–Lewy

CJ Chapman-Jouguet

DDT Deflagration to detonation transition

HD Homogeneous Chapman-Jouguet detonation

LS Leading shock

MPI Message Passing Interface

ODE Ordinary differential equation

PDE Partial differential equation

RF Reaction front

SD Stratified detonation

SLED Solver for Lagrangian Equations of Deflagration/Detonation

STP Standard temperature and pressure

VN von Neumann

ZND Zel'dovich-Neumann-Döring

Greek Symbols

$\dot{\Omega}_i$ Mass fraction production rate of species i

$\dot{\sigma}$ Thermicity

η Ratio of gradient layer thickness to induction length

γ Adiabatic index

λ Thermal conductivity

μ Dynamic viscosity

Φ Viscous dissipation term

ϕ Equivalence ratio

ϕ_1 Equivalence ratio of unburnt mixture before stratification

ϕ_2 Equivalence ratio of unburnt mixture after stratification

ϕ_i Equivalence ratio at induction zone

ρ Density

ρ_j Density of medium j

τ Viscous stress

τ_i Ignition delay time

τ_t Ignition delay time of mixture under transmitted shock

τ_{VN} Ignition delay time of mixture at VN state

ξ Normalized reactivity gradient

ξ_l Lower limiting value of ξ for developing detonation

ξ_u Upper limiting value of ξ for developing detonation

ξ_{eff} Integral normalized reactivity gradient

ζ Normalized ignition delay time including shock reflection effect

Roman Symbols

ΔM Lagrangian invariant mass of a fluid element

ΔT Temperature difference of hot spot

Δt Size of time step

ΔT^*	Normalized temperature difference of hot spot
$\dot{m}_i'''$	Mass production rate per unit volume of species i
$\dot{m}''$	Mass flux
$\dot{Q}$	Heat release rate per unit volume
$\dot{q}''$	Heat flux
A	Artificial viscosity term
a	Sound speed
a_f	Frozen sound speed
a_j	Sound speed of medium j
c	Constant
c_p	Specific heat at constant pressure
c_R	Pressure reflection coefficient
c_T	Pressure transmission coefficient
c_v	Specific heat at constant volume
$c_{p,i}$	Specific heat at constant pressure of species i
D	Detonation propagation speed
d	Size of water vapor gradient layer
d_s	Size of fuel-stratification layer
e	Internal energy per unit mass
E_t	Total energy per unit volume
h_i	Enthalpy of species i
h_i^0	Standard enthalpy of formation of species i
I	Specific acoustic impedance
I_j	Specific acoustic impedance of medium j
L	Characteristic location

l	Mesh point
L_d	Domain size
l_{ind}	Induction length
M	Lagrangian invariant mass
N	Total number of species
n	Time step
P	Pressure
P'	Acoustic pressure
P'_I	Acoustic pressure of incident wave
P'_R	Acoustic pressure of reflected wave
P'_T	Acoustic pressure of transmitted wave
P_{LS}	Leading shock spike pressure
P_{VN}	von Neumann spike pressure
Pr	Probability
q	Heat release per unit mass
R	Ideal gas constant
r	Location in the spherical domain
r_h	Size of hot spot
S_L	Laminar flame speed
S_{CJ}	Chapman-Jouguet speed
S_{LS}	Leading shock front speed
S_{RF}	Reaction front propagation speed
S_t	Speed of transmitted shock front
T	Temperature
t	Time

T_0	Standard temperature
T_h	Temperature of hot spot center
T_{VN}	von Neumann temperature
u	Fluid velocity
u_I	Incident fluid speed
u_i^*	Diffusion velocity of species i
u_R	Reflected fluid speed
u_r	Reaction front propagation speed relative to the unburnt mixture
u_T	Transmitted fluid speed
u_{eff}	Effective reaction front propagation speed
w	Normal velocity in the shock-fixed frame
x	Location in planar domain
X_i	Mole fraction of species i
Y	Dependent variable
Y_i	Mass fraction of species i
Z	Negative exponentiation of the logistic function
z	Ratio of specific acoustic impedances of two media

Acknowledgments

Many people have contributed to my doctoral research, and I could not accomplish without their support and help.

I would like to express my most sincere gratitude to my advisor, Professor Jyh-Yuan Chen, for his guidance and support. Professor Chen has trained me to become an independent but collaborative researcher. He has provided me not only a strong foundation of my research area, but also a great educational philosophy. I feel very fortunate to have him as my research advisor. I would like to thank Professor Carlos Fernandez-Pello, who has served on my qualifying exam chair and dissertation committee. His invaluable advice and continuous encouragement are greatly appreciated. I also learned how to share my knowledge while I was his teaching assistant. Both Professor Van P. Carey and Professor Mark T. Stacey have served on my qualifying exam committee and dissertation committee, and I would like to thank them for their support and help. Professor Carey has advised me on my research and the academic life. He took me as his teaching assistant, and supported my doctoral study. Professor Stacey has provided me a wider view on my research, and I could extend my research world with his encouragement. I thank Professor Richard Klein for serving on my qualifying exam committee and his teaching on numerical methods. I also would like to thank Professor Zheng Chen at Peking University for providing the numerical solver A-SURF.

I acknowledge the Ilju Academy and Culture Foundation for four-year scholarship and the Jane Lewis endowment for one-year fellowship. I could concentrate on my doctoral research with their financial support.

It was my great fortune to have great lab mates: Benjamin Wolk, Tiernan Casey, Daniel Pineda, Yulin Chen, Xian Shi, Yumin Huang, Charles Scudiere, Alex Frank, Jorge Moreno, Sirui Fu, and Santiago Mejia from Combustion Modeling Laboratory, Jim Oreluk, Wenyu Li and Zhenyuan Liu from Professor Micheal Frenklach's lab, James Urban and Maria Thomsen-Solis from Combustion Fire Processes Laboratory, Miguel Sierra Aznar from Combustion Analysis Laboratory, and visiting scholars and students, Fredrik Grøvdal, Tao Chen, and Shenghao Yu. I enjoyed this friendly and professional environment, and proud of being a member of this great team.

Nothing can express my gratitude enough to my parents, Chyung Hyeon Ryu and Sun I Li, and my brother, Jeweon Ryu. Their infinite trust and love made it possible for me to finish my doctoral study, and I love them. I am also sincerely grateful to my relatives and friends, and I could not survive without their support and care. Lastly, my wife, Haewon Kwon, has been always walking together with me, and I could be more mature with her. Her endless love and encouragement made this dissertation complete.

Chapter 1

Introduction

1.1 Motivation

One of forms of combustion called detonation is an abrupt and violent chemical reaction propagation through the explosive by strong compression, but not diffusion processes. Understanding this form of combustion is of interest in energy and safety applications due to its rapid energy conversion characteristic. For example, the energy conversion rate of a good solid explosive by a detonation is on the order of 10^{10} W/cm^2 in the detonation front (Fickett and Davis, 2000). The total electricity generation of the Unite States at utility scale facilities in 2016 is about 10^{12} W (U.S. Energy Information Administration, 2017), and a 10 cm $\times$ 10 cm detonation front can convert the same amount of power level. In a comparison with typical 100 kW automobile engine, a hundred thousand cars can be run at the same time with the power from a 1 cm^2 detonation front.

Energy science and technology

As the rapid energy conversion characteristic of detonation is significantly useful in industrial and military applications, the detonation phenomena have been studied actively to develop better energy conversion systems and explosives.

One of approaches to utilize the rapid energy conversion characteristic is directly utilizing detonation waves to the engine. In the early work of Zel'dovich (1940b), a thermodynamic analysis of the cycle efficiency with detonation was presented, and he proved that the efficiency of detonation combustion can be higher than that of constant-volume combustion without detonation. Several types of detonation engines have been developed, and most promising types are pulse and rotating detonation engines. In pulse detonation engine cycles, the engine is pulsed as the mixture should be refilled each cycle, while the rotating detonation engine uses an annular chamber and the detonation wave rotates transversely to create a continuous axial flow. The reviews by Bussing and Pappas (1996) and Rankin et al. (2017) provide more details about pulse and rotating detonation engines, respectively.

For the applications of detonation such as high explosives, detonation properties have been measured and calculated by many researchers. For example, Urtiew and Oppenheim (1966) developed experimental techniques to measure detonation properties of hydrogen/oxygen mixtures. Sućeska (1999) numerically calculated the detonation properties of typical explosives such as TNT (2,4,6-trinitrotoluene), RDX (1,3,5-trinitroperhydro-1,3,5-triazine), HMX (1,3,5,7-tetranitro-1,3,5,7-tetrazocine), and PETN (pentaerythritol tetranitrate). Recently, density functional theory calculation was used to develop a new explosive which has better detonation properties by Jeong (2018).

Explosion safety

On the other side, researchers also have been investigated detonation phenomena to avoid or suppress detonation for safety reasons. As a detonation wave propagates rapidly and accompanies strong shock waves, an explosion with detonation wave is extremely dangerous. Therefore, avoiding detonation during accidental explosions is crucial to reduce human and property damage.

One of the large scale examples is the Fukushima-Daiichi nuclear power plant accident in 2011. Multiple studies (Gauntt et al., 2012; International Atomic Energy Agency, 2015; Yanez et al., 2015; Xiao et al., 2017) showed that a detonation of hydrogen was initiated and ruptured the containment. Another example is an explosion accident in the natural gas pipelines. From 2013 to 2017, 60 fatalities and 304 injuries were associated with pipeline accidents (Pipeline and Hazardous Materials Safety Administration, 2018). To reduce the volume of natural gas significantly, highly pressurized natural gas is transported through the interstate pipelines. This may cause a hazardous explosion even with a small defect of the pipelines. If natural gas in the pipeline is disseminated and ignited in the air, a fatal incident with detonation may occur in some conditions.

In the small scale, many researchers (Peters et al., 2013; Wang et al., 2015a,b; Qi et al., 2015a,b; Robert et al., 2015) have been studied on abnormal high pressure peak called super-knock in internal combustion engines. For downsized and high boosted direct injection engines, super-knock phenomena were observed, and the engine components were easily damaged due to the high pressure peak. Multiple experiments (Wang et al., 2015a,b; Qi et al., 2015a,b) showed that the phenomena were due to detonation initiation.

Therefore, understanding initiation, propagation, and suppression of detonation is crucial in order to utilize detonation characteristics for energy science and technology, and solve safety issues in accidental explosions.

1.2 Structure of dissertation

This dissertation presents theoretical and numerical studies on detonation initiation, propagation, and suppression. The structure of this dissertation is organized as follows:

1. The first chapter starts with the motivation of detonation research. Detonation characteristics are presented, and applications of these characteristics in energy science and explosion safety are introduced. Then, the structure and contributions of this dissertation are described. Lastly, some fundamentals of detonation are presented: definition of important terms, governing equations, the Chapman-Jouguet solution, and the Zel'dovich-Neumann-Döring structure.

2. The second chapter presents numerical solvers used in this research. First, a steady-state one dimensional toolbox is introduced to calculate the Chapman-Jouguet solution and the Zel'dovich-Neumann-Döring structure for reference. A simplified transient solver for Lagrangian equations are described for trial simulations. Then, a description of a sophisticated transient solver with transport models is provided.

3. The third chapter discusses initiation processes of detonation. The Zel'dovich reactivity gradient theory is introduced. Transient and integral reactivity gradient methods are presented with multiple examples. Some prediction models of detonation initiation developed from machine learning techniques are evaluated.

4. The fourth chapter focuses on detonation propagation in fuel-stratification layers. The detonation propagation speed and the leading shock pressure are evaluated both in the lean-to-rich and rich-to-lean stratification for different stratification layer sizes and fuels. Using acoustic theory and detonation structure model, the phenomena are analyzed and the overall mechanism is proposed.

5. The fifth chapter discusses the mitigation and suppression of detonation waves propagating into the water vapor gradient layer. Three modes of detonation responses are introduced: normal propagation, mitigation and re-initiation, and suppression. Acoustic theory and transient reactivity gradient method are employed to explain each mode.

6. The last chapter concludes the dissertation with summarized numerical simulation results and theoretical analysis. A discussion is presented to extend this research, and some directions for future work are suggested.

7. The appendices provide detailed derivations of equations used in this dissertation. The first appendix contains derivations of the Rayleigh line, the Hugoniot curve, the Chapman-Jouguet condition, and the Chapman-Jouguet properties. The second appendix includes the derivations of shock reflection and transmission equations from acoustic theory.

1.3 Dissertation contributions

Contributions of the work presented in this dissertation to understand the detonation phenomena for higher efficiency energy use and accidental explosion safety include the following:

- Transient and integral reactivity gradient methods are proposed for better predictions of detonation initiation occurrence. These methods promote the in-depth understanding of detonation initiation mechanisms including deflagration to detonation transitions, and can be utilized to initiate or avoid a detonation easily for energy or safety use, respectively.
- Numerical investigations extend the understanding of detonation propagation processes in the fuel-stratification layer and water vapor gradient layer. The numerical tools and analysis used in this dissertation can be also utilized in other detonation-related research.
- Models for detonation propagation and suppression are developed. The model of overall stratified detonation propagation mechanism using acoustic theory and the detonation structure is the first model to explain the transient states of stratified detonation propagation. The detonation suppression model with two non-dimensional parameters is the first attempt to quantitatively analyze detonation suppression phenomena. These models suggest primary analyzing tools for applications.
- Appropriate scientific context for theoretical and numerical techniques to study detonation phenomena is provided.

1.4 Fundamentals of detonation

Definitions

The investigation of detonation processes requires some fundamental definitions, as some technical terms are not very clear and confused in the literature. Definitions described in this section will be used throughout this dissertation.

Different flame propagation modes are possible in a premixed mixture. The mixture can be liquid or solid, but this thesis will focus on gaseous mixtures. A normal premixed flame is called a *deflagration* or *deflagration wave*, as the burnt mixture expands after the flame propagation. A deflagration is through subsonic propagation by diffusion of heat and mass. The reactant in front of the flame is heated by heat and mass transfer, so the flame propagates through the reactant.

Another flame propagation mode with higher pressure peak is called a *detonation* or *detonation wave*. As a detonation is the supersonic flame propagation, a leading shock forms in front of the flame. The flame propagates through the unburnt mixture by adiabatic

compression and heating of the leading shock. In the detonation front, the reaction front propagation wave resonates with the leading shock, so the pressure rise from a detonation is much higher (typically, more than ten times) than that from a deflagration.

An *explosion* is a general term for the extreme exothermic reaction with rapid temperature and pressure increases. The explosion can accompany deflagration, detonation, or both. In some literature, an explosion implies simultaneous ignition in the whole domain, i.e., infinitely fast flame propagation. To avoid confusion, this simultaneous ignition phenomenon will be called a *thermal explosion* in this dissertation.

Basic equations

The basic equations describing a one-dimensional detonation were presented by Rankine (1870) and Hugoniot (1889). These equations are called Rankine-Hugoniot conditions, and available in common detonation textbooks (Fickett and Davis, 2000; Lee, 2008). The equations and analysis assume the following:

- The flow is steady and laminar.
- The shock compression and reaction are completed in the detonation front, so the gradients of the state variables in the burnt and unburnt sides are infinitely small.
- Both burnt and unburnt mixtures are ideal gases with constant specific heat.

The schematic of the system is as shown in Figure 1.1a. In the figure, the detonation propagates into unburnt mixture with the detonation propagation speed, D. P, T, ρ, and u are the pressure, temperature, density, and fluid velocity of the mixture, respectively. The subscripts b and u denote burnt and unburnt states, respectively. Initially, the unburnt mixture is at rest, i.e., $u_u = 0$. It is convenient to use relative velocities to the detonation wave, and the schematic of the system with relative velocities are shown in Figure 1.1b.

Then, the conservation equations of mass, momentum and energy for the system are:

$$\rho_b(u_b - D) = \rho_u(-D), \tag{1.1}$$

$$P_b + \rho_b(u_b - D)^2 = P_u + \rho_u(-D)^2, \tag{1.2}$$

$$c_p T_b + \frac{(u_b - D)^2}{2} = c_p T_u + \frac{(-D)^2}{2} + q, \tag{1.3}$$

where c_p is the specific heat at constant pressure, and q is the heat release per unit mass which can be calculated from the difference between the standard enthalpies of formation of unburnt and burnt mixtures.

The properties in unburnt side, P_u, T_u, and ρ_u, are generally known, so the equation of state only in burnt side is needed:

$$P_b = \rho_b R T_b, \tag{1.4}$$

where R is the ideal gas constant.

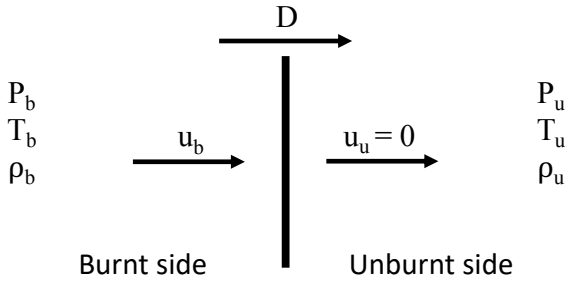

(a) Lab frame

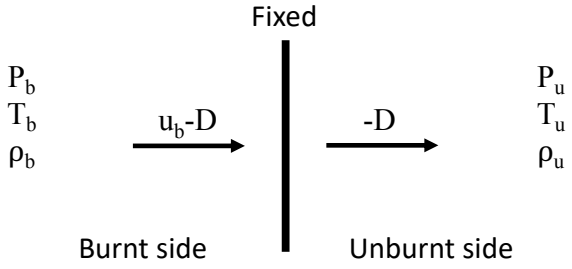

(b) Detonation wave fixed frame

Figure 1.1: Schematics of 1-D detonation system for basic equations.

Chapman-Jouguet solution

In Equations 1.1, 1.2, 1.3, and 1.4, known properties are c_p, q, and thermodynamic properties in unburnt side, so there are five unknowns, P_b, T_b, ρ_b, u_b, and D. However, as the system has four equations, no unique solution exists. The possible solution sets can be derived from a well-know graphical method, and the stable solution is called the Chapman-Jouguet (CJ) solution (Chapman, 1899; Jouguet, 1905, 1906). This is also widely explained in most detonation textbooks such as Fickett and Davis (2000) and Lee (2008).

Combining Equations 1.1 and 1.2 and eliminating u_b and D in the equation, a straight line in P-v diagram called the Rayleigh line can be obtained as

$$(P_b - P_u) = -(\rho_u D)^2 (v_b - v_u), \tag{1.5}$$

where, $v = 1/\rho$ is the specific volume. Using the mass flux, $\dot{m}'' = \rho_u D$, Equation 1.5 can be rewritten as

$$(P_b - P_u) = -(\dot{m}'')^2 (v_b - v_u). \tag{1.6}$$

In the Rayleigh line, $-(\dot{m}'')^2$ is the slope of the line.

From Equations 1.1, 1.2, and 1.3 with the relation, $c_p T = \frac{\gamma}{\gamma - 1} Pv$, the Hugoniot (Rankine-Hugoniot) curve can be derived in terms of P_b and v_b as

$$\frac{\gamma}{\gamma - 1}(P_b v_b - P_u v_u) - \frac{1}{2}(P_b - P_u)(v_b + v_u) = q, \tag{1.7}$$

where $\gamma = c_p/c_v$ is the adiabatic index, and c_v is the specific heat at constant volume. The detailed derivations of the Rayleigh line and the Hugoniot curve are available in Appendix A.

Figure 1.2 shows possible solution sets of Equations 1.1, 1.2, 1.3, and 1.4 using the Rayleigh line and the Hugoniot curve. Fixing the unburnt condition at v_u and P_u, the slope of the Rayleigh line can be chosen from $-\infty$ to 0, as $-(\dot{m}'')^2$ cannot be positive. Therefore, solutions in Areas (II) and (III) in Figure 1.2 are not possible. For a detonation, P_b is higher than P_u, so solutions of a detonation can be found in Area (I). Note that solutions in Area (IV) represent properties of a deflagration wave. In the detonation solutions, Area (I), there are three possible solution sets. Line A has two solutions: the upper point is the strong (overdriven) detonation, and the lower point is the weak detonation. Line B is tangential to the Hugoniot curve and has only one solution. The last case does not have solution as shown in Line C. It is known that the tangency solution is stable, so it is likely to be observed in the steady state detonation experiments. The strong detonation in Line A is not stable, so it can be only seen in transient states and eventually approach to the tangency solution. The weak detonation is not probable in the general detonation structures. Therefore, the detonation with the tangency solution is of interest, and specially called the Chapman-Jouguet (CJ) detonation. The tangential point is referred to as the CJ point, and the burnt mixture properties from a CJ detonation are called the CJ properties.

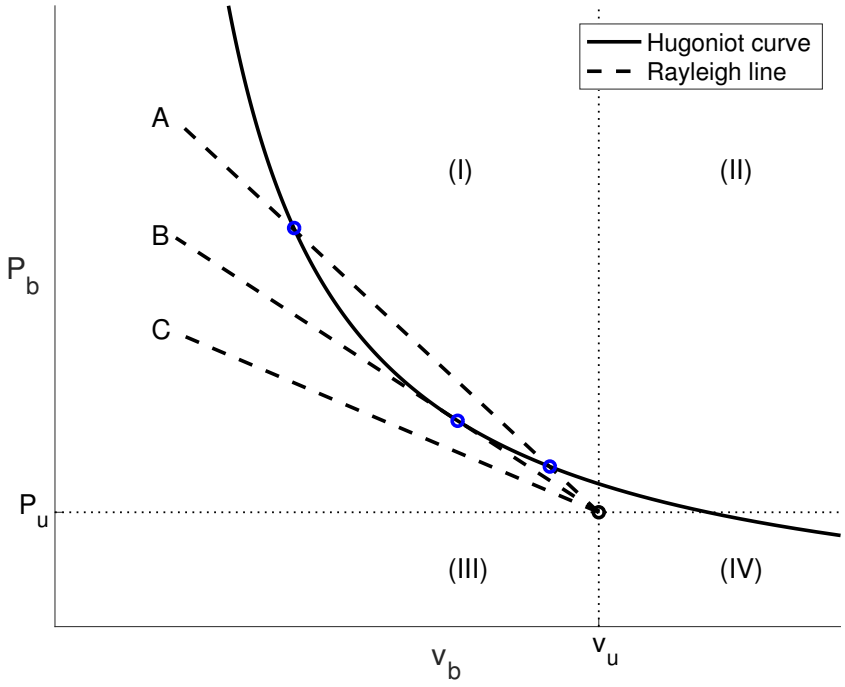

Figure 1.2: Possible solution sets of Rankine-Hugoniot conditions using Rayleigh line and Hugoniot curve.

Using the tangent condition of the Rayleigh line and the Hugoniot curve, the solution of the CJ detonation can be deduced. From the relation between slopes of the Rayleigh line and the Hugoniot curve,

$$\left(\frac{dP_b}{dv_b}\right)_{Rayleigh} = \left(\frac{dP_b}{dv_b}\right)_{Hugoniot}, \tag{1.8}$$

the CJ detonation condition can be found as

$$D_{CJ} - u_b = a_b, \tag{1.9}$$

where the subscript CJ denotes the CJ condition, and $a = (\gamma RT)^{1/2}$ is the sound speed. The CJ detonation velocity relative to the burnt fluid is sonic. Then, the mass conservation equation (Equation 1.1) yields

$$D_{CJ} = \frac{\rho_b}{\rho_u} a_b, \tag{1.10}$$

or

$$D_{CJ} = \frac{\rho_b}{\rho_u} \left(\gamma R T_b\right)^{1/2}, \tag{1.11}$$

from the CJ condition (Equation 1.9).

Using the CJ condition, the CJ properties can be deduced mathematically as

$$\frac{\rho_{CJ}}{\rho_u} = \frac{\rho_b}{\rho_u} = \frac{1}{\gamma}\left(1 - \frac{P_u}{P_b}\right) + 1, \tag{1.12}$$

$$\frac{T_{CJ}}{T_u} = \frac{T_b}{T_u} = \frac{\frac{q}{c_p T_u} + 1}{1 - \frac{\gamma-1}{2}\left[\left(\frac{\rho_b}{\rho_u}\right)^2 - 1\right]}, \tag{1.13}$$

$$\frac{P_{CJ}}{P_u} = \frac{P_b}{P_u} = \frac{\frac{2q\rho_u}{P_u} - \frac{\rho_u}{\rho_b} + \frac{\gamma+1}{\gamma-1}}{\frac{\gamma+1}{\gamma-1}\frac{\rho_u}{\rho_b} - 1}, \tag{1.14}$$

$$D_{CJ} = \frac{\rho_b}{\rho_u}\left\{\frac{q\left(\gamma-1\right) + a_u^2}{1 - \frac{\gamma-1}{2}\left[\left(\frac{\rho_b}{\rho_u}\right)^2 - 1\right]}\right\}^{1/2}. \tag{1.15}$$

As $P_b \gg P_u$ for a detonation wave, Equations 1.12 – 1.15 can be approximated:

$$\frac{\rho_{CJ}}{\rho_u} \cong \frac{1}{\gamma} + 1, \tag{1.16}$$

$$\frac{T_{CJ}}{T_u} \cong \frac{2\gamma^2}{\gamma+1}\left(\frac{q}{c_p T_u} + 1\right), \tag{1.17}$$

$$\frac{P_{CJ}}{P_u} \cong 2\gamma\left(\frac{q}{c_p T_u} + 1\right), \tag{1.18}$$

$$D_{CJ} \cong \left[2\left(\gamma^2-1\right)c_pT_u\left(\frac{q}{c_pT_u}+1\right)\right]^{1/2}. \tag{1.19}$$

Equations 1.17 – 1.19 can be further approximated when $\frac{q}{c_pT_u} \gg 1$ as

$$\frac{T_{CJ}}{T_u} \cong \frac{2\gamma^2}{\gamma+1}\left(\frac{q}{c_pT_u}\right), \tag{1.20}$$

$$\frac{P_{CJ}}{P_u} \cong 2\gamma\left(\frac{q}{c_pT_u}\right), \tag{1.21}$$

$$D_{CJ} \cong \left[2\left(\gamma^2-1\right)q\right]^{1/2}. \tag{1.22}$$

The CJ properties calculated using the above equations are generally very close to the those from experiments. The detailed derivations of the CJ detonation condition and properties (Equations 1.9 – 1.19) are also available in Appendix A.

The properties of a stoichiometric hydrogen/air mixture at standard temperature and pressure (STP), i.e., 25 °C and 1 atm, are: $\gamma \sim 1.3$, $c_p \sim 1.39$ kJ/kg/K, and $q \sim 2.89$ MJ/kg. The CJ properties of this mixture calculated using Equations 1.20 – 1.22 are: $T_{CJ} \sim 3055$ K, $P_{CJ} \sim 18.14$ atm, and $D_{CJ} \sim 1997$ m/s. Unlike premixed flame, the pressure rises more than ten times after the detonation wave passes. The detonation propagation speed is also much faster than laminar flame speed which is ∼2.2 m/s.

Detonation structure

Zel'dovich (1940a), von Neumann (1942), and Döring (1943) suggested a structure of one-dimensional detonation waves called the Zel'dovich-Neumann-Döring (ZND) structure. Figure 1.3 shows a typical ZND structure of detonation wave. In the figure, the detonation propagates to the right side. The left and right sides of the detonation are burnt and unburnt mixture, respectively. Note that the burnt side mixture is in the CJ state as explained in the previous section, so P, ρ, and T of burnt mixture approach to the CJ properties. The detonation wave has two parts, Areas (I) and (II), in the ZND structure. First, the unburnt mixture experiences Area (II) called induction zone. A shock wave is followed by the induction zone, so the mixture in the induction zone is adiabatically compressed by the shock. Therefore, pressure, density, and temperature increases sharply. As a certain amount of time is needed for the shocked mixture to ignite, the induction zone with constant properties is observed. The state of mixture in the induction zone is referred to as the von Neumann (VN) state. After the certain time in the induction zone, the mixture reacts actively in a short period as shown in Area (I). This area is called reaction zone, and the heat release rate per unit volume, $\dot{Q}$, is maximum in this area. In the reaction zone, temperature increases due to the reaction, but pressure and density decrease due to the expansion. After the reaction zone, the state of mixture approaches to the CJ state.

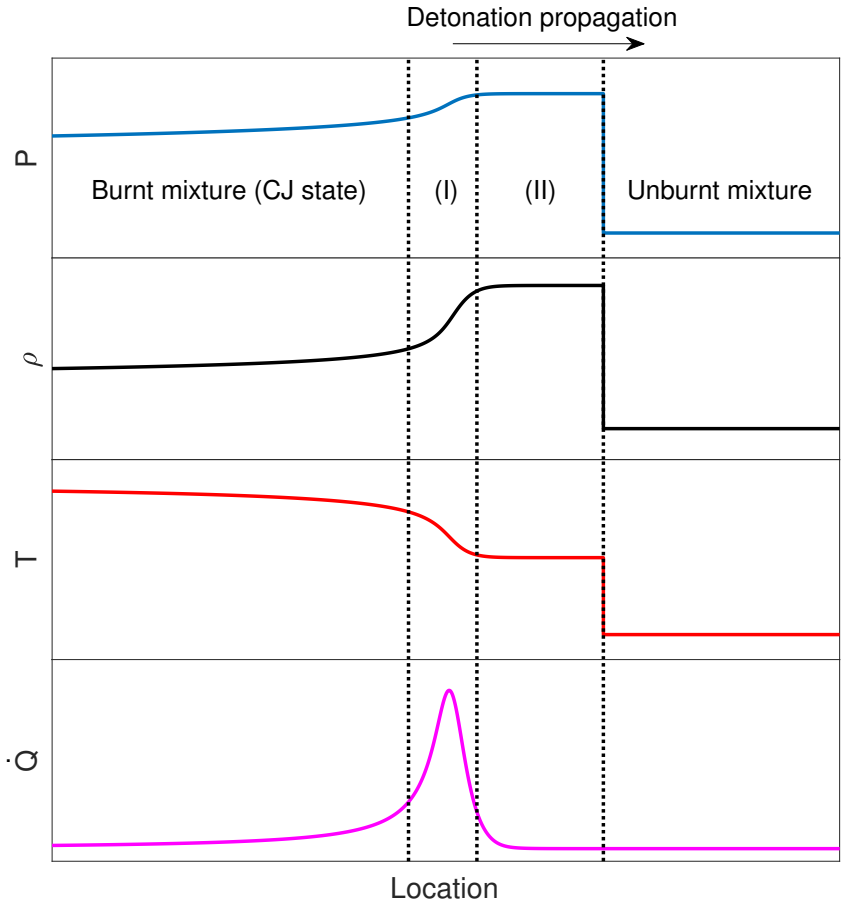

Figure 1.3: ZND structure of detonation wave. (I): Reaction zone, and (II): Induction zone (VN state).

Figure 1.4 presents the ZND structure on P-v diagram with the Rayleigh line and the Hugoniot curves. The dashed curve is the Hugoniot curve with $q = 0$, which implies that no reaction occurs along the dashed curve. Initially the mixture is at Point A (unburnt mixture). In the leading shock wave, the mixture is compressed along the dashed curve to Point B. Point B is the VN state, which is in the induction zone. In the reaction zone, the mixture follows the Rayleigh line to Point C. Thus, the Rayleigh line from Point B to Point C corresponds to the reaction zone in the ZND structure. Point C is the burnt mixture, and the mixture has the CJ properties. Therefore, properties at the VN and CJ states can be calculated graphically using the Rayleigh line and the Hugoniot curves.

The ZND structure can be also seen in the transient numerical simulations of detonation wave. Figure 1.5 shows simulation results from a transient numerical solver, which will be explained more in Chapter 2. In the figure, profiles of pressure, density, temperature, and heat release rate versus the location in a planar domain, x, are presented. A stoichiometric hydrogen/air detonation with $T_u = 1000$ K and $P_u = 5$ atm propagates to the right side

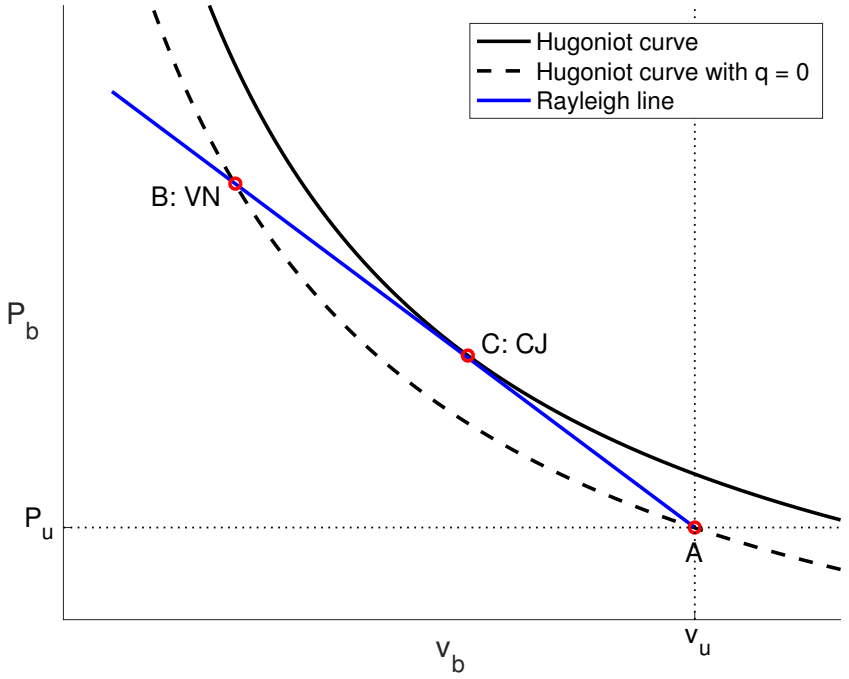

Figure 1.4: ZND structure on P-v diagram with the Rayleigh line and the Hugoniot curves A: Unburnt mixture, B: VN state, and C: CJ state.

of the domain. The overall structure corresponds to the ZND model including the reaction zone and induction zone.

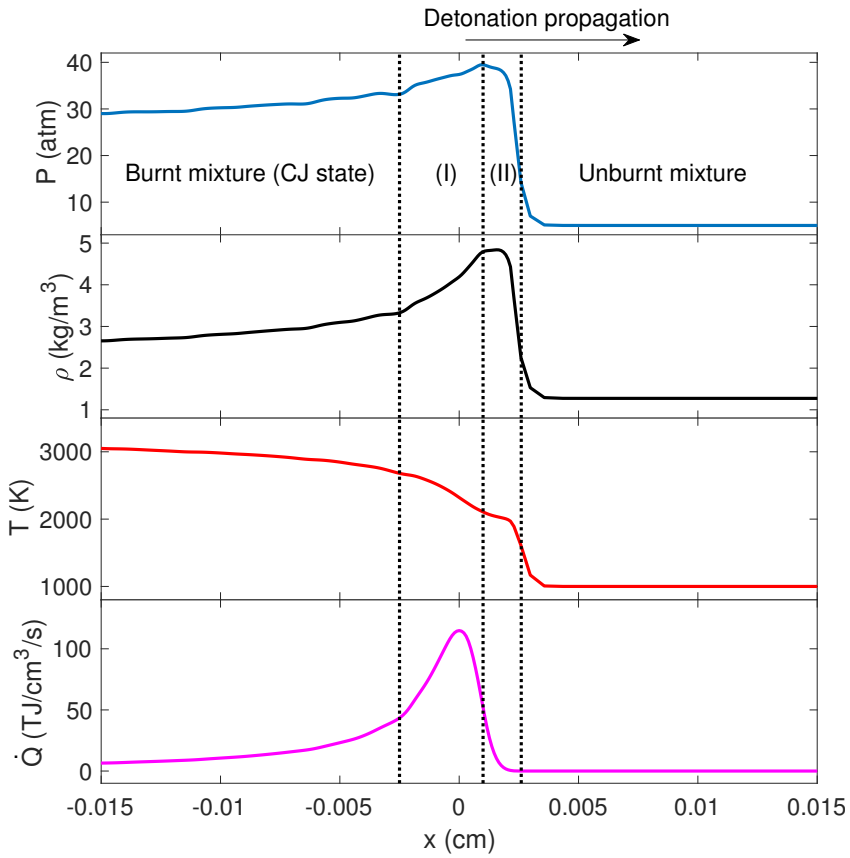

Figure 1.5: Transient simulation results of a stoichiometric hydrogen/air detonation wave with $T_u = 1000$ K and $P_u = 5$ atm.

Chapter 2

Methods

As the experiments of detonation are extremely difficult to be achieved, the work presented in this dissertation was mainly performed by several numerical solvers and aims to understand fundamental physics behind the phenomena. In this chapter, details regarding numerical solvers used in this presented work are given. The solvers include a calculation tool for steady state CJ-ZND detonation, and transient solvers with and without transport models.

2.1 Shock and Detonation Toolbox

The Shock and Detonation Toolbox (Browne et al., 2004; Kao and Shepherd, 2004) is a calculation toolbox for one-dimensional shock and detonation properties. The toolbox utilizes Cantera software (Goodwin et al., 2017) for the chemistry part. In this work, steady state detonation properties of given mixtures and conditions were calculated using the Shock and Detonation Toolbox for reference. The results of the solver include the CJ solution, the VN state properties, and values of the ZND structure such as induction length and reaction length. These values were referred to validate those from transient solvers.

The governing equations for the CJ detonation in the Shock and Detonation Toolbox are Equations 1.1 – 1.4. Thermodynamic properties are obtained from Cantera software with a given chemical kinetic model. Then, the toolbox solves the equations using the two-variable Newton-Raphson scheme with temperature and specific volume. The scheme was used by Reynolds (1986) to solve for a CJ detonation, and the same approach was implemented in the Shock and Detonation Toolbox.

For the ZND structure, the Shock and Detonation Toolbox solves the differential system of the one-dimensional reactive Euler equations as

$$w\frac{d\rho}{dx} + \rho\frac{dw}{dx} = 0, \tag{2.1}$$

$$\rho w\frac{dw}{dx} + \frac{dP}{dx} = 0, \tag{2.2}$$

$$w\left(\frac{dP}{dx}-\frac{d\rho}{dx}\right)=\rho a_f^2\dot{\sigma}, \tag{2.3}$$

$$w\frac{dY_i}{dx}=\dot{\Omega}_i, \tag{2.4}$$

where w is the normal velocity in the shock-fixed frame, a_f is the frozen sound speed, $\dot{\sigma}$ is the thermicity which measures the rate of chemical energy transformation into thermal energy, Y_i is the mass fraction of species i, $\dot{\Omega}_i$ is the mass fraction production rate of species i. An array of the thermicity are created by the Cantera software, and the differential system (Equations 2.1 – 2.4) is solved using a stiff ordinary differential equation (ODE) solver, MATLAB *ode15s* function (MathWorks, 2018).

More details of the Shock and Detonation Toolbox including background, derivations, algorithms, validations, and examples can be found in Browne et al. (2004) for the CJ solution, and Kao and Shepherd (2004) for the ZND structure calculation.

2.2 Solver for Lagrangian Equations of Deflagration/Detonation (SLED)

This section is based on the final class project report of *ASTRO 255 Computational Methods in Theoretical Astrophysics* in Spring 2016 semester by Professor Richard Klein at the University of California, Berkeley. The author acknowledges Professor Klein for discussions on numerical methods.

Simulations of detonation initiation or deflagration to detonation transition (DDT) problem with detailed chemical kinetics are computationally expensive and slow, because capturing shock front and stiff chemical reaction needs very small time step and grid size. Typically, the time step and grid size should be smaller than 1 ns and 10 μm respectively, to achieve solutions with high fidelity. Therefore, a simpler solver for trial simulations called the Solver for Lagrangian Equations of Deflagration/Detonation (SLED) was developed to investigate the phenomena roughly in advance of running expensive sophisticated simulations.

In this section, governing equations, numerical schemes, and the solving procedure for SLED are presented. Then, some examples and code validation are reported.

Lagrangian finite-difference equations

SLED solves the Lagrangian finite-difference equations for reactive compressible flow in one-dimensional spherical domain. The governing equations of a one-dimensional fluid motion using the time-independent Lagrangian invariant (von Neumann and Richtmyer, 1950) are

$$u=\frac{\partial x}{\partial t}, \tag{2.5}$$

$$\frac{1}{\rho} = \frac{\partial x}{\partial M}, \tag{2.6}$$

$$\frac{\partial u}{\partial t} = -\frac{\partial P}{\partial M}, \tag{2.7}$$

$$\frac{\partial e}{\partial t} + P\frac{\partial (1/\rho)}{\partial t} = 0, \tag{2.8}$$

$$P = e\rho\left(\gamma - 1\right), \tag{2.9}$$

where t is the time, M is the Lagrangian invariant mass, and e is the internal energy per unit mass.

These equations were modified to solve spherical reactive wave propagation problem, and the finite-difference forms are

$$\frac{r_l^{n+1} - r_l^n}{\Delta t^{n+\frac{1}{2}}} = u_l^{n+\frac{1}{2}}, \tag{2.10}$$

$$\Delta M_l = \rho_{l+\frac{1}{2}}^{n+1} \frac{4\pi}{3}\left(r_{l+1}^{n+1\,3} - r_l^{n+1\,3}\right), \tag{2.11}$$

$$\frac{u_l^{n+\frac{1}{2}} - u_l^{n-\frac{1}{2}}}{\Delta t^{n+\frac{1}{2}}} = 4\pi r_l^2 \left(\frac{P_{l+\frac{1}{2}}^n + A_{l+\frac{1}{2}}^{n-\frac{1}{2}} - P_{l-\frac{1}{2}}^n - A_{l-\frac{1}{2}}^{n-\frac{1}{2}}}{\Delta M_l}\right), \tag{2.12}$$

$$e_{l+\frac{1}{2}}^{n+1} - e_{l+\frac{1}{2}}^n + \left(\frac{P_{l+\frac{1}{2}}^{n+1} + P_{l+\frac{1}{2}}^n}{2} + A_{l+\frac{1}{2}}^{n+\frac{1}{2}}\right)\left(\frac{1}{\rho_{l+\frac{1}{2}}^{n+1}} - \frac{1}{\rho_{l+\frac{1}{2}}^n}\right) = q_{l+\frac{1}{2}}^{n+\frac{1}{2}}, \tag{2.13}$$

$$P_{l+\frac{1}{2}}^{n+1} = e_{l+\frac{1}{2}}^{n+1} \rho_{l+\frac{1}{2}}^{n+1}\left(\gamma_{l+\frac{1}{2}}^{n+1} - 1\right), \tag{2.14}$$

where r is the location in the spherical domain, Δt is the size of time step, A is the artificial viscosity term, ΔM is the Lagrangian invariant mass of a fluid element, the subscript l denotes the mesh point, and the superscript n denotes time step. Note that staggered mesh points are represented using $\frac{1}{2}$ in subscript and superscript.

The initial values of the Lagrangian invariant mass of each fluid element are time-independent, so the size of each mesh changes every time step to keep the value of the Lagrangian invariant mass constant. The high pressure zone has finer meshes, while meshes in the low pressure zone are coarse. This approach is beneficial in the compressible wave propagation problem, since the high pressure zone, i.e., shock area, is of interest. By the Lagrangian finite-difference approach, the problem can be solved with a smaller number of meshes.

Equations 2.12 and 2.13 include the artificial viscosity term (von Neumann and Richtmyer, 1950). The term is added to the pressure terms of the equations for the artificial

dissipation to resolve the stiff shock front. It smooths out the pressure cliff to solve equations numerically. In SLED, A is a function of u, ρ, and a, including linear and quadratic terms as suggested in *ASTRO 255* lecture:

$$A_{l+\frac{1}{2}}^{n+\frac{1}{2}} = \frac{c_0^2\left(u_{l+1}^{n+\frac{1}{2}} - u_l^{n+\frac{1}{2}}\right)^2}{\frac{1}{2}\left(\frac{1}{\rho_{l+\frac{1}{2}}^{n+1}} + \frac{1}{\rho_{l+\frac{1}{2}}^{n}}\right)} - \frac{c_1\left(u_{l+1}^{n+\frac{1}{2}} - u_l^{n+\frac{1}{2}}\right)}{\frac{1}{2}\left(\frac{1}{\rho_{l+\frac{1}{2}}^{n+1}} + \frac{1}{\rho_{l+\frac{1}{2}}^{n}}\right)} a_{l+\frac{1}{2}}^{n+1}, \tag{2.15}$$

where c_0 and c_1 are constants. The artificial viscosity term is only applied for the meshes that $\frac{\partial u}{\partial r} < 0$. In Equation 2.15, the sound speed, a, can be calculated using the value of A in the previous time step as

$$a_{l+\frac{1}{2}}^{n+1} = \gamma_{l+\frac{1}{2}}^{n+1}\sqrt{\frac{P_{l+\frac{1}{2}}^{n+1} + A_{l+\frac{1}{2}}^{n-\frac{1}{2}}}{\rho_{l+\frac{1}{2}}^{n+1}}}. \tag{2.16}$$

For examples and code validation, $c_0^2 = 1$ and $c_1 = 0.5$ were used.

CHEMKIN package

SLED utilizes the CHEMKIN (Kee et al., 1996) subroutine libraries to load thermodynamic data and calculate chemical properties from the chemical kinetic models. CHEMKIN is one of the mainly used packages in combustion research. It was developed by Sandia National Laboratories in 1996 using FORTRAN 77 to solve large systems of chemical reactions.

CHEMKIN interpreter produces CHEMKIN link binary file (*chem.bin*) from the reactions (*chem.inp*) and thermodynamic data (*therm.dat*). Then, the Gas-Phase Subroutine Library loads the binary file and calculates chemical properties. More details of CHEMKIN including equations, structure, and examples are available in Kee et al. (1996).

Algorithm

The finite-difference equations (Equations 2.10 – 2.14) were implemented in FORTRAN, and the details of the solving procedure are as follows:

1. Initial conditions such as domain size, grid size, and profiles of temperature, pressure, and species mass fractions in the domain are defined. Boundary conditions are also set.

2. Thermodynamic data is loaded from CHEMKIN database file for the specified initial conditions.

3. Density profile is calculated using CHEMKIN subroutine.

4. Initially, the Lagrangian invariant masses for each element are computed from density and initial mesh location by Equation 2.11.
5. Initial time step size is guessed by the Courant–Friedrichs–Lewy (CFL) stability.
6. Equation 2.12 is solved to calculate velocity for the next time step.
7. Mesh locations for the next time step are calculated using Equation 2.10.
8. Mean molecular weights and chemical molar production rates of the species are calculated from CHEMKIN subroutine.
9. Mass fractions of species for the next time step are computed using the values from Step 8.
10. Iteration is performed from Step 6 to Step 9 using smaller time step sizes until the stable and physical solutions for mesh locations and mass fractions of species are obtained.
11. Density profile for the next time step is calculated by Equation 2.11.
12. The ratios of specific heats are computed using CHEMKIN subroutines.
13. Internal energies for current time step are calculated from Equation 2.14.
14. Sound speeds are computed using Equation 2.16.
15. Artificial viscosity terms are calculated by Equation 2.15.
16. Enthalpies of each species are obtained from CHEMKIN subroutines.
17. Heat releases during the time step are calculated using enthalpies and molar production rates of the species.
18. Energy equation is solved explicitly using Equations 2.13 and 2.14.
19. Temperature profile for the new time step is calculated using CHEMKIN subroutines and the equation of state.
20. All values are updated, and a calculation for the next time step is started from Step 5.

It was performed successfully and produced reasonable results with much shorter calculation time than the sophisticated research code. The stability control with the initial time step size was a big issue during the code development. However, the issue was solved by the iteration procedure (Step 6 to Step 9) to find a stable time step size.

Examples

Several examples were calculated using SLED. A reaction propagation wave was initiated from temperature gradient of the center hot spot, i.e., a zone at higher temperature than the surrounding. The mixtures at different temperature have different auto-ignition delay times, and the auto-ignition delay time is exponentially decreased as temperature increases. Thus, the initial temperature gradient can produce reaction front propagation from the center to the outside of the hot spot. The hot spot works as an ignition source.

In these examples, the radius for the one-dimensional spherical domain is 10 cm. An isotropic flow is assumed and the reflective boundary condition at the center was applied. The code can solve for both open and closed boundary conditions at the outer boundary, and the open boundary condition was used here. Outside of the hot spot, temperature is uniformly 1180 K, and pressure is 50 atm everywhere. Initially, the size of every mesh is 0.2 mm. The initial mixture is a stoichiometric 50%H_2-50%CO/air mixture, so the initial mole fractions are $X_{CO} = 0.148$, $X_{H_2} = 0.148$, $X_{O_2} = 0.148$, $X_{N_2} = 0.556$. The size of time step is initially 2.6 ns, and it adaptively reduces to the order of 0.01 ns for the stability when the ignition happens. Several cases with different maximum hot spot temperatures were solved to capture different modes of reaction front propagation. The temperature is maximum at the center of hot spot and linearly decreases to the outer temperature. The size of hot spot is 5 mm for all cases. For chemistry, 13 species skeletal mechanism for 50%H_2-50%CO/air mixture from GRI-Mech 3.0 (Smith et al., 1999) was used.

Figure 2.1 shows the calculation result from the hot spot with center temperature of 1183 K. The temperature difference between the center and the outside of hot spot, ΔT, was 3 K. Due to the relatively low temperature gradient, the autoignition delay times at neighboring meshes in the hot spot were similar. Thus, the reaction front propagation speed was very fast, and the reaction wave was ahead of the pressure wave. The center of hot spot started to ignite at $\sim$65 μs, and the reaction front propagated very fast until $\sim$67 μs. At about 67 μs, autoignition occurred simultaneously in the unburnt mixture, and the reaction front propagation became a thermal explosion without detonation initiation.

ΔT was increased to 20 K (maximum temperature of 1200 K) for the second example as shown in Figure 2.2. A detonation propagation was obtained. The reaction front propagation speed and sound speed were on the same order of magnitude, and the resonance of two waves produced the detonation wave. High pressure peaks and temperature cliffs were observed compared to the previous example. As the hot spot temperature was higher than that of the deflagration and thermal explosion case, the hot spot ignited earlier. Thus, the reaction front propagated longer before the simultaneous autoignition.

Validation

The code was validated using the example result shown in Figure 2.2. A simulation was performed using a more sophisticated research code (Chen, 2009; Chen et al., 2009) with the

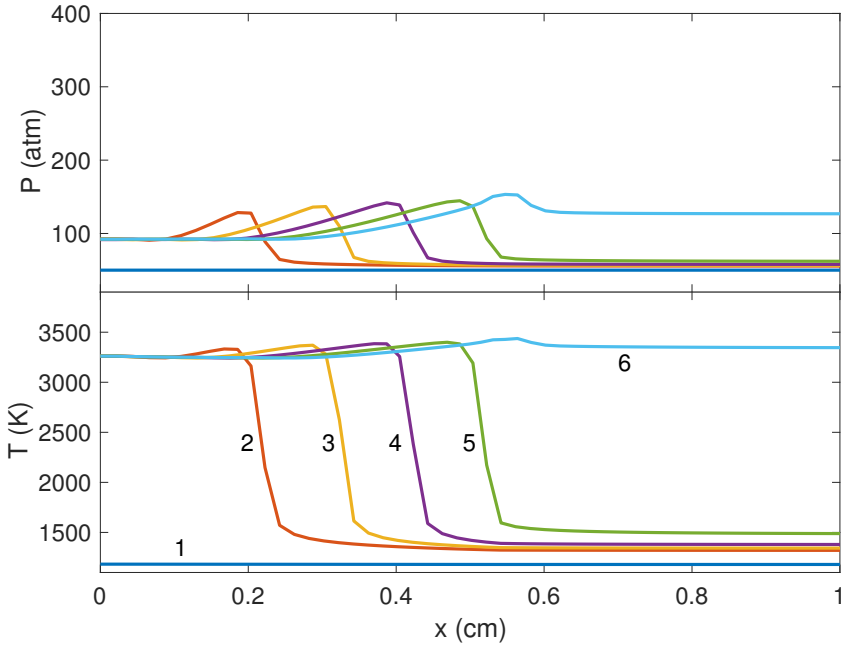

Figure 2.1: Deflagration and thermal explosion from SLED calculation with $\Delta T = 3$ K. Time sequences 1: 0.00 μs, 2: 65.52 μs, 3: 65.99 μs, 4: 66.43 μs, 5: 66.84 μs, 6: 67.23 μs.

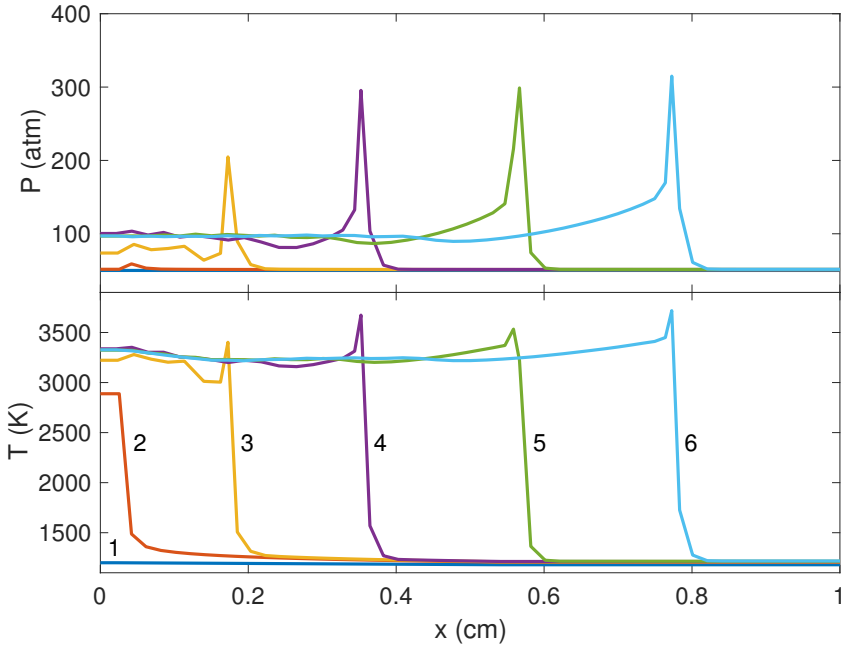

Figure 2.2: Detonation initiation from SLED calculation with $\Delta T = 20$ K. Time sequences 1: 0.00 μs, 2: 50.51 μs, 3: 52.21 μs, 4: 53.37 μs, 5: 54.56 μs, 6: 55.71 μs.

same conditions. The sophisticated code is an in-house code for reactive compressible flows using finite-volume method with transport models, which requires expensive computational cost. The details about the code are presented in the following section. The result from the research code is presented in Figure 2.3. The magnitude of pressure peaks and detonation wave speed were very close to the result from SLED. Even though the result in Figure 2.3 oscillates less and describes the leading shock front more accurately, the solution from SLED is still reasonable and captures the similar trend in a very short computation time. Therefore, SLED can be used as a good trial solver to estimate a primary trend or result before running the sophisticated research code.

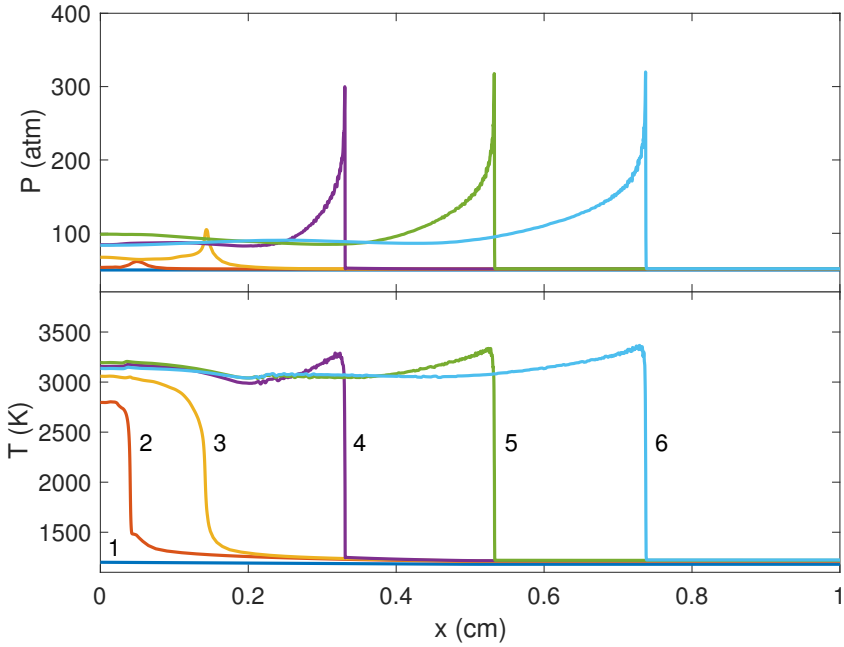

Figure 2.3: Detonation initiation from sophisticated research code calculation with $\Delta T = 20$ K. Time sequences 1: 0.00 μs, 2: 52.34 μs, 3: 53.90 μs, 4: 55.07 μs, 5: 56.25 μs, 6: 57.42 μs.

2.3 Adaptive Simulation of Unsteady Reactive Flow (A-SURF)

The transient simulation work presented in this dissertation was mainly performed by Adaptive Simulation of Unsteady Reactive Flow (A-SURF). A-SURF (Chen, 2009) is a research code written in FORTRAN to simulate compressible reactive flows. The one-dimensional multi-species unsteady conservation equations are solved with the adaptive mesh refinement (AMR) method. A parallel version of the code, ASURF-Parallel (Shi, 2017), was developed using Message Passing Interface (MPI) for the efficient use of computational resources. Both

original and parallel versions of the code have been validated by multiple researchers for studies on compressible reactive flows (Chen et al., 2009; Dai and Chen, 2015; Pan et al., 2016; Qi and Chen, 2017; Shi et al., 2017b). In this work, ASURF-Parallel was used to perform transient simulations of detonation initiation, propagation, and suppression in inhomogeneous mixtures.

In this section, governing equations, transport and chemistry models, and numerical methods of A-SURF are presented. A-SURF has an ability to simulate one-dimensional flows in planar, cylindrical, or spherical coordinate. However, in the following sections, all governing equations and model equations are presented only in the one-dimensional planar coordinate for the simplicity. The governing equations in cylindrical and spherical coordinates and more details on A-SURF can be found in Chen (2009). The parallelization process of ASURF-Parallel is briefly explained in the later section, and details are available in Shi (2017).

Governing equations

The governing equations in a planar coordinate can be written as

$$\frac{\partial}{\partial t}\begin{pmatrix}\rho Y_1\\ \rho Y_2\\ \vdots\\ \rho Y_N\\ \rho u\\ E_t\end{pmatrix}+\frac{\partial}{\partial x}\begin{pmatrix}\rho u Y_1\\ \rho u Y_2\\ \vdots\\ \rho u Y_N\\ \rho u^2+P\\ (E_t+P)\,u\end{pmatrix}=\frac{\partial}{\partial x}\begin{pmatrix}-\rho u_1^* Y_1\\ -\rho u_2^* Y_2\\ \vdots\\ -\rho u_N^* Y_N\\ \tau\\ \dot{q}''+\Phi\end{pmatrix}+\begin{pmatrix}\dot{m}_1'''\\ \dot{m}_2'''\\ \vdots\\ \dot{m}_N'''\\ 0\\ 0\end{pmatrix}. \tag{2.17}$$

The left hand side of Equation 2.17 has unsteady and convection terms. In the right hand side of equation, there are diffusion and chemical source terms. From the first row to the N^{th} row of Equation 2.17 are species conservation equations. The $(N+1)^{th}$ row is the Navier–Stokes (momentum) equation, and the last row is the energy conservation equation. Thus, $(N+2)$ equations are solved during the A-SURF simulations. In the speceis conservation part of Equation 2.17, u_i^* and $\dot{m}_i'''$ are the diffusion velocity and mass production rate per unit volume of species i respectively, and N is the total number of species. In the momentum and energy equations, τ is the viscous stress, E_t is the total energy per unit volume, $\dot{q}''$ is the heat flux, and Φ is the viscous dissipation term. Note that the total energy is defined as

$$E_t = -P + \frac{\rho u^2}{2} + \rho \sum_{i=1}^{N} (Y_i h_i), \tag{2.18}$$

where h_i is the enthalpy of species i.

Transport and chemistry models

All transport properties are obtained or calculated using the TRANSPORT package (Kee et al., 1986) during the A-SURF simulations. The TRANSPORT package requires input files with basic transport and thermodynamic properties.

The diffusion velocity of each species, u_i^*, in the species conservation equations can be obtained by solving a system of diffusion equations. In A-SURF, the mixture-averaged formula including correction velocity to ensure mass conservation in TRANSPORT package (Kee et al., 1986) is used for species diffusion to reduce the computational cost.

The gas mixture is assumed as a Newtonian fluid, so the viscous stress in the momentum conservation equation is modeled by the Stokes' law of friction. For a planar coordinate, viscous stress is modeled as

$$\tau = \frac{4}{3}\mu\frac{\partial u}{\partial x}, \tag{2.19}$$

where μ is the dynamic viscosity of the mixture.

In the energy conservation equation in planar coordinate, the heat flux contains two terms as

$$\dot{q}'' = \lambda\frac{\partial T}{\partial x} - \rho\sum_{i=1}^{N}(u_i^* Y_i h_i), \tag{2.20}$$

where the λ is the thermal conductivity. In Equation 2.20, the first term is the heat conduction expressed by the Fourier's law and the second term is the heat flux by diffusion of species with different enthalpies. Moreover, the viscous dissipation term is modeled as

$$\Phi = u\frac{\partial \tau}{\partial x} + \frac{4}{3}\mu\left(\frac{\partial u}{\partial x}\right)^2. \tag{2.21}$$

The chemical system is solved to obtain the mass production rate of each species, $\dot{m}_i'''$, by the CHEMKIN package (Kee et al., 1996). A chemical mechanism input file containing elementary reactions and reaction parameters is required to evaluate the production rate by the law of mass action and the empirical Arrhenius law.

Numerical methods

The governing equations are solved by the fractional-step procedure due to the stiff chemical source term. In the first fractional step, the chemical source term is removed, so the partial differential equations (PDEs) with unsteady, convection, and diffusion terms are solved. Then, the ordinary differential equations (ODEs) with only unsteady and chemical source terms are solved in the second fractional step. Therefore, the non-reactive flow system and the homogeneous reacting system are solved separately. Multiple options of numerical schemes are available in A-SURF to solve PDEs and ODEs. In this section, only schemes used in the present study are introduced.

The non-reactive PDE system is discretized by finite volume method to resolve the discontinuous shock front. Instead of evaluating derivative values as in finite difference method, the integral values over a control volume of interest are evaluated. Specifically, the HLLC (Toro et al., 1994) and a second order central difference schemes are employed to evaluate convective and diffusive fluxes, respectively. For the time integration of PDE system, the first-order Euler method is used in the study. For the reacting ODE system, the implicit VODE solver (Brown et al., 1989) is utilized to resolve stiff chemical source term.

Using a fine mesh size over the whole domain is computationally expensive. In A-SURF, the mesh adaptation is applied for the efficient use of computational resources, so the meshes in the area of interest are locally subdivided, and meshes in the area of less important are merged dynamically.

Parallelization

ASURF-Parallel is a parallel version of A-SURF using MPI, and reduces the computation time. The domain is decomposed between the processors based on the number of grid cells. For synchronization, one node is dedicated to write files. Each processor updates its sub-domain with additional boundary cells, as the solution of a grid cell depends on its neighboring cells. Then, the equations are solved in each sub-domain independently and simultaneously. After the calculations, MPI_GATHER and MPI_BCAST routines are used to collect data set and update data to every processor for the new time step.

Chapter 3

Detonation Initiation

Detonation initiation by deflagration to detonation transition (DDT) is a process that has been studied actively due to its relevance to engine super-knock issues. Recently, the internal combustion researchers have been developing downsized engines with high boosted direct injection to improve power density, fuel economy, and emission. However, a super-knock, which has much higher pressure peak than that of the conventional knock, was frequently observed during the operation of the downsized engines, and the engine was damaged easily (Wang et al., 2015a). Multiple studies (Wang et al., 2015a,b; Qi et al., 2015a,b) found that the super-knock occurs due to DDT in the engine cylinder. Therefore, understanding the mechanism of DDT is essential to prevent super-knock phenomena.

In this chapter, studies on detonation initiation are presented. First, the reaction front propagation modes from hot spots are discussed using the reactivity gradient theory. Then, to predict DDT occurrences, the transient and integral reactivity gradient methods are proposed and evaluated. Lastly, prediction of DDT occurrence using several machine learning techniques are introduced and examined.

3.1 Reactivity gradient theory

Zel'dovich proposed a theory relating reaction front propagation modes to spatial auto-ignition sequence, i.e., the reactivity gradient (Zel'dovich et al., 1970; Zel'dovich, 1980). In this theory, the speed of reaction front propagation relative to unburnt mixture is defined using the reactivity gradient as

$$u_r = \left(\frac{\partial \tau_i}{\partial r} \right)^{-1}, \tag{3.1}$$

where τ_i is the ignition delay time. Different reaction front propagation modes were identified by comparing the inverse of reactivity gradient to the corresponding sound speed and laminar flame speed.

Gu et al. (2003) applied this theory to the hot spot induced DDT in a stoichiometric 50%H_2-50%CO/air mixture. The reactivity gradient was normalized by the critical value of reactivity gradient, which was the inverse of sound speed:

$$\xi = \frac{\left(\frac{\partial \tau_i}{\partial r}\right)}{\left(\frac{\partial \tau_i}{\partial r}\right)_c} = \frac{\left(\frac{\partial \tau_i}{\partial r}\right)}{\left(\frac{1}{a}\right)} = \frac{a}{u_r}, \tag{3.2}$$

where subscript c denotes the critical value. As in Equation 3.2, the normalized reactivity gradient, ξ, is simply the ratio of a to u_r. ξ can be rewritten in terms of temperature gradient of the hot spot as

$$\xi = \frac{\left(\frac{\partial \tau_i}{\partial T}\frac{\partial T}{\partial r}\right)}{\left(\frac{1}{a}\right)} = \frac{\partial \tau_i}{\partial T}\frac{\partial T}{\partial r}a. \tag{3.3}$$

The values of normalized reactivity gradient can be obtained from the sound speed, ignition delay time, and temperature gradient in the hot spot. They identified five reaction front propagation modes of Zel'dovich's classification (Zel'dovich, 1980) numerically by changing temperature gradient of hot spot, and these are:

1. $\xi = 0$, near-instantaneous thermal explosion,
2. $0 < \xi < \xi_l$, supersonic autoignitive deflagration,
3. $\xi_l \leq \xi < \xi_u$, developing and developed detonation,
4. $\xi_u \leq \xi < \frac{a}{S_L}$, subsonic autoignitive deflagration,
5. $\xi \geq \frac{a}{S_L}$, laminar burning deflagration ,

where subscript ξ_l and ξ_u denote the lower and upper limiting values of ξ for a developing detonation respectively, and S_L is the laminar flame speed. The occurrence of these different modes is strongly correlated to the reactive gradient of initial hot spot, ξ. If ξ is large enough, acoustic wave is faster than than reaction front propagation wave, so the propagation is a subsonic deflagration. When ξ is small, reaction front propagation wave is ahead of acoustic wave, so the propagation is a supersonic deflagration, or a thermal explosion for $\xi = 0$. If ξ approaches to unity, i.e., autoignition front propagation speed approximately approaches to acoustic wave speed, those two waves resonate and a detonation wave is likely to initiate.

Further studies using the value of temperature gradient have been done actively. Dai et al. (2015) employed the same methodology as in Gu et al. (2003) for n-heptane/air mixture, which has negative temperature coefficient region. The possibility of DDT induced by a cold spot instead of a hot spot was explained. Dai and Chen (2015) studied three ignition stages of n-heptane/air mixture during a hot spot induced supersonic reaction front propagation.

3.2 Transient reactivity gradient

In the previous section, the reactivity gradient is employed as an indicator to estimate whether a detonation is initiated in a hot spot. A detonation develops when $\xi \sim 1$, or $\xi_l \leq \xi < \xi_u$. However, in the simulation results of Gu et al. (2003), a detonation was not initiated even though $\xi = 1$. It was also found that although the initial ξ was higher than order of unity ($\xi > \xi_u$), there was a developing detonation. The reason is that the value of ξ changes during the induction time due to conduction, diffusion and chemical reaction.

Therefore, in this study, transient values of ξ in the unburnt mixture near ignition front are proposed instead of ξ based on the initial temperature gradient to analyze detonation initiation phenomena better. Moreover, the spatial distribution of ξ is employed rather than using one value of ξ. Equation 3.2 can be rewritten to calculate temporal evolution of ξ distribution:

$$\xi(r,t) = \frac{\partial \tau_i(r,t)}{\partial r} a(r,t), \tag{3.4}$$

where ξ, τ_i, and a are functions of location and time.

Temporal and spatial values of $(\partial \tau_i / \partial r)$ can be obtained from the local slope of the autoignition delay time versus temperature plot and the temperature profiles from numerical calculations. Transient values of local sound speed, $a = (\gamma RT)^{1/2}$, also can be deduced directly from the temperatures profile. For example, Figure 3.1 shows values of τ_i versus temperature calculated from SENKIN (Lutz et al., 1988) for a stoichiometric 50%H_2-50%CO/air mixture at 50 atm. The result shows that autoignition delay time exponentially decreases as temperature increases in general. The values of a for the same mixture versus temperature are also shown in Figure 3.2. Since the sound speed does not vary much compared to the autoignition delay time with temperature, ξ depends more on the gradient of ignition delay time than the sound speed.

Simulation setup

A transient simulation of ignition and reaction front propagation was carried out using ASURF-Parallel (Chen, 2009; Shi, 2017), a time-accurate and space-adaptive solver for one-dimensional compressible multi-component reactive flows. In the simulation, a one-dimensional spherical domain with radius of 10 cm was used. Both the center and the outer boundaries had reflective boundary conditions.

Initially, a hot spot of radius 3 mm was specified at the center, and the hot spot initiated an autoignition event generating a reaction front propagation outwardly. The initial temperature was 1077 K at the center and linearly decreased to 1066 K at $r = 3$ mm. The temperature was uniform at 1066 K throughout the rest of the domain. The initial pressure was 50 atm. The minimum grid size was set to $\sim$0.2 μm and the CFL number was 0.2. The domain contained a stoichiometric 50%H_2-50%CO/air mixture. A 12-species skeletal

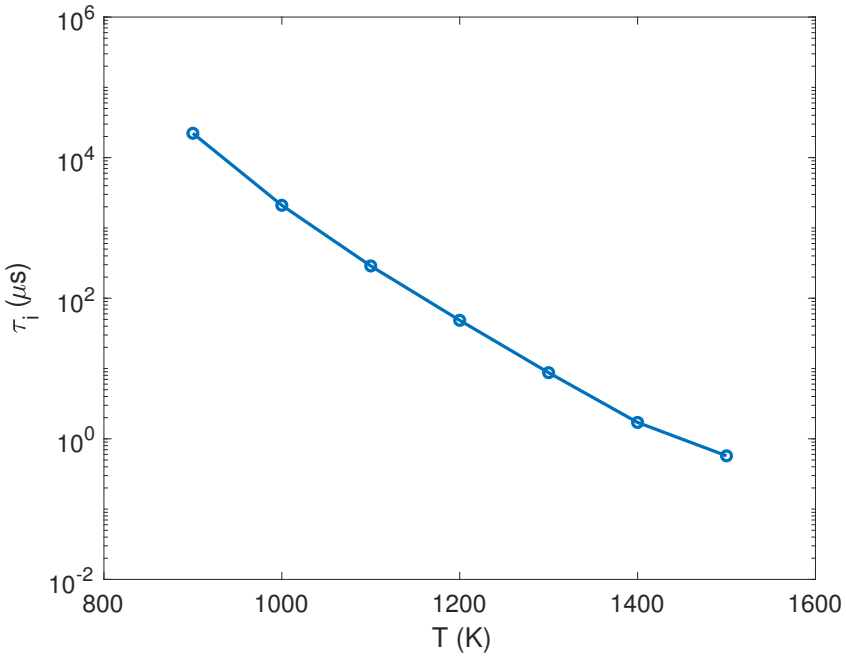

Figure 3.1: Computed autoignition delay times versus temperature for stoichiometric 50%H_2-50%CO/air mixture at 50 atm.

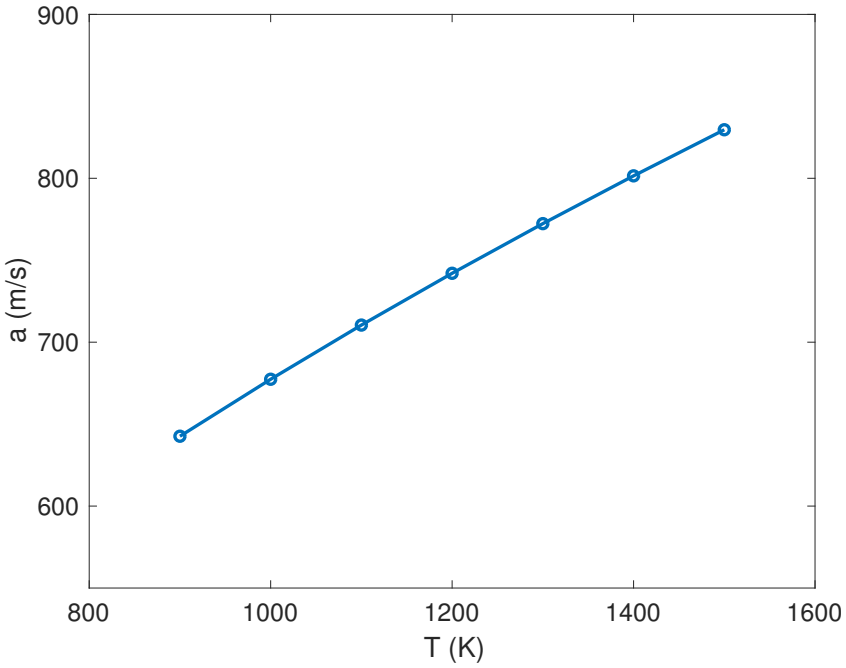

Figure 3.2: Computed sound speeds versus temperature for stoichiometric 50%H_2-50%CO/air mixture at 50 atm.

chemical kinetic mechanism for the H_2/CO combustion was developed from GRI-Mech 3.0 (Smith et al., 1999) and used in the current study.

Results and discussion

The normalized reactivity gradient of the initial hot spot in this simulation setup was 25. As this value was larger than the order of unity, subsonic deflagration was estimated from the initial reactivity gradient. Figure 3.3 shows that development of pressure, temperature and ξ during a hot-spot induced reaction propagation. Based on the temperature profiles of each time sequence, $(\partial\tau_i/\partial r)$ and a were calculated, and ξ distributions were obtained using Equation 3.4.

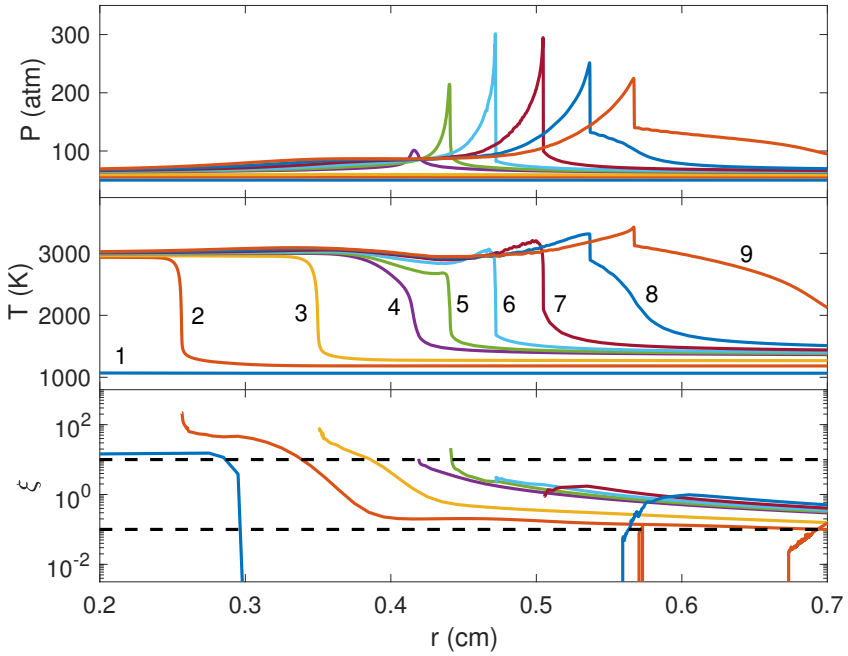

Figure 3.3: Development of pressure, temperature, and ξ for a hot spot with $\xi = 25$. Time sequence 1: 0.0 μs, 2: 527.3 μs, 3: 543.4 μs, 4: 545.9 μs, 5: 546.2 μs, 6: 546.5 μs, 7: 546.8 μs, 8: 547.0 μs, 9: 547.3 μs. Dashed lines correspond to $\xi = 10$ and 0.1 respectively.

The initial distribution of normalized reactivity gradient was approximately 25 in the hot spot area (from 0 to 0.3 cm). In the outside of the hot spot, ξ was close to 0, as the mixture was homogeneous. Note that ξ distributions in Figure 3.3 are presented in the log-scale, so points with $\xi = 0$ are not shown in the figure. The subsonic deflagration was initiated and propagated until ~0.4 cm. At time sequence 4, ξ ahead of the reaction front reduced to the order of unity leading to a developing detonation until time sequence 7. The area ahead of detonation front at time sequences 8 and 9 had very small values of ξ, so the reaction

front propagation became a supersonic deflagration followed by a near-instantaneous thermal explosion.

The initial reactivity gradient only can estimate the approximate mode of reaction propagation. However, using the transient ξ distribution, the effect of conduction, diffusion and chemical reaction during the induction time on the reactivity gradient can be observed, and the transient reaction propagation modes can be captured with a clear explanation. The process of transition to each mode can be understood by temporal evolution of ξ distribution in the reaction front region, and it showed that the reaction propagation was involved with DDT followed by a thermal explosion. Even though initial ξ is larger than the order of unity, the initial deflagration can transition to a detonation wave. Therefore, to predict a detonation occurrences more precisely, a method including both direct detonation initiation and DDT is proposed in the next section.

3.3 Integral reactivity gradient

The normalized reactivity gradient calculated from the initial temperature profile is an indicator to estimate the mode of the reaction propagation from an inhomogeneous mixture. However, due to the conduction, diffusion and chemical reaction during the induction time, it cannot successfully predict the occurrence of a detonation for the cases with relatively long initiation time. Moreover, as discussed in the previous section, the transition process is not considered, so the detonation initiation by DDT is not fully estimated and the detonation initiation time cannot be predicted. In this study, an integral reactivity gradient method is proposed to predict the occurrence of detonation more accurately.

Temperature profile after the induction time

Since the reactivity gradient changes during the induction time due to the conduction, diffusion and chemical reaction, if ξ is obtained after the induction time, it can predict the detonation occurrences more precisely. Therefore, the estimation of temperature profile after the induction time directly from the initial temperature gradient is useful to obtain an accurate ξ.

Rearranging the last row of Equation 2.17 and Equation 2.18, the energy conservation equation becomes

$$\frac{\partial}{\partial t}\left[-P+\frac{\rho u^2}{2}+\rho\sum_{i=1}^{N}(Y_i h_i)\right]+\frac{\partial}{\partial x}\left\{\left[\frac{\rho u^2}{2}+\rho\sum_{i=1}^{N}(Y_i h_i)\right]u\right\}=\frac{\partial}{\partial x}\left(\dot{q}''+\Phi\right). \tag{3.5}$$

Before ignition, the fluid velocity is almost at rest, so the terms with u in Equation 3.5 can be negligible. Note that the viscous dissipation term, Φ, is also negligible when $u = 0$ as in Equation 2.21. The pressure is almost constant over the time before ignition, so $(\partial P/\partial t)$

term is very small compared to other terms. Then, the energy conservation before ignition can be simplified as

$$\frac{\partial}{\partial t}\left[\rho\sum_{i=1}^{N}(Y_i h_i)\right] = \frac{\partial}{\partial x}\left(\lambda\frac{\partial T}{\partial x}\right), \tag{3.6}$$

with the heat flux model introduced in the previous chapter (Equation 2.20). In the heat flux model equation, the heat flux by species diffusion is neglected, as the mixture composition is homogeneous. The enthalpy term can be rewritten using the standard enthalpy of formation as

$$\frac{\partial}{\partial t}\left[\rho\sum_{i=1}^{N}\left(Y_i h_i^0 + Y_i\int_{T_0}^{T} c_{p,i}dT\right)\right] = \frac{\partial}{\partial x}\left(\lambda\frac{\partial T}{\partial x}\right), \tag{3.7}$$

where h_i^0 is the standard enthalpy of formation of species i, and T_0 is the standard temperature, and $c_{p,i}$ is the specific heat at constant pressure of species i. Then, the equation becomes

$$-\dot{Q} + \frac{\partial}{\partial t}\left[\rho\sum_{i=1}^{N}\left(Y_i\int_{T_0}^{T} c_{p,i}dT\right)\right] = \frac{\partial}{\partial x}\left(\lambda\frac{\partial T}{\partial x}\right), \tag{3.8}$$

where $\dot{Q}$ is the heat release rate per unit volume by chemical reaction.

The order of magnitude estimation of each term in Equation 3.8 during the induction time of a hot mixture yields that the heat conduction term is much smaller than other terms, so the equation becomes

$$\frac{\partial}{\partial t}\left[\rho\sum_{i=1}^{N}\left(Y_i\int_{T_0}^{T} c_{p,i}dT\right)\right] = \dot{Q}. \tag{3.9}$$

Therefore, during the induction time, the spatial temperature profile can be estimated by only chemical reaction term of each location. The value of ξ based on the temperature distribution in the end of the induction time is more accurate value than that from the initial temperature gradient, as it includes the effect of the chemical reaction during the induction time.

Figure 3.4 shows the evolution of temperature profiles calculated directly from Equation 3.9 for a stoichiometric 50%H_2-50%CO/air mixture at 1180 K and 50 atm with a 5 mm hot spot. The temperature in the center of hot spot was 1200 K. For the chemical reaction calculation, a 12-species skeletal chemical kinetic mechanism of the H_2/CO combustion developed from GRI-Mech 3.0 (Smith et al., 1999) was used. The temperature in the center of hot spot increases faster than that of boundary of hot spot, as the ignition delay time decreases exponentially with the temperature increment.

Effective reaction propagation

The normalized reactivity gradient can be simply expressed as the ratio of a to u_r. When a and u_r are on the same order of magnitude, the reaction and sound waves resonate and the

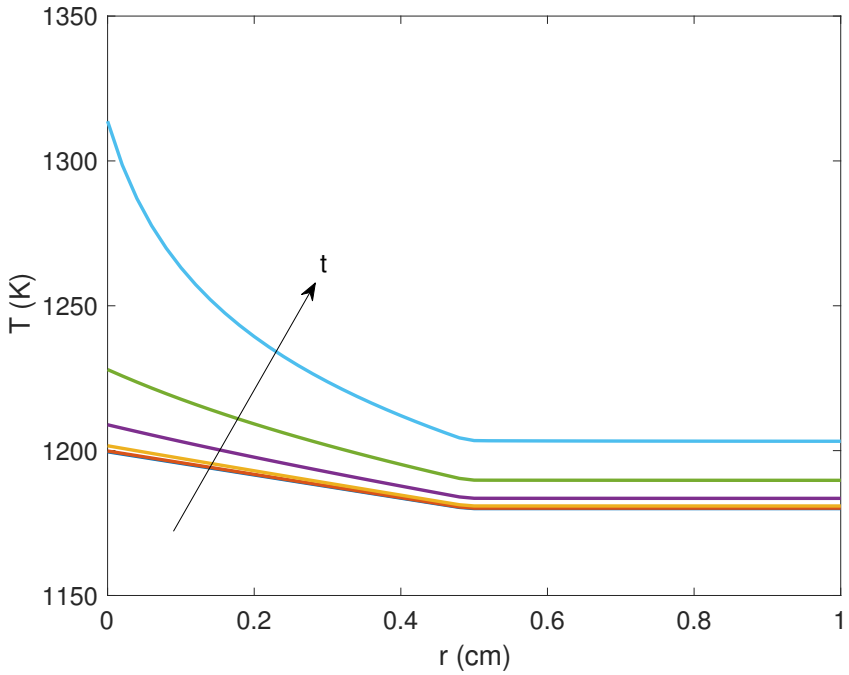

Figure 3.4: Evolution of temperature profile for a stoichiometric 50%H_2-50%CO/air mixture at 1180 K and 50 atm with a 5 mm hot spot. The time intervals between each line are 10 μs.

detonation is initiated. As the variation of sound speed is relatively small compared to that of reaction front propagation speed, the reaction propagation speed is a key factor to decide the detonation initiation.

The spatial distribution of reaction propagation speed can be obtained from the temperature profile in the end of the induction time. Then, the effective reaction front propagation speed at $r = L$ is proposed as

$$u_{eff}(L) = \frac{1}{L}\int_0^L u_r(r)dr, \tag{3.10}$$

where L is the characteristic location. The effective reaction front propagation is an integral value, and represents the averaged reaction propagation speed from 0 to L. Then, the integral normalized reactivity gradient, ξ_{eff}, at location L is defined as

$$\xi_{eff}(L) = \frac{a}{u_{eff}(L)}. \tag{3.11}$$

Therefore, when u_{eff} approaches to the sound speed, the integral reactivity gradient is on the order of unity resulting in a detonation initiation. Figure 3.5 shows that the value of u_{eff} for different characteristic lengths from 0 to 0.5 cm. The mixture was the same as

the previous case, a stoichiometric 50%H_2-50%CO/air mixture at 1180 K and 50 atm with a 5 mm hot spot. The bounds of sound speed are approximately 750 and 1000 m/ for this condition, and shown in the figure with dashed lines. The values of u_{eff} are within the bounds of sound speed when $L \sim 0.15$ cm. Thus, the value of integral reactivity gradient at $L \sim 0.15$ cm is on the order of unity. Note that this result is directly from the initial values without any complex numerical simulations.

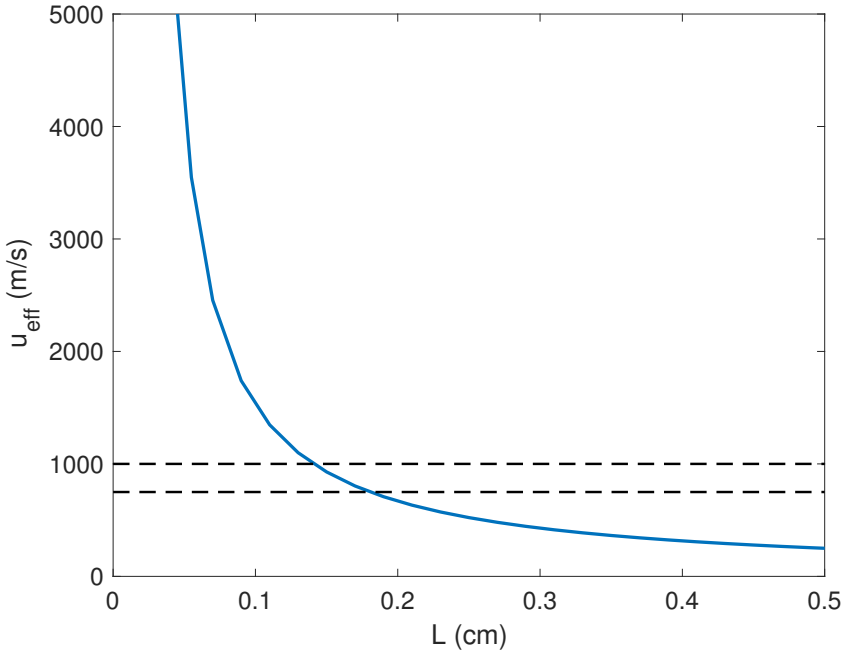

Figure 3.5: Effective reaction front propagation speeds for different characteristic lengths from 0 to 0.5 cm, for a stoichiometric 50%H_2-50%CO/air mixture at 1180 K and 50 atm with a 5 mm hot spot. Dashed lines correspond to bounds of sound speed, $a = 750$ and 1000 m/s.

Figure 3.6 shows the A-SURF simulation results with the same conditions and mixture with the previous case. In the simulation result, the reaction propagation is a supersonic deflagration initially, but transitions to the detonation between 0.1 and 0.2 cm. The estimated characteristic length of detonation initiation is ∼0.15 cm, which corresponds to the simulation results. Moreover, when $L < 0.15$, the effective reaction propagation speed is larger than the sound speed, and ξ_{eff} is smaller than the order of unity, which results in a supersonic deflagration. This supersonic deflagration also corresponds to the simulation result.

The method of integral reactivity gradient with the temperature profile after the induction time shows a good agreement with A-SURF simulation. The chemical reaction effect is considered in the method, and a detonation initiation by DDT with the initiation time

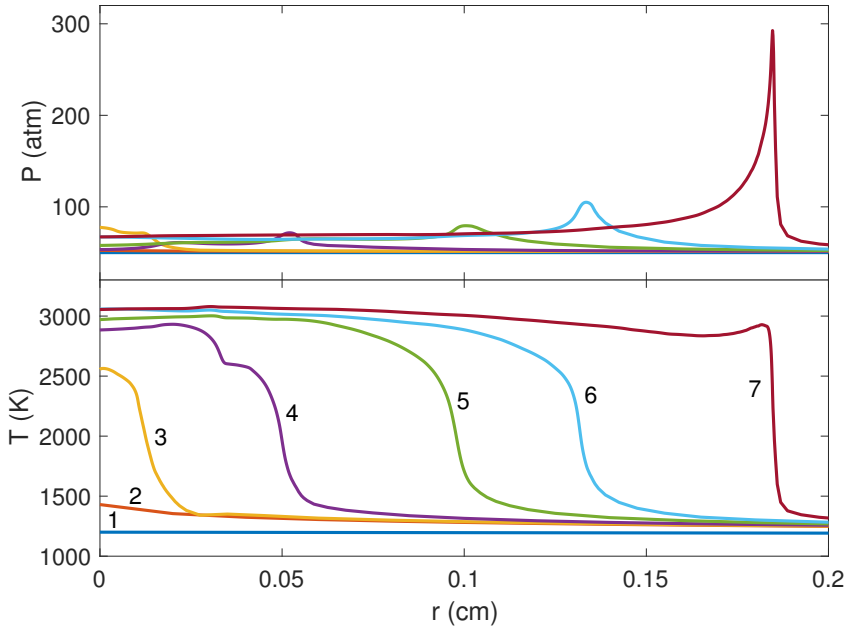

Figure 3.6: Development of pressure and temperature from A-SURF calculation for a stoichiometric 50%H_2-50%CO/air mixture at 1180 K and 50 atm with a 5 mm hot spot. Time sequence 1: 0.00 μs, 2: 51.56 μs, 3: 51.95 μs, 4: 52.73 μs, 5: 53.51 μs, 6: 53.90 μs, 7: 54.29 μs.

also can be estimated directly from the initial conditions without any complex numerical simulations.

3.4 Prediction models using machine learning techniques

This section is based on the final class project report of *IEOR 142 Introduction to Machine Learning and Data Analytics* in Fall 2017 semester by Professor Paul Grigas at the University of California, Berkeley. Discussions with Professor Grigas on machine learning techniques used in the present study are acknowledged.

Motivation

The research on detonation has many barriers. In experiments, facilities are not sustainable for repeating tests due to its high pressure. It is also extremely difficult to set a condition for a detonation experimentally. In the numerical side of research, usually the computational cost is very expensive due to its stiff governing equations. Capturing shock needs small grid size, and it requires very small time step size for the stability reason. Therefore, it is

beneficial to use previous data set to estimate new conditions of detonation initiation by machine learning techniques. This study can be utilized as a primary prediction method of detonation initiation, and also applied to find important variables.

Data set

Eighty-two cases were obtained from ASURF-Parallel calculations for the reaction propagation by a hot-spot with various conditions as shown in Tabel 3.1. The conditions were defined as independent variables, and include temperature of hot spot center, T_h, size of hot spot, r_h, ambient temperature, ambient pressure, domain size, L_d, fuel type, coordinate, and equivalence ratio, ϕ. Due to the lack of data points, some variables were not used in this study, and some variables were normalized with others to avoid the multicollinearity. The dependent variable is the mode of flame propagation: deflagration or detonation.

Table 3.1: Data set of reaction propagation by a hot spot from ASURF-Parallel simulations.

Data #	T_h (K)	T (K)	r_h (cm)	P (atm)	L_d (cm)	Fuel	ϕ	Coordinate	Mode
1	1110	1100	0.6	10	10	H_2	1	Planar	Detonation
2	1130	1100	0.2	10	10	H_2	1	Planar	Deflagration
3	1130	1100	0.6	10	10	H_2	1	Planar	Detonation
4	1150	1100	0.1	10	10	H_2	1	Planar	Deflagration
5	1150	1100	0.6	10	10	H_2	1	Planar	Detonation
6	1150	1100	1.8	10	10	H_2	1	Planar	Detonation
7	1180	1100	0.6	10	10	H_2	1	Planar	Detonation
8	1200	1000	0.6	10	10	H_2	1	Planar	Detonation
9	1200	1100	0.6	10	10	H_2	1	Planar	Detonation
10	1200	1150	0.1	10	10	H_2	1	Planar	Detonation
11	1200	1150	0.2	10	10	H_2	1	Planar	Detonation
12	1200	1150	1	10	10	H_2	1	Planar	Detonation
13	1200	1150	1.8	10	10	H_2	1	Planar	Detonation
14	1200	1150	3.4	10	10	H_2	1	Planar	Detonation
15	1200	1150	8.2	10	10	H_2	1	Planar	Deflagration
16	1200	1185	0.1	10	10	H_2	1	Planar	Detonation
17	1200	1185	0.6	10	10	H_2	1	Planar	Detonation
18	1200	1185	1.8	10	10	H_2	1	Planar	Deflagration
19	1000.5	1000	0.6	10	10	H_2	1	Planar	Detonation
20	1005	1000	0.6	10	10	H_2	1	Planar	Deflagration
21	1005	1000	0.3	10	10	H_2	1	Planar	Deflagration
22	1100	1000	0.6	10	10	H_2	1	Planar	Deflagration
23	1200	800	0.6	10	10	H_2	1	Planar	Deflagration
24	1200	900	0.6	10	10	H_2	1	Planar	Deflagration
25	1200	1000	1	5	40	H_2	0.1	Planar	Deflagration
26	1200	1000	1	5	40	H_2	0.2	Planar	Deflagration
27	1200	1000	1	5	40	H_2	0.3	Planar	Detonation
28	1200	1000	1	5	40	H_2	0.4	Planar	Detonation
29	1200	1000	1	5	40	H_2	0.5	Planar	Detonation
30	1200	1000	1	5	40	H_2	0.6	Planar	Detonation

31	1200	1000	1	5	40	H_2	0.7	Planar	Detonation
32	1200	1000	1	5	40	H_2	0.8	Planar	Detonation
33	1200	1000	1	5	40	H_2	0.9	Planar	Detonation
34	1200	1000	1	5	40	H_2	1	Planar	Detonation
35	1200	1000	1	5	40	H_2	1.1	Planar	Detonation
36	1200	1000	1	5	40	H_2	1.2	Planar	Detonation
37	1200	1000	1	5	40	H_2	1.3	Planar	Detonation
38	1200	1000	1	5	40	H_2	1.5	Planar	Detonation
39	1200	1000	1	5	40	H_2	1.7	Planar	Detonation
40	1200	1000	1	5	40	H_2	1.9	Planar	Detonation
41	1200	1000	1	5	40	H_2	2.1	Planar	Detonation
42	1200	1000	1	5	40	H_2	2.5	Planar	Detonation
43	1200	1000	1	5	40	H_2	3	Planar	Detonation
44	1200	1000	1	5	40	H_2	3.5	Planar	Detonation
45	1200	1000	1	5	40	H_2	3.8	Planar	Detonation
46	1200	1000	1	5	40	H_2	3.9	Planar	Detonation
47	1200	1000	1	5	40	H_2	4	Planar	Detonation
48	1200	1000	1	5	40	H_2	4.2	Planar	Detonation
49	1200	1000	1	5	40	H_2	4.5	Planar	Detonation
50	1200	1000	1	5	40	H_2	5	Planar	Detonation
51	1200	1000	1	5	40	H_2	5.5	Planar	Detonation
52	1200	1000	1	5	40	H_2	6	Planar	Deflagration
53	1200	1000	1	5	40	H_2	7	Planar	Deflagration
54	1200	1000	1	5	40	H_2	8	Planar	Deflagration
55	1200	1000	1	5	40	H_2	9	Planar	Deflagration
56	1200	1000	1	5	40	H_2	10	Planar	Deflagration
57	1180.4	1180	0.01	50	5	H_2-CO	1	Spherical	Deflagration
58	1180.8	1180	0.02	50	5	H_2-CO	1	Spherical	Deflagration
59	1181.2	1180	0.03	50	5	H_2-CO	1	Spherical	Deflagration
60	1181.6	1180	0.04	50	5	H_2-CO	1	Spherical	Deflagration
61	1182	1180	0.05	50	5	H_2-CO	1	Spherical	Detonation
62	1184	1180	0.2	50	5	H_2-CO	1	Spherical	Detonation
63	1184	1180	0.05	50	5	H_2-CO	1	Spherical	Deflagration
64	1188	1180	0.2	50	5	H_2-CO	1	Spherical	Detonation
65	1192	1180	0.1	50	5	H_2-CO	1	Spherical	Deflagration
66	1192	1180	0.01	50	5	H_2-CO	1	Spherical	Deflagration
67	1192	1180	0.2	50	5	H_2-CO	1	Spherical	Detonation
68	1192	1180	0.3	50	5	H_2-CO	1	Spherical	Detonation
69	1192	1180	0.03	50	5	H_2-CO	1	Spherical	Deflagration
70	1192	1180	0.05	50	5	H_2-CO	1	Spherical	Deflagration
71	1192	1180	0.07	50	5	H_2-CO	1	Spherical	Deflagration
72	1192	1180	0.15	50	5	H_2-CO	1	Spherical	Detonation
73	1192	1180	0.25	50	5	H_2-CO	1	Spherical	Detonation
74	1200	1188	0.3	50	5	H_2-CO	1	Spherical	Detonation
75	1200	1192	0.2	50	5	H_2-CO	1	Spherical	Detonation
76	1200	1196	0.2	50	5	H_2-CO	1	Spherical	Detonation
77	1200	1198	0.05	50	5	H_2-CO	1	Spherical	Deflagration
78	1350	1300	0.1	50	5	H_2-CO	1	Spherical	Detonation
79	1350	1320	0.1	50	5	H_2-CO	1	Spherical	Detonation
80	1200	1180	0.5	50	4	H_2-CO	1	Spherical	Detonation

81	1200	1180	2	50	10	H_2-CO	1	Spherical	Detonation
82	1300	1100	2	50	10	H_2-CO	1	Spherical	Detonation

Set-up and baseline model

The data randomly split into training and test sets. Models were developed from the training set, and validated using the test set. 75% of data were used as a training set, and 25% of data were used as a test set. The baseline model was based on the percentage of detonation cases in the training set, and the accuracy of the baseline model is about 87%. The accuracy of baseline model was comparably high, because obtained data are deflected to detonation cases.

The temperature gradient is a key factor of the reaction propagation mode as discussed using the reactivity gradient theory. Thus, using the temperature difference of hot spot instead of the temperature of hot spot center represents the physical phenomena better. The temperature difference of hot spot was normalized by ambient temperature as

$$\Delta T^* = \frac{T_h - T}{T}, \tag{3.12}$$

where T is the ambient temperature. Moreover, domain length and coordinate were not used for the data training, as the effect of these were negligible. Therefore, independent variables were the normalized temperature difference, ΔT^*, size of hot spot, ambient temperature, ambient pressure, fuel, and equivalence ratio.

The predictive models were developed using the R software (R Core Team, 2017) from the training data set. As this is a classification problem, i.e., predicting a binary outcome: detonation or deflagration, the logistic regression and CART (classification and regression trees) models are considered. The detailed theory on these models with R examples can be found in James et al. (2013).

Logistic regression

In the logistic regression model, only the cases with H_2 were considered due to the small number of data for H_2-CO. A logistic regression model was developed by learning the training data set as

$$\begin{aligned} Pr(Y = 1) &= \frac{1}{1 + e^{-Z}}, \\ Z &= -23.18 + 11.17\Delta T^* + 0.02601T - 0.6730d_h - 0.3156P - 0.4906\phi, \end{aligned} \tag{3.13}$$

where Pr is the probability, Y is the dependent variable, and Z is the negative exponentiation of the logistic function. The units of independent variables are as in Table 3.1. In this

model, the dependent variable is modeled as a Bernoulli random variable, i.e., $Y = 1$ for the detonation mode and $Y = 0$ for the deflagration mode. Therefore, if $Pr(Y = 1) > 0.5$, the propagation mode is likely to be a detonation wave. When $Pr(Y = 1) < 0.5$, a deflagration wave is estimated.

Figure 3.7 shows the distribution of dependent variables of the training data set calculated by the developed logistic regression model. The model successfully classified the data into the detonation mode and deflagration mode. Using the test data set, the accuracy of this model was calculated: 0.7143. The number of data set was not sufficiently large and the independent variables were clustered (not scattered), so the prediction was less accurate.

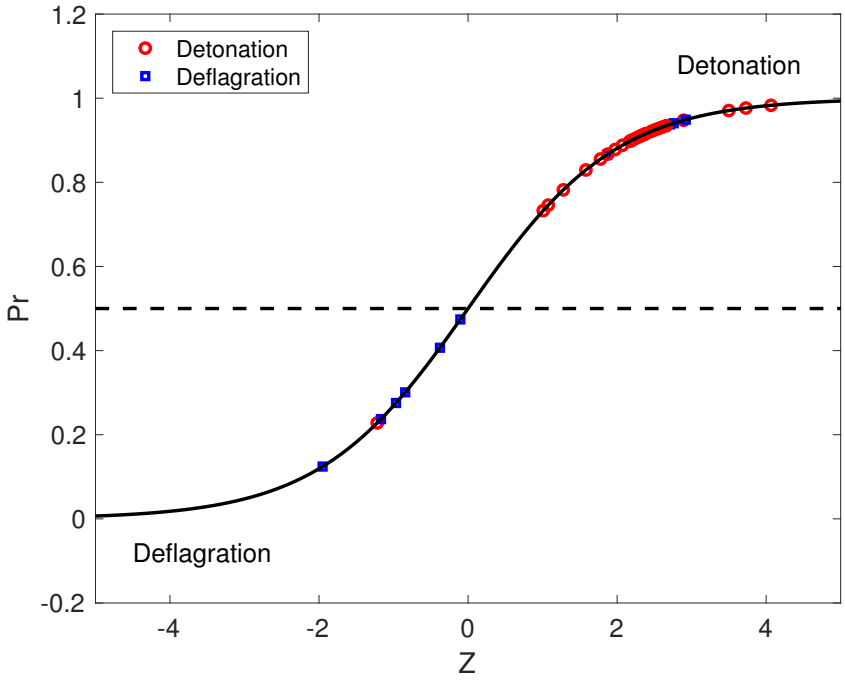

Figure 3.7: Distribution of dependent variables calculated by the developed logistic regression model. Solid line corresponds to the logistic function, $\frac{1}{1+e^{-Z}}$, and dashed line is the cutoff line, $Pr = 0.5$.

The R software shows "p-value" for each independent variable, and the values for this model are shown in Table 3.2. A "p-value" is the boundary point where the significance considerably changes. A small "p-value" indicates that the corresponding independent variable is a significant coefficient. The ambient temperature and equivalence ratio were dominant factors, as their values were relatively small. Since the reactivity of a gas mixture is highly sensitive to the ambient temperature and equivalence ratio, the result is physically appropriate. Moreover, the reactivity of gas mixture more depends on temperature than pressure, and "p-values" show the same tendency. Even though this machine learning technique does

Table 3.2: Calculated "p-value" of each independent variable for logistic regression model from R.

Independent variable	p-value
ΔT^*	0.3712
T	0.0470
d_h	0.1332
P	0.4549
ϕ	0.0287

not include the physics or mechanism of the phenomena in the model development process, the developed model can predict the physics of the phenomena.

Classification and regression trees (CART)

The classification and regression trees (CART) model creates a tree by splitting on independent variables for the prediction. A CART model was developed using the R software. The model requires a value of complexity parameter, which prunes the splits of tree that do not impact the model sufficiently. A small complexity parameter has more splits in the tree. In the present model, the value of complexity parameter was chosen from the cross-validation method. The training data was divided into five different groups, and the models were trained by removing one group for each case. The averaged losses of prediction were calculated from the models for various complexity parameters, and the optimal value for the complexity parameter was 0.02.

Figure 3.8 shows the developed CART model. The optimal model includes only two independent variables, the size of hot spot, and the ambient temperature. The detonation mode is predicted when the hot spot size larger than 0.085 cm with the ambient temperature higher than 1125 K. If the size of hot spot is larger than 0.8 cm, the model predict a detonation regardless of other independent variables. The accuracy of the CART model calculated from the test data set was 0.7619. For better model development, data points in a wide range of independent variables are required.

Summary and future work

The prediction models using machine learning techniques for detonation occurrence were developed from the training of numerical simulation result data set. Even though the prediction was not very accurate due to the small number of data points and clustering of independent variables, the modes of flame propagation could be estimated roughly without computationally expensive numerical simulations. Moreover, the machine learning techniques can be helpful to understand the real physics of non-linear and multi-dimensional variable problems without any physical model in the techniques.

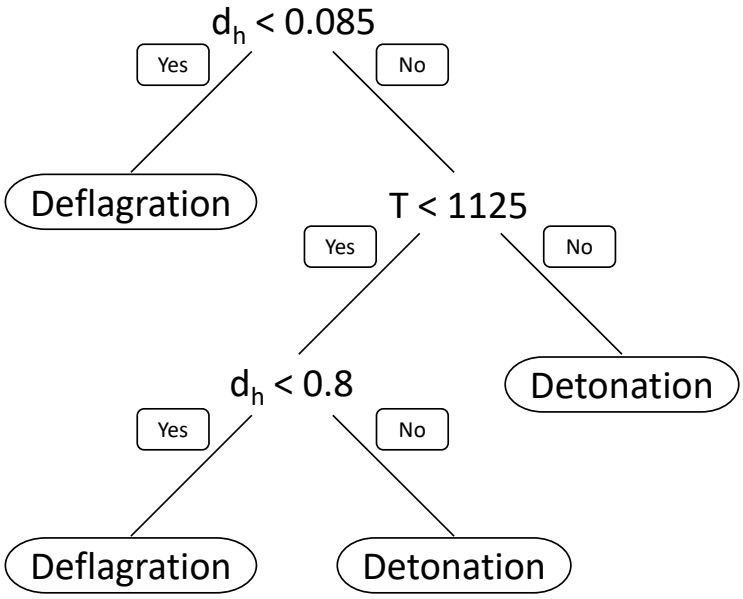

Figure 3.8: Optimal CART model developed using R.

For better prediction, independent variables should be reorganized, such as using log or exponential values, normalizing, and scaling. As the independent variables used in this study were not scattered, more data with wide range of independent variables are needed. The models can be easily modified if more data points are obtained, so these models can be sustainably used for the future research. Furthermore, including statistical learning models directly into the numerical simulation of reacting flows will possibly bring a better and faster numerical model with new insights.

Chapter 4

Detonation Propagation

This chapter is based on the manuscript in preparation (Ryu et al., 2018b). The study is a numerical investigation of detonation propagation, especially in fuel-stratification layers.

4.1 Introduction

Detonation propagation in inhomogeneous mixtures is practically important in real-world accident scenarios, since explosion accidents likely occur under the fuel-stratified conditions rather than premixed conditions. Therefore, the behavior of detonation propagation in inhomogeneous unburnt mixtures has been actively studied.

Thomas et al. (1991) experimentally studied detonation propagation in concentration gradients, and found that the properties of propagated detonation were rapidly adjusted to the Chapman-Jouguet (CJ) values of the local gas mixture. A numerical study was performed for detonation propagation along mixture composition gradients, and explained the effects of the gradient on the detonation cell size by Kessler et al. (2012). Ettner et al. (2013) also numerically investigated the Mach reflection effects on detonation propagation in the stratification layers. Recently, multiple experiments of H_2/air detonation propagation were performed to examine the influences of fuel-stratification layers. Deficits in detonation propagation speed by concentration gradients were experimentally measured by Boeck et al. (2016), and the maximum speed deficit was 9% of the CJ speed. The critical value of H_2 concentration for detonation propagation was also investigated experimentally by Grune et al. (2017).

Another approach to study the detonation propagation in inhomogeneous mixture is using inert gases. Experimental results of detonation propagation through inert gases (Gavrilenko et al., 1982; Teodorczyk and Benoan, 1996) showed similar behavior with studies using fuel-stratification layers. Houim and Fievisohn (2017) investigated the influence of acoustic impedance ratio between the inert and reactant gases numerically.

However, previous studies on detonation propagation focused on the overall effects of the inhomogeneous unburned mixture, and did not consider the transient states. Some studies (Shi et al., 2016, 2017a) investigated the transient states in the inhomogeneous mixtures, but these numerical results were for laminar flame propagation. A recent investigation (Ryu et al., 2018a) focused on the transient states of detonation propagation, but mainly considered the effect of water vapor concentration gradient on detonation suppression. In this work, the numerical study mainly explores the transient process of detonation propagation through fuel-stratification layers and aims to answer:

- How does fuel stratification layer affect detonation propagation properties?
- How do directions (e.g., from rich to lean) and degrees of stratification influence the detonation speed and the leading shock pressure?
- Does the same stratified detonation behavior hold for different fuel species?
- What is the detailed mechanism causing the deficit or surplus of detonation property compared to that of local homogeneous CJ detonation in fuel-stratification layers?

To answer these questions, numerical simulations of fuel-stratified hydrogen/air and propane/air detonations were performed and compared to the corresponding local homogeneous CJ detonation (HD) properties. Trends in lean-to-rich and rich-to-lean stratifications were compared, and several models were used to understand the mechanism causing detonation property deficit or surplus in the stratification layers. All simulations were performed in a one-dimensional planar domain to concentrate on the interaction between leading shock and reaction front, so multi-dimensional effects and wall effects were not considered.

4.2 Numerical setup

To simulate the transient change of detonation wave through the fuel-stratification layer, ASURF-Parallel (Chen, 2009; Shi, 2017) was used. Figure 4.1 shows a schematic setup of stratified detonation (SD) simulations. A homogeneous CJ detonation at equivalence ratio ϕ_1 was propagating to the right side of the one-dimensional planar domain initially. Fuel-stratification was imposed in front of the homogeneous detonation wave from $x = 0$ to d_s cm. This fuel-stratified region is referred to as the fuel-stratification layer. The initial detonation front was at $x \sim 0^-$ cm, so the effects of species diffusion before the reaction were minimized. In the fuel-stratification layer, the equivalence ratio is increased or decreased continuously to a certain equivalence ratio, ϕ_2. On the right side of the stratification layer, the equivalence ratio, ϕ_2, is uniform to the right end of the domain. A reflected boundary condition was applied to the left end of the domain to sustain the detonation propagation, and a transmissive boundary condition was used in the right end of the domain to avoid disturbances from the reflected acoustic waves.

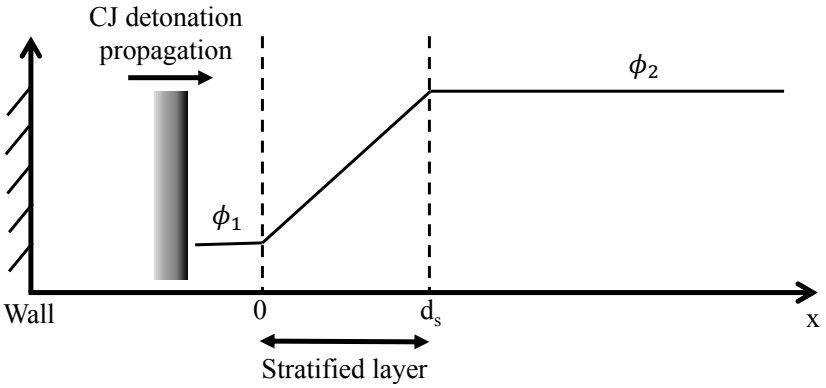

Figure 4.1: Schematic setup of detonation propagation through stratification layer in 1-D planar domain.

For hydrogen/air combustion, a 9-species skeletal chemical kinetic model (Burke et al., 2012) was used, and the simulations were performed with initial temperature, T, of 1000 K and pressure, P, of 5 atm. For propane/air combustion, a 27-species reduced skeletal model (Chen and Chen, 2018) was utilized with initial states of $T = 1150$ K and $P = 40$ atm to have a similar detonation structure with hydrogen/air detonation. The initial temperature and pressure of unburnt mixture remained the same until the detonation wave passed. The simulation domain was 40 cm long with the minimum grid size of 9.77×10^{-7} m, and the time step was 5×10^{-11} s. Figure 4.2 shows an example of the initial state for hydrogen/air detonation simulations. Since the burned mixture side is not the region of interest in current study, equivalence ratio is presented only in the unburnt side.

In addition to ASURF-Parallel, the Shock and Detonation Toolbox (Browne et al., 2004; Kao and Shepherd, 2004) were utilized to calculate the CJ speed, S_{CJ}, and von Neumann (VN) spike pressure, P_{VN}, using the same chemical kinetic models and conditions for reference. Some calculated values of hydrogen/air and propane/air detonations using A-SURF and the Shock and Detonation Toolbox are presented in Table 4.1. The calculated properties from A-SURF simulation of homogeneous CJ detonation were very close to the values from the Shock and Detonation Toolbox.

In this study, numerical simulations were performed for lean-to-rich and rich-to-lean stratified detonation with several thickness of the stratification layer to examine the effects of direction and degree of fuel-stratification. In order to investigate the interaction between the leading shock front and the reaction front in the stratification layer, the length of stratification layer should be larger than the induction length of the Zel'dovich-Neumann-Döring (ZND) detonation structure (Zel'dovich, 1940a; von Neumann, 1942; Döring, 1943). Two sizes of stratification layer, i.e., 0.1 and 1.0 cm, were used, since the typical induction length of this simulation condition is on the order of 10^{-5} m. Cases of hydrogen/air and propane/air were compared, and the transient process was analyzed with simple models to elucidate the detailed mechanism causing change in detonation properties compare to the

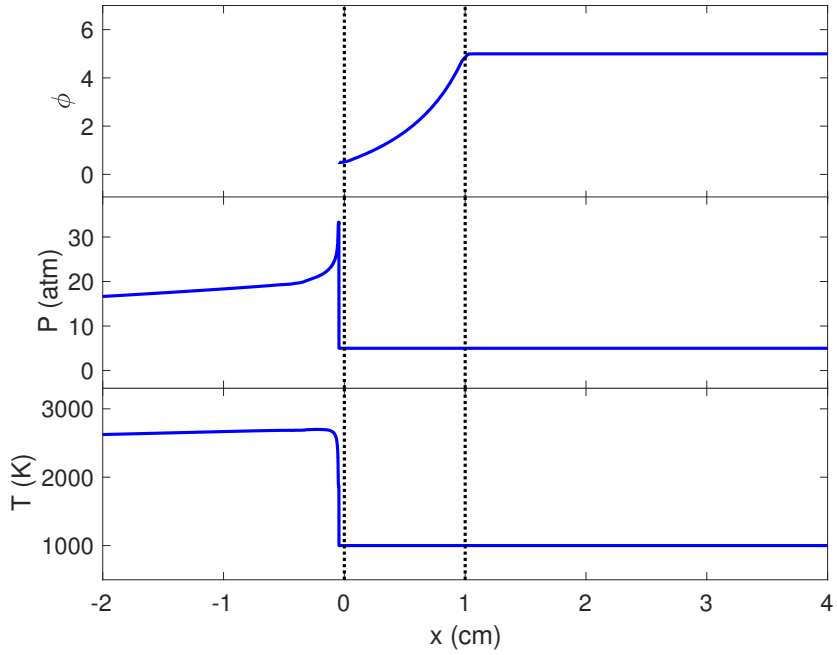

Figure 4.2: Example profiles of equivalence ratio in unburnt side, pressure, and temperature at the initial state of simulation.

Table 4.1: Calculated CJ speeds, VN spike pressures using A-SURF and Shock and Detonation Toolbox.

Fuel	ϕ	S_{CJ} (m/s)		P_{VN} (atm)	
		A-SURF	Toolbox	A-SURF	Toolbox
H_2	0.6	1720	1733	35.55	35.86
	1.0	1928	1946	39.76	40.36
	1.4	2033	2054	40.12	40.64
C_3H_8	0.6	1635	1672	282.2	297.9
	1.0	1842	1859	362.0	377.2
	1.4	1919	1923	398.6	410.7

values of corresponding homogeneous detonation.

4.3 Results

In explosion accidents, the ignition can be initiated both in the lean and rich mixture sides. Therefore, detonation propagations in both lean-to-rich and rich-to-lean stratification layers were simulated and compared. In the ZND structure, the induction zone contains unburnt mixture at high pressure, so the equivalence ratio at the induction zone, ϕ_i, can be considered as the local equivalence ratio at flame front. In the simulation, the time scale of detonation

propagation in the stratification layer was very small compared to the species diffusion time scale, so the change of local equivalence ratio due to the diffusion processes can be negligible.

Hydrogen/air detonation

Figure 4.3 presents the detonation propagation speeds, D, of hydrogen/air lean-to-rich stratified detonation and HDs. The detonation propagated from the mixture with $\phi_1 = 0.6$ (lean) to $\phi_2 = 1.4$ (rich) mixture. The detonation propagation speeds at each location and corresponding equivalence ratios at the induction zone were calculated. Homogeneous detonation propagation speeds were also calculated using A-SURF for 9 equivalence ratios over a range of 0.6 – 1.4. Note that the SD properties rapidly approach to the HD properties after the stratification layer, but only results in the stratification layer were shown for clarity. For the stratification layer size of 0.1 cm, the speed of stratified detonation propagation in the stratification layer was slower than the that of the corresponding HD speed, and the maximum deficit was ∼5.1% of HD speed. When the size of stratification layer became 1.0 cm, the SD speed was slightly lower than its corresponding HD speed, and the maximum deficit was only ∼0.9%. The deceleration of SD speed was larger for the smaller size of fuel-stratification layer.

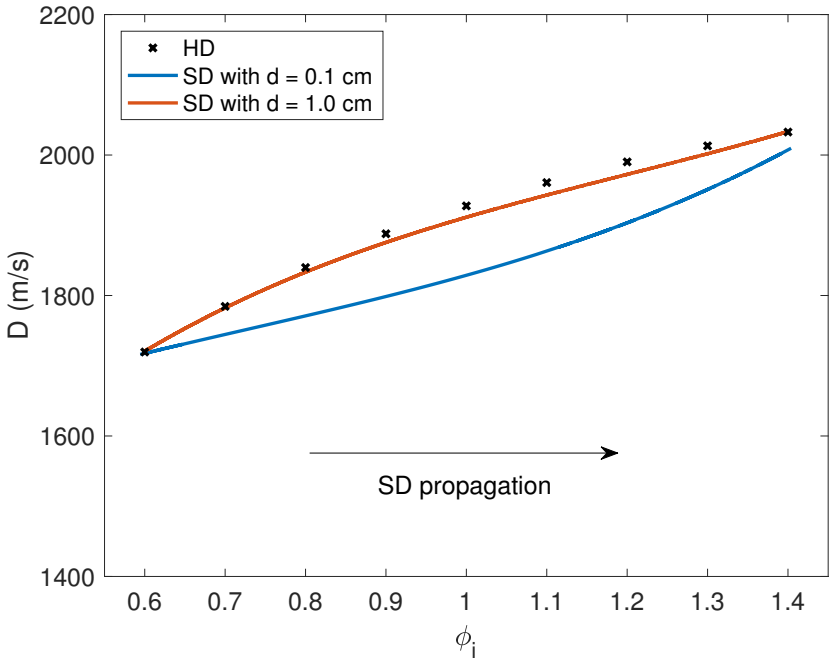

Figure 4.3: Computed detonation propagation speeds of H_2/air HD and SD with $d_s = 0.1$ and 1.0 cm. SD propagates from $\phi_1 = 0.6$ (lean) to $\phi_2 = 1.4$ (rich).

For the safety application of detonation, the leading shock pressure, P_{LS}, is the center of interest. The leading shock pressure traces of the stratified and homogeneous detonations are

shown in Figure 4.4. Similar to the trend of detonation speed, the leading shock strength of stratified detonation was mitigated compared to that of HD, and the mitigation effect was larger for the smaller layer size. The maximum deficits were about 9.9% and 1.4% of homogeneous shock pressure for $d_s = 0.1$ and 1.0 cm, respectively.

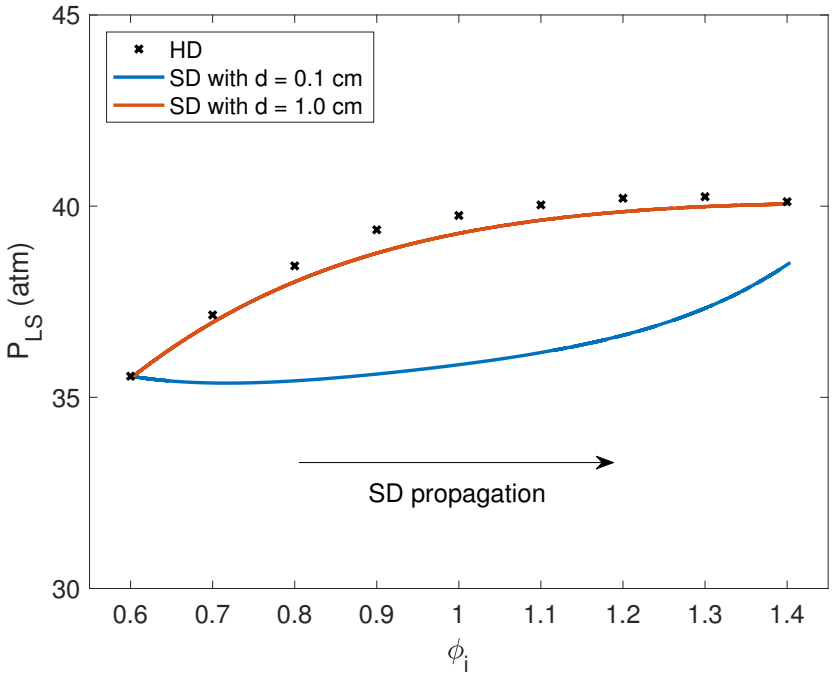

Figure 4.4: Computed leading shock pressures of H_2/air HD and SD with $d_s = 0.1$ and 1.0 cm. SD propagates from $\phi_1 = 0.6$ (lean) to $\phi_2 = 1.4$ (rich).

In the simulations of hydrogen/air rich-to-lean stratified detonation, the trend was opposite from the lean-to-rich SD cases. Figure 4.5 and Figure 4.6 show speeds and leading shock pressures of the rich-to-lean SD calculated from the simulations. The calculations were performed for the same stratification layer sizes with the lean-to-rich SD cases. The equivalence ratios before and after the stratification layer were $\phi_1 = 1.4$ (rich) and $\phi_2 = 0.6$ (lean). The speeds of the stratified detonation were faster than those of HD, and the maximum surpluses in speed are around 3.8% and 2.5% of HD speed for $d_s = 0.1$ and 1 cm, receptively. Leading shock pressures were also higher for SD cases than HD cases, and about 9.0% and 5.2% surpluses of HD leading shock pressure (VN pressure) were observed for the stratification layer sizes of 0.1 and 1.0 cm, receptively.

Both lean-to-rich and rich-to-lean stratified detonations tend to be adjusted to the properties of local homogeneous CJ detonation to avoid the unstable detonation state. However, due to the fuel-stratification direction and degree, the properties of SD have deficits or surpluses of the local corresponding HD values.

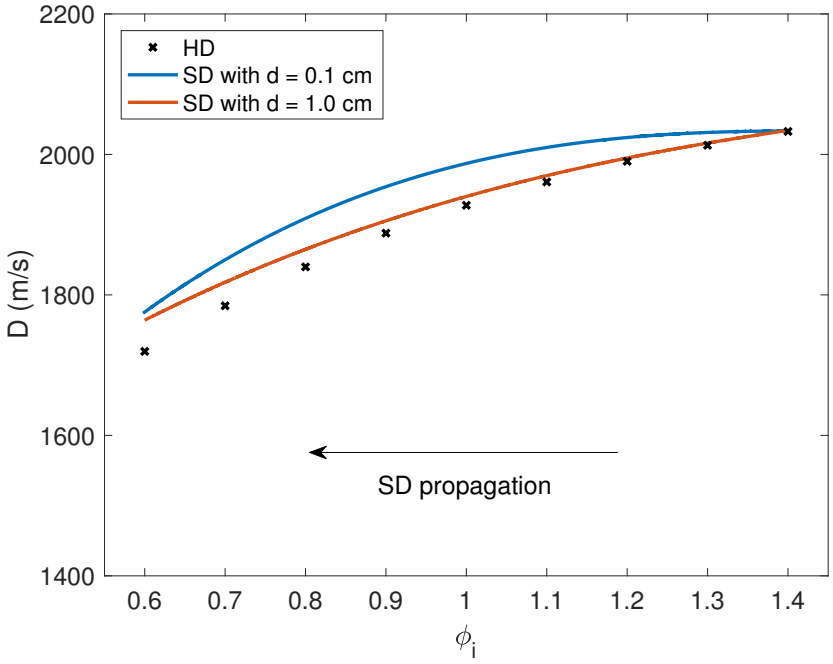

Figure 4.5: Computed detonation propagation speeds of H_2/air HD and SD with $d_s = 0.1$ and 1.0 cm. SD propagates from $\phi_1 = 1.4$ (rich) to $\phi_2 = 0.6$ (lean).

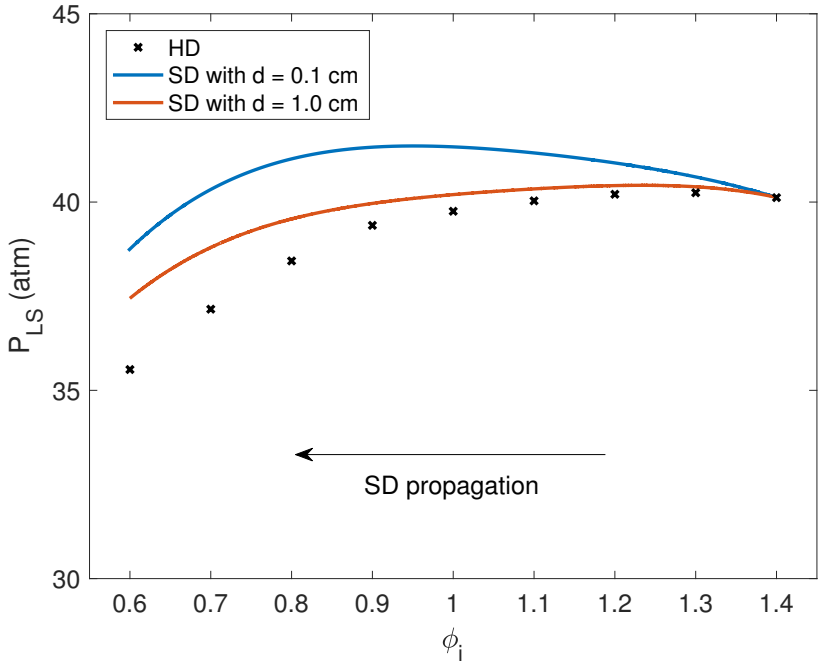

Figure 4.6: Computed leading shock pressures of H_2/air HD and SD with $d_s = 0.1$ and 1.0 cm. SD propagates from $\phi_1 = 1.4$ (rich) to $\phi_2 = 0.6$ (lean).

Propane/air detonation

Propane has different properties from hydrogen, and these may affect the properties of detonation propagation in the fuel-stratification layer. Due to the difficulty of detonation initiation at the same temperature and pressure of H_2 detonation cases, different initial temperature and pressure were used as specified in Section 4.2. These conditions were set to initiate detonation waves in the same bounds of lean and rich equivalence ratios of hydrogen cases. Therefore, ϕ_1 and ϕ_2 were the same as the hydrogen/air detonation cases. In this section, simulations with propane are presented, and the results were distinguishable from those of hydrogen/air cases.

For propane/air lean-to-rich detonation propagation, ϕ_1 (lean) was 0.6 and ϕ_2 (rich) was 1.4. The SD propagation speeds are shown in Figure 4.7. The case with $d_s = 0.1$ cm had ∼2.6% maximum surplus, while the case with $d_s = 1.0$ cm had ∼2.0% maximum deficit of HD propagation speed. Figure 4.8 shows the leading shock pressures for lean-to-rich detonation propagation. For $d_s = 1.0$ cm, the result was similar to the lean-to-rich case of hydrogen/air SD, and the maximum deficit was about 4.3% of HD leading shock pressure. However, the case with $d_s = 0.1$ cm, the trend of leading shock pressure through the stratification layer was different from other cases. Initially, the shock pressure was smaller than corresponding HD shock pressure, but near the stoichiometric point, the shock pressure overshot the corresponding shock pressure of HD. Then, the leading shock pressure oscillated in the rich mixture zone over the HD shock pressure.

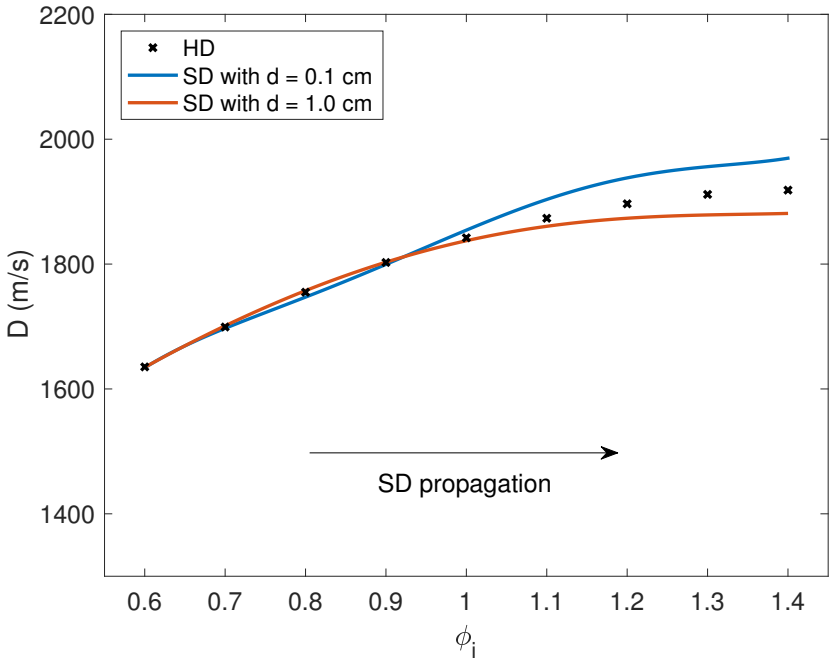

Figure 4.7: Computed detonation propagation speeds of C_3H_8/air HD and SD with $d_s = 0.1$ and 1.0 cm. SD propagates from $\phi_1 = 0.6$ (lean) to $\phi_2 = 1.4$ (rich).

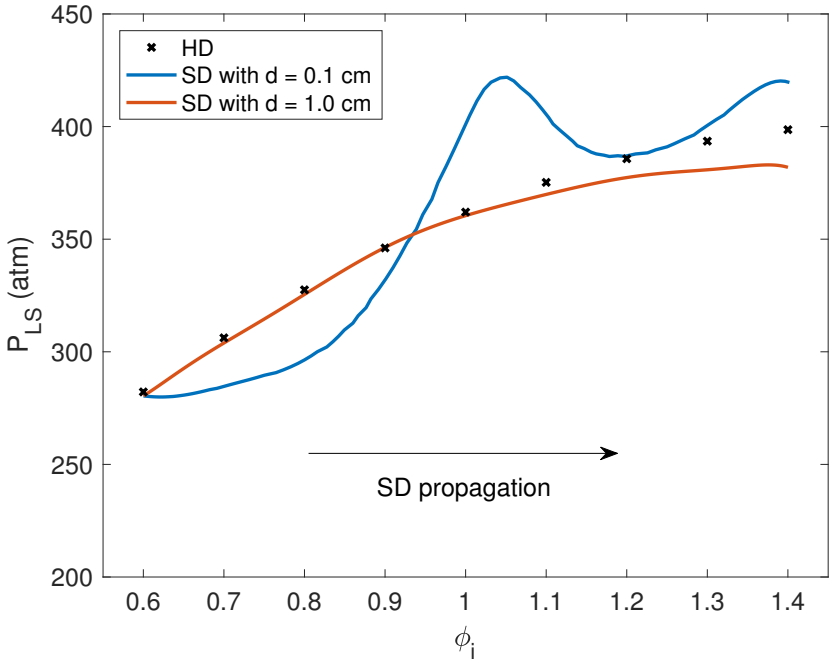

Figure 4.8: Computed leading shock pressures of C_3H_8/air HD and SD with $d_s = 0.1$ and 1.0 cm. SD propagates from $\phi_1 = 0.6$ (lean) to $\phi_2 = 1.4$ (rich).

Figures 4.9 and 4.10 show the simulation results of propane/air rich-to-lean SD cases with $\phi_1 = 1.4$ and $\phi_2 = 0.6$. The SD propagation speed in the 0.1 cm stratification layer was slightly faster in the rich mixture area, but became slower than that of HD propagation speed in the leaner side. The maximum deficit was about 3.5% of HD speed. In the 1 cm stratification layer, the SD propagated almost at the same speed with corresponding HD speed, and the maximum deficit was less than 1% of HD speed. The leading shock pressure was slightly higher than corresponding HD pressure ($\sim$1.3%) in the 0.1 cm stratification layer, but overall the SD leading shock pressures for both $d_s = 0.1$ and 1.0 cm cases were almost the same as corresponding HD shock pressures.

4.4 Discussion

Effect of shock reflection

In the ZND detonation structure model, the leading shock is ahead of the reaction front. When the detonation wave propagates into the stratification layer, the leading shock is affected by the layer first. Therefore, the leading shock behavior in the stratification layer should be first investigated to understand SD. In acoustics theory, shock reflections occur when the shock wave experiences a specific acoustic impedance difference across the stratification layer. The amounts of reflection and transmission can be predicted with a

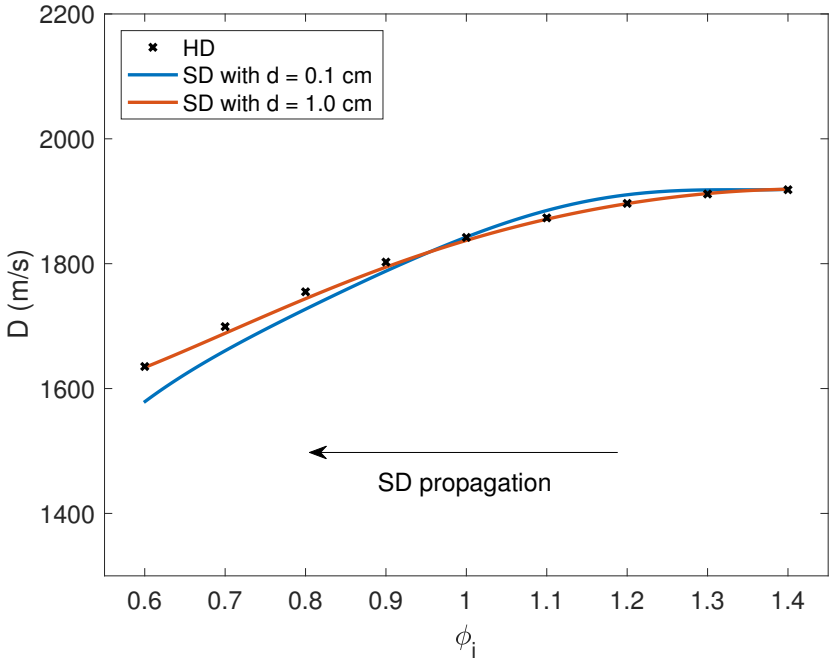

Figure 4.9: Computed detonation propagation speeds of C_3H_8/air HD and SD with $d_s = 0.1$ and 1.0 cm. SD propagates from $\phi_2 = 1.4$ (rich) to $\phi_1 = 0.6$ (lean).

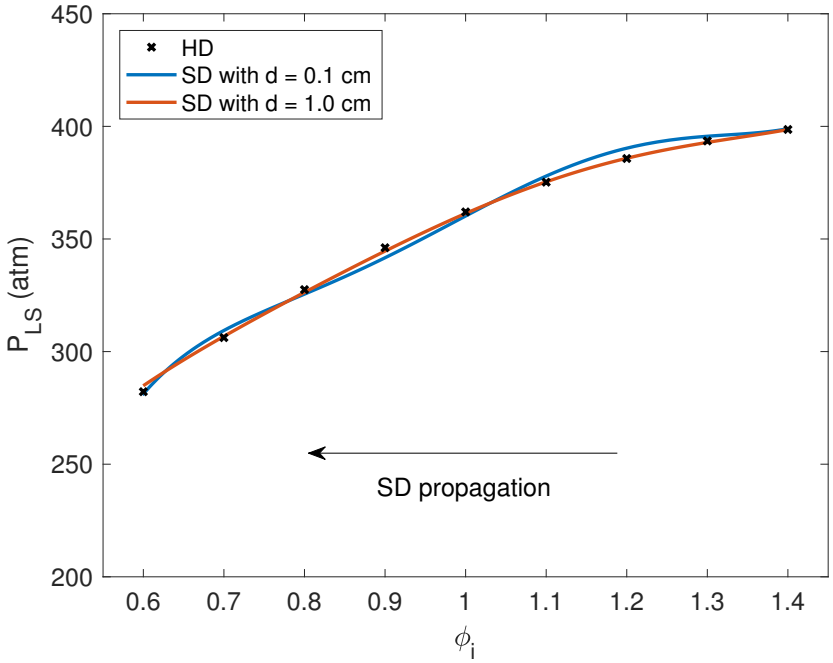

Figure 4.10: Computed leading shock pressures of C_3H_8/air HD and SD with $d_s = 0.1$ and 1.0 cm. SD propagates from $\phi_2 = 1.4$ (rich) to $\phi_1 = 0.6$ (lean).

Table 4.2: Acoustic properties of H_2 and C_3H_8 stratification layers.

Fuel	Stratification ($\phi_1 \rightarrow \phi_2$)	I_1 (Pa·s/m)	I_2 (Pa·s/m)	z	c_R	c_T
H_2	$0.6 \rightarrow 1.4$	985.7	887.7	0.90	-0.052	0.948
	$1.4 \rightarrow 0.6$	887.7	985.7	1.11	0.052	1.052
C_3H_8	$0.6 \rightarrow 1.4$	8028	7969	0.99	-0.004	0.996
	$1.4 \rightarrow 0.6$	7969	8028	1.01	0.004	1.004

simple model. Typical acoustics textbooks such as Kinsler et al. (2000) introduce a simple wave reflection and transmission model in the interface between two different media, assuming chemically frozen and linear response. According to the model, the specific acoustic impedance of medium j, I_j, is defined as

$$I_j = \rho_j a_j, \tag{4.1}$$

where subscript j denotes properties of medium j. When the wave propagates from medium 1 to medium 2, the pressure reflection coefficient, c_R, and the pressure transmission coefficient, c_T, are

$$c_R \equiv \frac{P'_R}{P'_I} = \frac{z-1}{z+1}, \tag{4.2}$$

$$c_T \equiv \frac{P'_T}{P'_I} = \frac{2z}{z+1}, \tag{4.3}$$

where P'_I, P'_R, and P'_T are acoustic pressures of incident, reflected, and transmitted waves respectively, and $z = I_2/I_1$ is the ratio of the specific acoustic impedances of two media. Note that the sum of P'_I and P'_R equals to P'_T by the pressure conservation in the interface. The detailed derivations of Equations 4.2 and 4.3 can be found in Appendix B. The calculated values of I, z, c_R, and c_T for several lean-to-rich and rich-to-lean cases are in Table 4.2.

Acoustic impedances of both hydrogen/air and propane/air are decreased as the mixtures become richer. The density of rich hydrogen/air mixture is smaller than that of lean mixture, while the difference in sound speeds is comparably small. In the propane/air cases, if the mixture becomes richer, the density increases slightly but the sound speed decreases more. Thus, when the wave propagates from lean mixture to rich mixture, the specific acoustic impedance between the interface decreases as shown in Table 4.2. The acoustic impedance difference between lean and rich mixtures of hydrogen/air case is larger than that of propane/air case. Therefore, the effect of shock reflection is distinct in hydrogen/air SD, while propane/air SD is barely affected by the acoustic impedance difference.

In the hydrogen/air lean-to-rich stratified detonation cases, the specific acoustic impedance difference induces a negative shock reflection and a weakened shock transmission at the interface. The amplitude of transmitted shock wave in the lean-to-rich propagation is lower than that of incident shock. The weakened leading shock induces lower temperature in the

induction zone and longer induction length, thus the reaction propagation is decelerated. The decelerated reaction propagation induces a deficit in the detonation propagation speed in the stratification layer. For rich-to-lean propagation cases, an opposite trend is estimated. Due to the positive shock reflection, an increased shock transmission is predicted from the simple model. The model can explain deficits and surpluses of hydrogen/air cases (Figures 4.3 – 4.6).

In Figure 4.11, the trend of shock reflections in lean-to-rich (top) and rich-to-lean (bottom) stratified hydrogen/air detonations are presented. Note that the cases shown in the figure have different lean and rich equivalence ratios from hydrogen/air cases shown in previous section to show the negative and positive reflections clearly. Figure 4.11 shows the profiles of leading shocks before and after the stratification layer from the ASURF-Parallel calculation. The positions of the leading shock are aligned to the same location for comparison. The lean-to-rich case shows a negative shock reflection and decreased transmitted shock wave, while the rich-to-lean case shows a positive reflection and increased transmission. These trends were similar to the estimation from the simple wave reflection and transmission model.

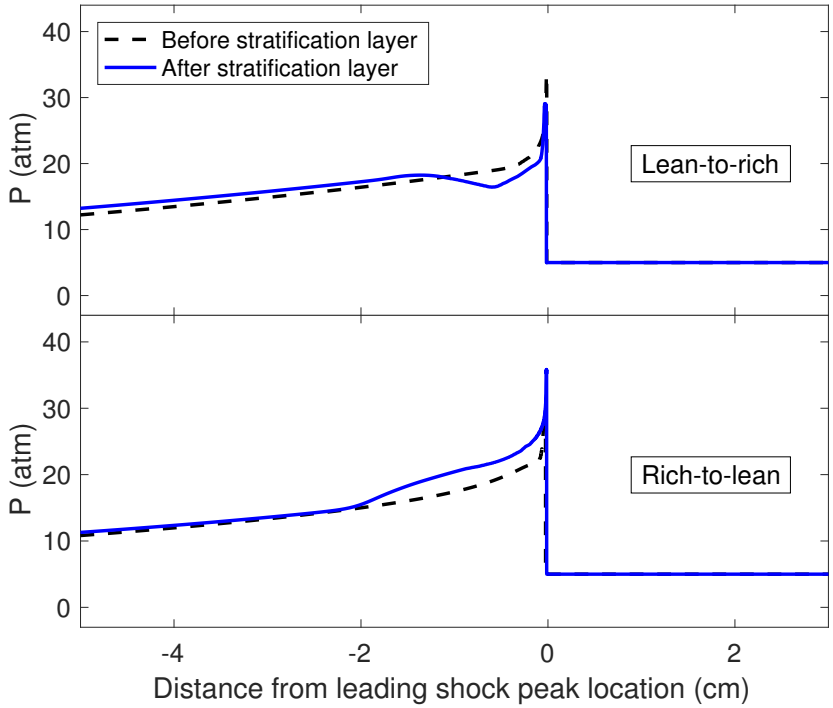

Figure 4.11: Computed pressure profiles of hydrogen/air SD propagation. SD propagates from $\phi_1 = 0.5$ to $\phi_2 = 5.0$ (top) and from $\phi_1 = 5.0$ to $\phi_2 = 0.5$ (bottom).

For a larger size of stratification layer, the model can be modified with multiple interfaces with multiple fluid media instead of one interface with two media. A long stratification layer

can be considered as a series of many interfaces with smaller specific acoustic impedance differences. Thus, the amount of reflection is small at each interface due to the small gradient of adjacent media, but multiple reflections occur for a relatively long period. The reflection effect of larger size of stratification layer is small, as the time scale of the adjustment to HD is not sufficiently larger than the period of multiple reflections.

Effect of detonation structure

The ZND structure further explains deficits or surpluses of stratified detonation speeds compared to those of corresponding homogeneous detonation waves. In the ZND structure, the leading shock is ahead of the reaction front by the induction length. Thus, unlike homogeneous detonation, the LS and RF experience different equivalence ratios in stratified detonations. For a lean-to-rich stratification, the mixture at LS front is richer than that at RF. Therefore, the RF propagation speed is slower than that of the corresponding homogeneous detonation, and this process induces longer induction length.

In Figure 4.12, the pressure, temperature, and heat release rate profiles of hydrogen/air SD and HD at $\phi_i = 1.0$ from the ASURF-Parallel calculations are shown, when SD propagates in the 0.1 cm stratification layer from $\phi_1 = 0.6$ to $\phi_2 = 1.4$. The position at 0 cm represents the leading shock location, so the positive location represents unburnt and unshocked mixture, while the negative locations are shocked mixture. The leading shock is ahead of reaction front for both homogeneous and stratified detonations as shown in Figure 4.12. The heat release rate of SD was delayed and decreased from the that of homogeneous detonation, because the mixture at the reaction front of SD was slightly lean, while the mixture at the leading shock front was slightly rich. The mixture distribution in SD induces longer induction length, and the temperature profiles clearly shows that the induction zone of SD is much larger than that of HD.

In rich-to-lean propagation, the mixture at the reaction front of SD was rich. Thus, the heat release rate of SD was larger than that of HD. The size of induction zone also became smaller, so the reaction propagation speed was accelerated. Figure 4.13 shows the pressure, temperature, and heat release rate profiles of hydrogen/air SD and HD at $\phi_i = 1.0$. The SD propagates in the 0.1 cm stratification layer from $\phi_1 = 1.4$ to $\phi_2 = 0.6$. The trend was opposite from the lean-to-rich case. The induction zone was shorten, and the heat release rate increased, compared to the homogeneous detonation structure. However, these changes were significantly small compared to the lean-to-rich case, even though the sizes of stratification layer were the same.

The distribution of hydrogen/air HD shock pressures over equivalence ratio was shown in Figures 4.4 and 4.6. Overall, the leading shock pressure of HD increases as the mixture is richer. However, in the lean side, the slope of the LS pressure increment is stiff, while the slope is gradual in the richer side. The SD waves tend to be adjusted to the local corresponding HD to become a stable state. If the size of stratification layer is sufficiently

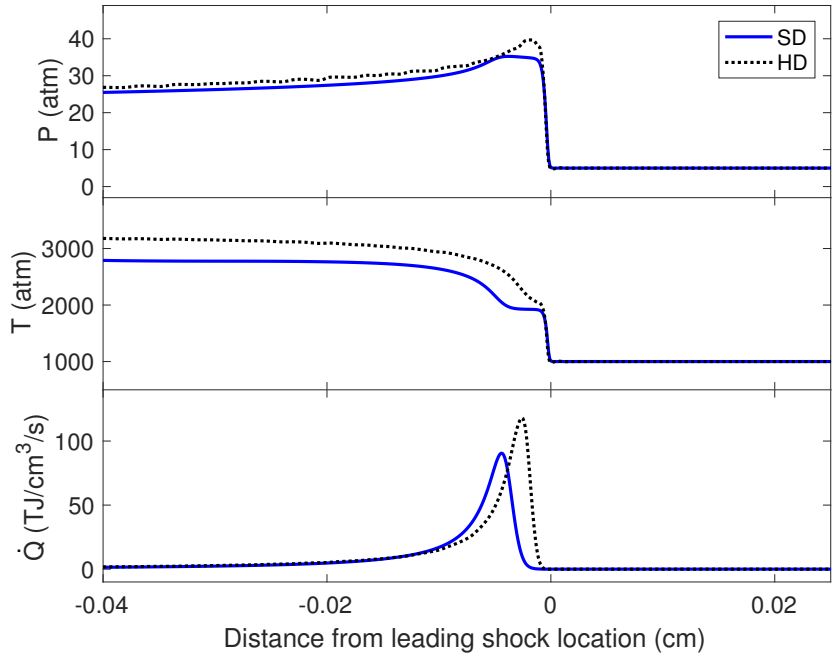

Figure 4.12: Pressure, temperature, and heat release rate profiles of hydrogen/air SD and HD at $\phi_i = 1.0$, when SD propagates from $\phi_1 = 0.6$ to $\phi_2 = 1.4$ ($d_s = 0.1$ cm).

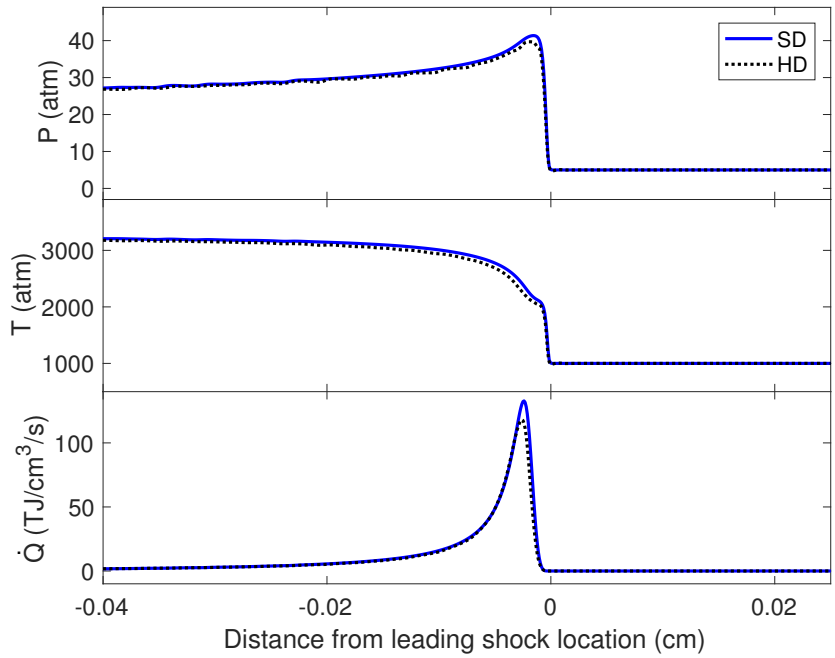

Figure 4.13: Pressure, temperature, and heat release rate profiles of hydrogen/air SD and HD at $\phi_i = 1.0$, when SD propagates from $\phi_1 = 1.4$ to $\phi_2 = 0.6$ ($d_s = 0.1$ cm).

long, the stratified detonation will follow the local CJ properties in the stratification layer. In the lean-to-rich cases, the stratified detonation propagates from the lean side, where the HD leading shock pressure increases rapidly. Thus, the time scale of adjustment to HD is relatively long, and the effect of stratification is considerable. On the other hand, the rich-to-lean SD propagates from the richer side. Since the HD leading shock pressure does not change much in the beginning of the stratified layer, the time scale of adjustment to HD is very short. Therefore, the stratified detonation behaves like a series of HDs in the richer side of the stratification layer.

Effect of fuel

The propane/air detonation showed different trends from the hydrogen/air cases. All cases except the lean-to-rich SD in 0.1 cm stratification layer also can be explained by the shock reflection and detonation structure effects. The acoustic impedance difference of lean and rich propane/air mixtures is very small, so the effect of shock reflection is negligible. The typical induction length of propane/air detonation is much shorter than that of hydrogen/air detonation in this work, which implies that the difference in mixtures at RF and LS front in the propane/air SD is small compared to the that of hydrogen/air SD. Thus, the effect of detonation structure is less in the propane/air SD than in the hydrogen/air SD. Since both the shock reflection and detonation structure effects are less, the propane/air SD detonation tends to follow the corresponding local homogeneous detonation properties as shown in Figures 4.7 – 4.10 except the case of lean-to-rich SD with 0.1 cm stratification layer.

In the case of lean-to-rich SD with 0.1 cm stratification layer, the leading shock pressure showed a different behavior compared to other cases. This behavior is due to the competition of leading shock front speed, S_{LS}, and reaction front propagation speed, S_{RF}. Initially, the the induction length, l_{ind}, became longer than that of HD by the detonation structure effect. As discussed earlier, longer induction length induces a deceleration of S_{RF}. However, S_{LS} is also decelerated by the longer l_{ind}. The LS is generally supported by the reaction front propagation. If the distance between the LS and RF becomes larger, the RF cannot support the LS. Thus, S_{LS} is decelerated, and P_{LS} is weakened. When the deceleration of S_{RF} is larger than that of S_{LS}, the induction length grows longer. Then, the detonation propagation is slower and the leading shock pressure is lower than those of HD. On the other hand, when the deceleration of S_{LS} is larger, the length of induction zone becomes shorter, so the faster detonation propagation and higher P_{LS} will be observed.

Figure 4.14 shows S_{RF}, S_{LS}, and l_{ind} in the 0.1 cm stratification layer for propane/air lean-to-rich SD. Note that the induction lengths in this figure were calculated based on the distance between the locations of LS and RF. Initially, the LS and RF propagated at the same speed. The induction length increased due to the detonation structure effect, so both S_{RF} and S_{LS} were slower than the corresponding homogeneous detonation. As the deceleration of S_{LS} was larger, the induction length started to decreased until $\phi_i \sim 1.1$. As the induction length at $\phi_i \sim 1.1$ was smaller than that of corresponding HD, the detonation

propagation speed was faster and the leading shock pressure was higher than the properties of HD at this location as shown in Figures 4.7 and 4.8. Then, the length of induction zone oscillated due to the competition of S_{RF} and S_{LS}, and so did P_{LS}.

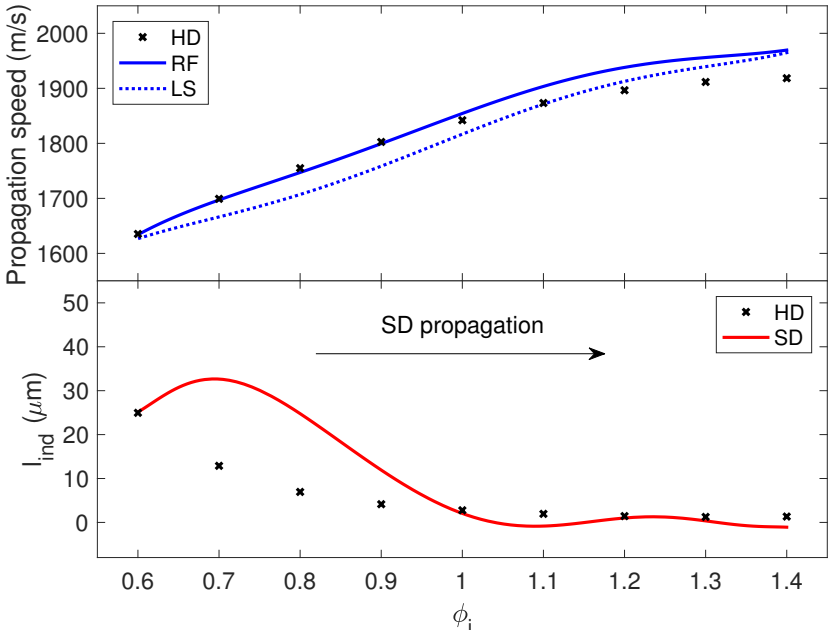

Figure 4.14: S_{RF}, S_{LS}, and l_{ind} in 0.1 cm stratification layer for propane/air lean-to-rich SD propagation from $\phi_1 = 0.6$ to $\phi_2 = 1.4$.

Overall mechanisms of stratified detonation

From the results and discussion, the overall mechanisms of lean-to-rich and rich-to-lean stratified detonations are modeled as in Figure 4.15.

For hydrogen/air lean-to-rich SD, both shock reflection and detonation structure effects decreased the leading shock pressure and VN temperature. The induction length became longer, and S_{RF} deceleration was larger than that of LS speed, so slower detonation propagation speed and lower leading shock pressure were observed as described in Figure 4.15a. When the length of stratification layer is longer, both shock reflection and detonation structure effects were less, the deficits were also less. The mechanism of hydrogen/air rich-to-lean SD cases were similar but opposite as in Figure 4.15b.

Cases of propane/air lean-to-rich SD also followed Figure 4.15a. However the effect of shock reflection was negligible, and the structure effect was small compared to the effects of hydrogen/air SD. For a large stratification layer ($d_s = 1$ cm), effects were small, but the trend was similar to the hydrogen/air cases. However, for the 0.1 cm stratification layer, the structure effect was large, and the competition of S_{RF} and S_{LS} were observed. The

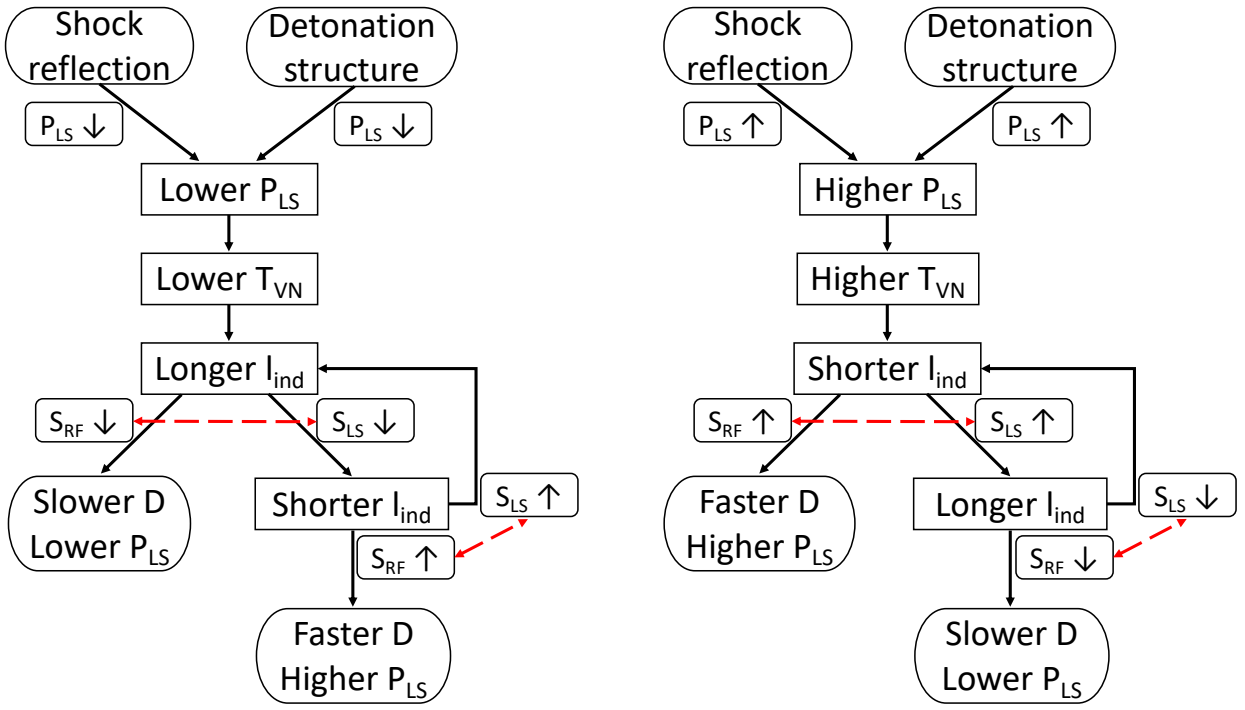

(a) Lean-to-rich (b) Rich-to-lean

Figure 4.15: Mechanisms of stratified detonation propagation compared to corresponding homogeneous detonations

leading shock pressure overshot and oscillated, and the process can be described by the loop in Figure 4.15a.

Propane/air rich-to-lean SD cases generally showed negligible effects of stratification. For a small stratification layer ($d_s = 0.1$ cm), a small structure effect was observed. As in Figure 4.15b, the LS pressure was initially slightly higher than the corresponding HD. Then, the shortened induction length provoked acceleration of S_{LS}, and the accelerated S_{LS} extended the induction length. Thus, slightly slower detonation propagation speed and lower LS pressure were observed in the lean side.

4.5 Conclusions

Numerical simulations were performed on hydrogen/air and propane/air stratified detonations in the one-dimensional planar coordinate using ASURF-Parallel. The properties of stratified detonation at each location in the stratification layer were calculated and compared with those of homogeneous detonation of the local equivalence ratio. Lean-to-rich and rich-to-lean propagation cases with different sizes of stratification layer were considered. A model for an acoustic wave propagating through the interface of two different fluid media

and the ZND detonation structure model were employed to explain the behavior of stratified detonation. The following conclusions were deduced from the simulation results and analysis:

- Generally, the lean-to-rich stratified detonation had deficits in detonation propagation speed and leading shock pressure compared to the corresponding homogeneous detonation. On the other hand, the rich-to-lean stratified detonation showed surpluses in both detonation propagation speed and leading shock pressure. These trends were distinct for hydrogen/air detonation cases. The effect of fuel-stratification was larger for smaller stratification layer size due to the higher gradient of the stratification.

- A wave reflection and transmission model was employed to investigate the effect of shock reflection. In the model, the specific acoustic impedance difference between the interface was the main factor to create the shock reflection. The amounts of shock reflection and transmission were calculated using the model. Negative shock reflection and decreased transmission were found in the lean-to-rich propagation, while positive shock reflection and increased transmission were found in the rich-to-lean propagation. The estimation from the simple model corresponded to the ASURF-Parallel simulation result qualitatively.

- The ZND structure model was utilized to further explain deficits or surpluses of stratified detonation properties. In a ZND detonation, the leading shock is ahead of the reaction front. Thus, the leading shock and reaction front are affected differently by the fuel-stratification. For lean-to-rich propagation, as the mixture at the reaction front is leaner than the mixture at the leading shock front, the induction zone becomes longer and the reaction front propagation speed is decelerated. The rich-to-lean stratified detonation showed the opposite trend. The structure effect was confirmed with the transient simulation results.

- The increment of HD leading shock pressure with equivalence ratio is stiff in the lean side, while it is gradual in the rich side. The lean-to-rich stratified detonation propagates from the lean side where the time scale of adjustment to the homogeneous detonation is considerably long, so the stratification effect was clearly observed. For rich-to-lean stratified detonation, the stratification effect was less due to a short time scale of adjustment to the homogeneous detonation in the rich side.

- Propane/air stratified detonation has shorter induction length and smaller difference in acoustic impedances, compared to the hydrogen/air SD. Thus, the effects of detonation structure and shock reflection are limited. The SD tends to follow the corresponding homogeneous detonations. However, due to the competition between the leading shock speed and reaction front propagation speed, the induction length and the leading shock pressure may oscillate.

- The overall mechanisms of lean-to-rich and rich-to-lean stratified detonations were proposed. The schematics explain the effects of shock reflection and detonation structure, and the behavior of leading shock pressure, induction length, and the detonation propagation speed. The competition of leading shock speed and reaction front propagation speed is also included.

The models and analysis presented in this study can be applied to other stratified detonation problems with different fuels and conditions. A different trend is expected for a heavy fuel, as the specific acoustic impedance of fuel/air mixture may increase when the mixture becomes richer.

Chapter 5

Detonation Suppression

This chapter is based on the manuscript submitted for publication (Ryu et al., 2018a). The study is a numerical investigation of detonation propagation modes in water vapor concentration gradients.

5.1 Introduction

Prevention and suppression of potential detonations are extremely important, as detonations with violent pressure waves frequently cause catastrophic human casualties and property damages. The fundamental process of detonation suppression has been studied actively (Dorofeev, 2011). Several methods have been proposed to suppress detonations, and one of the effective suppression methods is using water sprays (Thomas et al., 1990; Parra et al., 2004; Ye et al., 2005). Thomas et al. (1990) experimentally investigated detonation quenching by measuring pressure in a vertical tube fitted with various spray generators which inject water at the top of the tube during detonation propagation. With a proper water spray, detonation quenching was observed. The spray droplet size and loading densities were suggested as the key parameters governing the extinction of detonation wave. A field-scale pipe experiment was done by Ye et al. (2005). Water mist was used to suppress detonation, and suppression effect of water mist was successfully proved in a field-scale pipe of methane/air mixture. They found that the detonation suppression depended on the density and the size of water mist suspended inside the pipe. Parra et al. (2004) performed numerical simulations on extinction of detonation wave with a water mist. They focused on droplet break-up effect of the introduced water content, and confirmed detonation quenching.

As the addition of water introduces inhomogeneity to the fuel/air mixtures, many researchers have investigated the detonation suppression process through a composition-varying layer of unburnt mixtures, both experimentally and numerically. An experimental research with C_2H_2/O_2 mixture was performed by Thomas et al. (1991) to study detonation propagation along concentration gradients of several dilution gases, and they found that the

properties of transmitted detonation were rapidly adjusted to values appropriate to the local gas mixture. They also observed secondary pressure peaks due to an explosion of the shocked but unreacted gas after the decoupling of the incident shock and reaction front. Kessler et al. (2012) and Ettner et al. (2013) numerically simulated detonation propagations along equivalence ratio gradients, and explained the effects of the gradient on the cell size of CH_4/air detonation and the Mach reflection of H_2/O_2 detonation, respectively. Later, the influences of H_2 concentration gradients on detonation propagation were experimentally investigated. Boeck et al. (2016) observed velocity deficits of detonation propagation in H_2/air mixture by H_2 concentration gradients, and Grune et al. (2017) investigated the critical conditions for detonation propagations in both H_2/air and H_2/O_2 mixtures with H_2 concentration gradients. Similar studies have been performed for the propagation of detonations through inert gases (Gavrilenko et al., 1982; Teodorczyk and Benoan, 1996). Experimental studies of the inert gas effect on detonation propagations showed similar behaviors with concentration gradient studies. The influence of acoustic impedance of an inert gas was also simulated recently (Houim and Fievisohn, 2017).

However, the above-mentioned studies on detonation suppression mainly correlated the final states of the detonation propagation with the initial mixture conditions, and did not investigate the detailed transient states during the suppression process. The behaviors of detonation waves propagating into a H_2O-diluted mixture can be better understood by taking a closer look at the transient process. Therefore, in this paper, the numerical investigation focuses on the transient process of established detonations propagating through vapor gradient layers. Specifically, following questions are to be answered:

- How does an established Chapman-Jouguet (CJ) detonation respond when passing through a H_2O gradient layer?
- What are the detailed mechanisms of various combustion modes resulting from the gradient layers?
- Can these combustion modes be classified by some parameters? If so, what kind of information is needed for such classification?

To answer these questions, detonation simulations of stoichiometric 50%H_2-50%CO/air mixtures with H_2O gradient layers were performed. The theory of shock transmission and reflection in a density-varying medium was introduced to elaborate the decoupling process of leading shock and reaction front, i.e., detonation suppression. Two dimensionless parameters based on the initial conditions were proposed to determine possible combustion modes, while a transient parameter was proposed to predict the detonation re-initiation after the mitigation of the initial detonation.

5.2 Numerical simulation setup

Figure 5.1 shows the schematic setup of this numerical study. An one-dimensional planar domain was used as this is the simplest model to consider. A fully developed CJ detonation was initialized near the left end of the domain and propagating to the right. The left end has a wall (reflective) boundary condition to sustain the detonation wave, and the right end has a transmissive boundary condition to attenuate reflected pressure waves. H_2O was added in the unburnt mixture upstream of the detonation wave. The location at $x = 0$ is marked as the start of H_2O-containing region of unburnt mixture. From $x = 0$ to d cm, the concentration of H_2O linearly increases to a certain mole fraction X_{H_2O}. This region is referred to as the gradient layer. On the right side of the gradient layer, the mole fraction of H_2O is uniform throughout the domain when $x \geq d$. The CJ detonation front was placed at x = -0.02 cm to minimize the effect of the unintended H_2O mass diffusion before the arrival of the incident CJ detonation.

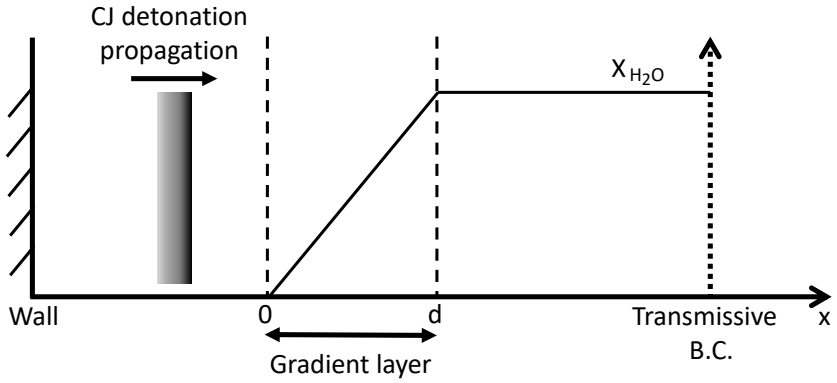

Figure 5.1: Schematic setup of detonation propagation through a H_2O gradient layer in 1-D planar domain.

Transient detonation simulations were carried out using ASURF-Parallel (Chen, 2009; Shi, 2017). For steady-state ZND detonation calculations, the Shock and Detonation Toolbox (Browne et al., 2004; Kao and Shepherd, 2004) was used. For ignition delay calculations, SENKIN (Lutz et al., 1988) was used.

A stoichiometric 50%H_2-50%CO/air mixture at initial temperature, T, of 1200 K and pressure, P, of 30 atm was simulated. H_2-CO syngas was chosen as the fuel due to its relatively well-understood chemical kinetics. An 11-species skeletal chemical kinetic model (Hawkes et al., 2007) was used in the current study. When H_2O was added, the mixture temperature and pressure remained the same. The whole domain length of the simulation is 10 cm. The minimum grid size is 6.25×10^{-7} m, and the time step is 6.25×10^{-11} s. An example of the simulation initial state is shown in Figure 5.2. Note that H_2O is one of the product species of the CJ detonation, so there should have values of X_{H_2O} in the region x<0,

corresponding to H_2O in the burnt gas. However, they are omitted for clarity in Figure 5.2 as the plot only intends to show the H_2O dilution on the unburnt mixture side.

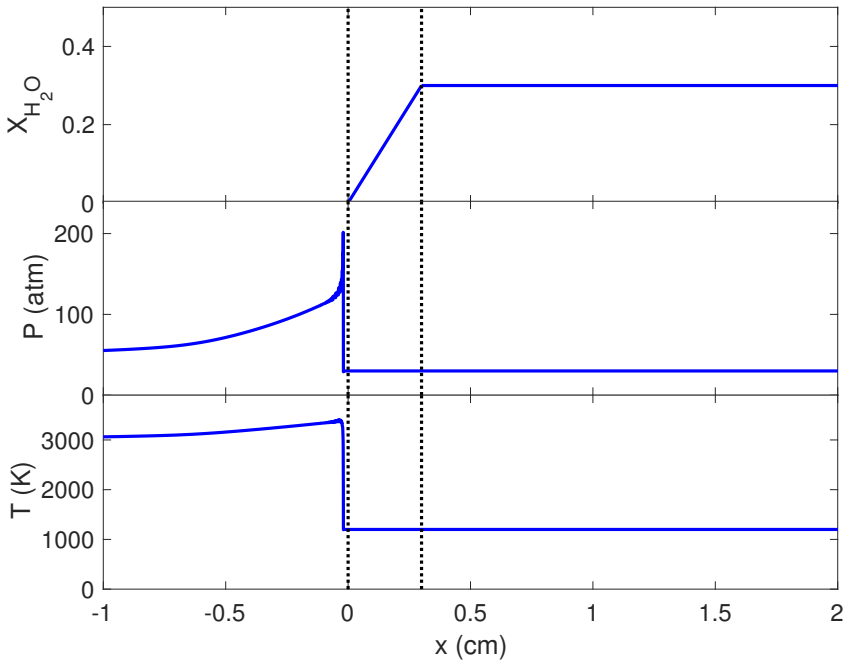

Figure 5.2: An example of H_2O mole fraction in unburnt side, pressure, and temperature profiles at the simulation initial state.

Multiple numerical simulations were performed, in which the amount of H_2O on the unburnt side and the thickness of the gradient layer were varied. Five different mole fractions of H_2O, $X_{H_2O} = 0.1$, 0.2, 0.3, 0.4, and 0.5, were used. The thicknesses of the gradient layer, d, were chosen from 10^{-5} m to 10^{-2} m, while the induction length of the ZND detonation structure is on the order of 10^{-5} m for this particular syngas/air mixture and the imposed thermodynamic conditions.

As this study is conducted in an 1-D planar domain, effects of heat and friction losses through the walls, and three-dimensional effects such as turbulence and stretching are neglected.

5.3 Results and discussion

Chemical effect of water vapor

Before looking at the water vapor gradient, H_2-CO/air reaction with water vapor at the shocked condition was investigated to explain how water vapor contents affect the detonation propagation chemically. The vapor content suppresses the detonation by two mechanisms.

One is by the chemical effect of H_2O molecules, and the other is by reducing the energy density of the unburnt mixture. To separate these two effect, a modified chemical kinetic model was considered by adding inert H_2O molecules. The modified mechanism has one more species, H_2O(i), which has the same thermodynamic and transport properties with H_2O. However, H_2O(i) is chemically frozen and does not react with other species. Instead of adding H_2O to the unburnt mixture side, the same amount of H_2O(i) was added. Comparing two cases with H_2O and H_2O(i) shows the chemical effect of H_2O molecules to the process of detonation suppression.

Figure 5.3 and Figure 5.4 shows the evolutions of the temperature, heat release rate, and H_2O (H_2O + H_2O(i)), O, and OH mole fractions during the reaction in the VN state behind the leading shock computed by the SENKIN for mixtures with $X_{H_2O} = 0.5$ and $X_{H_2O(i)}$= 0.5. In the inert H_2O case, the peak of heat release rate, $\dot{Q}$, was much higher and sharper, so the temperature increased more rapidly than that of the real mechanism. This shows that the water vapor content reduces heat release rate and the reaction speed by its chemical effect.

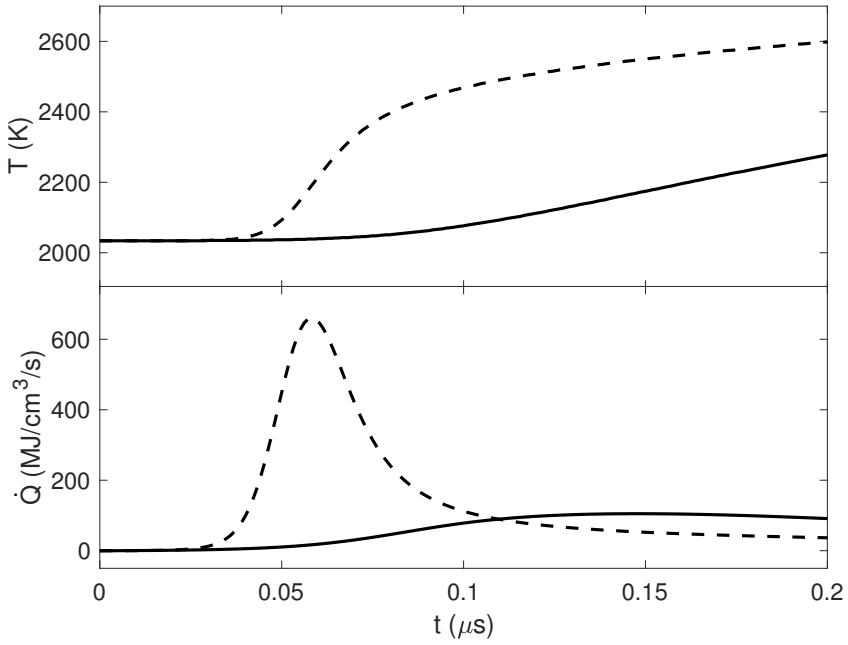

Figure 5.3: Computed temporal evolutions of temperature and pressure during a reaction in VN state of $X_{H_2O} = 0.5$. Solid line: real mechanism, dashed line: mechanism using inert H_2O.

Using the KINALC code (Turányi, 1997), the pathway analysis was performed. During the earlier stage of the reactions (at 2100 K), H_2O species actively reacts with O molecules and produces OH:

$$O + H_2O \rightarrow 2OH. \tag{5.1}$$

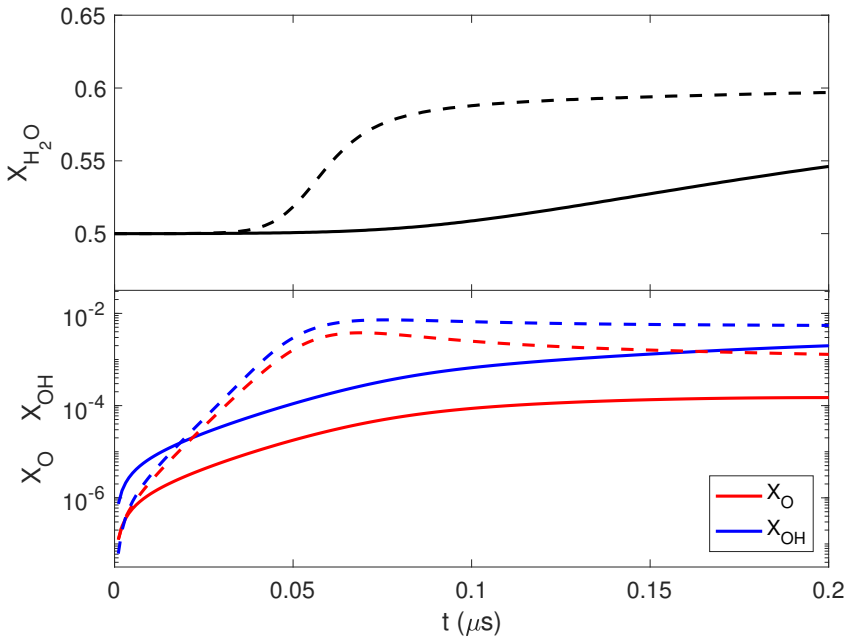

Figure 5.4: Computed temporal evolutions of H_2O (H_2O + H_2O(i)), O, and OH mole fractions during the reaction in VN state of $X_{H_2O} = 0.5$. Solid line: real mechanism, dashed line: mechanism using inert H_2O.

This is an endothermic reaction, and one of the major heat consumption reactions in the earlier stage of the global reaction. In Figure 5.4, the real mechanism shows that OH species are produced much more due to plenty amount of H_2O than in the case of inert H_2O during the earlier stage. Reaction 5.1 consumed O radicals, so the mole fraction of O was smaller than inert H_2O case. Since this reaction is endothermic, the overall heat release rate is decreased and the reaction also becomes slower. The chemical effect of water vapor is found as a factor of the detonation suppression because it increases the gap between the leading shock front and the reaction front.

ZND detonation calculations

CJ and von Neumann (VN) states were first obtained from calculated ZND detonations of stoichiometric 50%H_2-50%CO/air mixtures with and without H_2O using the Shock and Detonation Toolbox. The results are presented in Table 5.1 as a function of X_{H_2O}, which increases from 0 to 0.5 with an increment of 0.1. The corresponding ignition delay times of mixtures at the VN states, τ_{VN}, were also calculated using SENKIN. These results served as references to be compared with the transient A-SURF simulation results. For the incident detonation without H_2O dilution, the initial propagation speed of the detonation front was ~1800 m/s, and the peak pressure was about 202 atm in the A-SURF simulation. In comparison, for the corresponding ZND detonation, the CJ speed, S_{CJ}, was 1799 m/s and

Table 5.1: Calculated CJ speeds, VN states, and ignition delay times at VN states of homogeneous H_2-CO/air/H_2O mixtures using Shock and Detonation Toolbox and SENKIN.

X_{H_2O}	S_{CJ} (m/s)	P_{VN} (atm)	T_{VN} (K)	τ_{VN} (μs)
0.0	1799	204.9	2250	1.752×10^{-2}
0.1	1764	192.6	2147	2.914×10^{-2}
0.2	1729	180.6	2054	5.559×10^{-2}
0.3	1690	168.3	1966	1.259×10^{-1}
0.4	1645	155.0	1880	3.356×10^{-1}
0.5	1589	140.5	1794	1.021

the VN pressure, P_{VN}, was 204.9 atm, which were very close to the values from the A-SURF simulation.

Modes of detonation propagation through the gradient layer

When the incident detonation propagates through the gradient layer, three combustion modes are observed depending on X_{H_2O} and thickness of gradient layer, d: 1) normal detonation propagation, 2) detonation mitigation and re-initiation, and 3) detonation suppression. In this study, detonation mitigation refers to the intermediate state where a detonation is about to transition into a deflagration, while detonation suppression refers to the process where a detonation fully transitions into a deflagration. More quantitative comparisons are provided in the following section.

Temporal snapshots of pressure, temperature, and heat release rate profiles are shown to elaborate different combustion modes. Figure 5.5 presents the first mode: normal detonation propagation. The imposed mole fraction of H_2O on the unburnt mixture side is 0.1 and the thickness of the gradient layer is 0.1 cm. The location of pressure peak is defined as the leading shock (LS), while the location of maximum heat release rate is defined as the reaction front (RF). In an established CJ detonation, LS and RF are very close to each other, either of them can be referred to as the detonation front. In this simulation case, the RF followed closely with LS during the whole time when the detonation passed through the layer, although LS peak pressure was slightly weakened. The peak pressure after the gradient layer was around 193 atm, matching the calculated VN values. For this case, the transient detonation can be treated "quasi-steadily", i.e., described by a series of ZND detonations based on local mixture compositions throughout the gradient layer. A similar phenomenon was observed experimentally by Thomas et al. (1991).

When the amount of H_2O on the unburnt mixture side is increased, it is anticipated that the detonation wave would be suppressed. However, an intermediate combustion mode was observed. Figure 5.6 presents the simulation results of a case with $X_{H_2O} = 0.3$ and $d = 0.1$ cm. When the detonation front first entered the gradient layer at 0.48 μs, denoted by the time sequence 2, the RF followed closely with LS. Between time sequences 2 and 4, the RF trailed

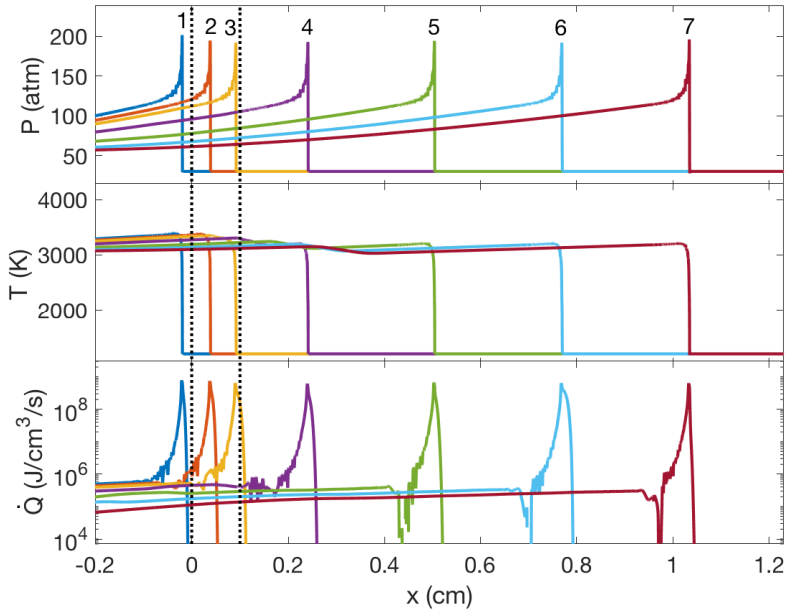

Figure 5.5: Computed profiles of pressure, temperature, and heat release rate for a detonation propagation through 0.1 cm gradient layer with $X_{H_2O} = 0.1$. Time sequence 1: 0.00 μs, 2: 0.33 μs, 3: 0.63 μs, 4: 1.48 μs, 5: 2.98 μs, 6: 4.48 μs, 7: 5.98 μs.

behind the LS, and LS peak pressure was reduced due to the decoupling of the two fronts. The temperature profiles reveal two regions of sharp temperature changes: the right region containing a step increase is caused by the compression from the LS, while the left region of a relatively slow increase represents the heat release from the RF. This indicates that the detonation is mitigated and about to transition into a deflagration. However, starting from time sequence 5, another pressure peak was seen behind the LS. The pressure peak kept growing and eventually caught up with the LS at time sequence 7. The resulting peak pressure was even higher than the VN pressure of the local mixture. In the meantime, the reaction front followed closely with the LS again. This secondary pressure peak after the separation of LS and RF was also observed in the experiments by Thomas et al. (1991). After time sequence 8, the newly generated detonation approached its corresponding CJ and VN states of $X_{H_2O} = 0.3$ mixture. The shock pressure was about 174 atm, which was close to its VN pressure as shown in Table 5.1.

Figure 5.7 presents the results of a simulation case with $X_{H_2O} = 0.5$, and $d = 0.1$ cm. The phenomenon of detonation suppression was observed. Similar to the previous case, the LS started to separate from the RF at 0.48 μs (time sequence 2) and the peak pressure became weaker. After a while, these two wave fronts completely separated. The speed of reaction front propagation approached to the laminar flame speed.

Propagation of LS and RF from all three above cases are compared in Figure 5.8. For

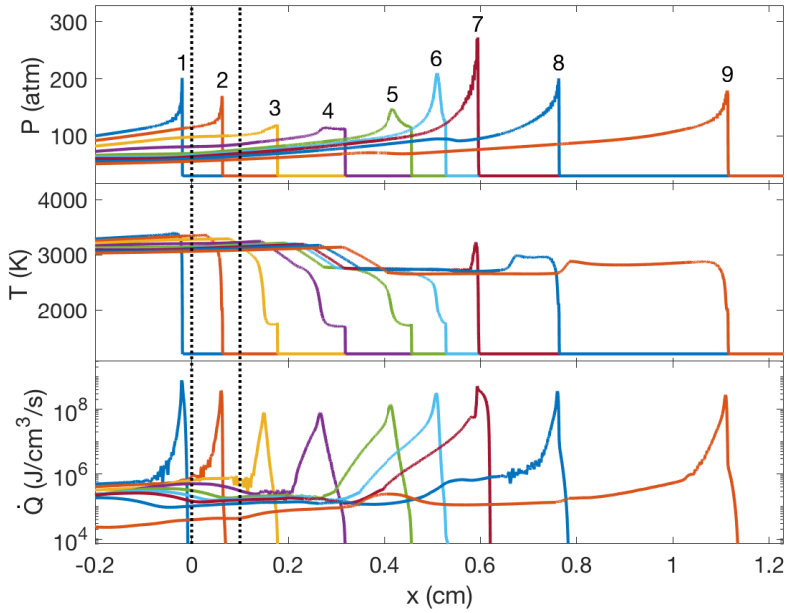

Figure 5.6: Computed profiles of pressure, temperature, and heat release rate for a detonation propagation through 0.1 cm gradient layer with $X_{H_2O} = 0.3$. Time sequence 1: 0.00 μs, 2: 0.48 μs, 3: 1.23 μs, 4: 2.23 μs, 5: 3.23 μs, 6: 3.73 μs, 7: 4.10 μs, 8: 4.98 μs, 9: 6.98 μs.

the case of $X_{H_2O} = 0.1$, the detonation front propagated at ~1760 m/s after the gradient layer, close to the corresponding CJ speed. In the case with $X_{H_2O} = 0.3$, the temporary separation of LS and RF can be clearly seen: the LS and RF propagated at ~1540 m/s and ~1170 m/s, respectively. Eventually, the re-initiated detonation propagated at ~ 700 m/s, close to the CJ speed of $X_{H_2O} = 0.3$ mixture. In the third case, $X_{H_2O} = 0.5$, the detonation was suppressed, as the LS and RF fully separated. The reaction front propagated at ~970 m/s and the leading shock speed was ~1480 m/s after the gradient layer.

Effect of water vapor dilution

As shown in the experimental study by Thomas et al. (1991), when a detonation entered a concentration gradient layer, the LS peak pressure and the detonation propagation speed tended to adjust to the corresponding VN pressure and CJ detonation speed based on local mixture composition and conditions, respectively, as overdriven detonation state is unstable. In this numerical study, a similar trend was observed in the first combustion mode ($X_{H_2O} = 0.1$ and $d = 0.1$ cm), where the detonation can be "quasi-steadily" approximated by local CJ and VN states of the gradient layer. However, large departures from such a "quasi-steady" approximation were found in the other two combustion modes when the amount of H_2O dilution was increased. In these two cases with $X_{H_2O} = 0.3$ and 0.5, the LS peak pressures became lower than the corresponding VN pressures when the detonation passed the gradient

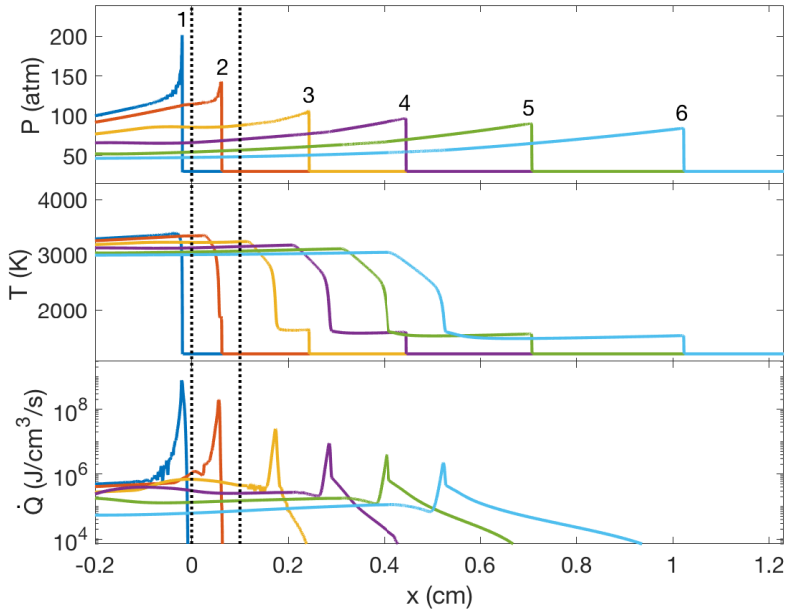

Figure 5.7: Computed profiles of pressure, temperature, and heat release rate for a detonation propagation through 0.1 cm gradient layer with $X_{H_2O} = 0.5$. Time sequence 1: 0.00 μs, 2: 0.48 μs, 3: 1.73 μs, 4: 3.23 μs, 5: 5.23 μs, 6: 7.73 μs.

layer. The weakened LS led to lower post-shock temperature, thus longer ignition delay time of the unreacted mixture. Such a process promoted the separation of LS and RF as the delayed heat release at the RF can no longer support and couple with the LS. Eventually, the LS was fully decoupled from the RF, i.e., the detonation was mitigated and suppressed. Therefore, the key to understand detonation mitigation and suppression is to identify the conditions the leading shock is sufficiently weakened by the gradient layer.

Note that the dilution of H_2O not only reduces the mixture reactivity, but also lowers the total mixture density. According to acoustic theory, when an ideal shock propagates from one medium to another, part of the incident shock is reflected and the rest is transmitted. The properties of transmitted and reflected shocks are determined by the densities and sound speeds of the two media. Compared to mixtures without water vapor, the unburnt mixture with H_2O has a lower density and a higher acoustic speed. When the detonation enters the H_2O-containing region, some portion of the leading shock is reflected and the resulting transmitted shock is thus weakened. Assuming a chemically frozen and linear shock response through an infinitely thin gradient layer, the percentage of the leading shock transmitting into the H_2O-containing region can be estimated using the ratio of specific acoustic impedances across the interface (Kinsler et al., 2000) as introduced in the previous chapter (Equation 4.3).

In the detonation simulations, the mixtures on both sides of the gradient layer are known

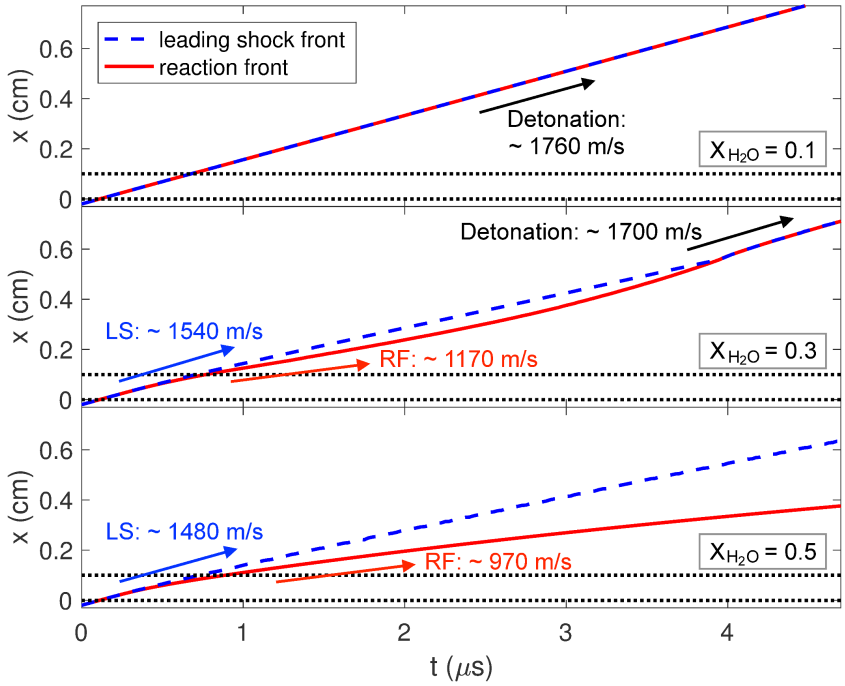

Figure 5.8: Computed temporal locations of leading shock front and reaction front for detonation propagations through 0.1 cm gradient layer with $X_{H_2O} = 0.1$ (top), $X_{H_2O} = 0.3$ (middle), and $X_{H_2O} = 0.5$ (bottom).

thus specific acoustic impedances of two media are readily available; z and c_T can then be calculated. Taking the incident shock pressure, P_I', as the VN pressure of the incident detonation, P_T' can be obtained by multiplying P_I' and c_T. Values of z, c_T, and P_T' are presented for several cases with different levels of X_{H_2O} in Table 5.2. Note that when P_T' in Table 5.2 are lower than P_{VN} in Table 5.1, the transmitted detonation is underdriven compared to the corresponding CJ detonation. Based on P_T' and the corresponding mixture composition, the speed of transmitted shock, S_t, can be calculated using the SD Toolbox. The ratio between S_t and the corresponding CJ detonation speed, S_{CJ}, was calculated and shown in Table 5.2. Moreover, the ignition delay time of the mixture at P_T' state, τ_t, was calculated and compared to the corresponding ignition delay at VN states, τ_{VN}. The ratio between the two ignition delay values is also given in Table 5.2.

Based on the results presented in Table 5.2, the speed of the transmitted shock is very close to the CJ detonation speed, as S_t/S_{CJ} is approximately 1 even at $X_{H_2O} = 0.5$. In comparison, the ignition delay can be greatly increased, e.g., when $X_{H_2O} = 0.5$, the ignition delay under transmitted shock is ~56% longer than the corresponding VN ignition delay. If the shock speed remains the same but the ignition delay time is longer, the reaction front will lag behind the shock, possibly leading to the decoupling of the leading shock and reaction front. Therefore, the chemical effect caused by the transmitted shock is believed dominant

Table 5.2: Estimated properties of transmitted shock to H_2-CO/air/H_2O mixtures from H_2-CO/air mixture.

X_{H_2O}	z	c_T	P'_T (atm)	S_t/S_{CJ}	τ_t/τ_{VN}
0.1	0.98	0.99	190.6	0.99	1.03
0.2	0.96	0.98	176.5	0.99	1.09
0.3	0.95	0.97	162.2	0.98	1.20
0.4	0.93	0.96	146.8	0.97	1.49
0.5	0.91	0.95	130.3	0.96	1.56

in determining the consequent combustion mode after the interface. Therefore, the ratio of τ_t and τ_{VN} may be considered as one parameter to quantify different combustion modes:

$$\zeta = \frac{\tau_t}{\tau_{VN}}. \tag{5.2}$$

Note that the above analysis is solely based on the thermodynamic proprieties of mixtures without any transient simulation result. In order to further explore the effects of ζ, simulations with a thin gradient layer were performed and analyzed. The thickness of the gradient layer is set to 0.001 cm, which is the same order of magnitude as the detonation induction length of the undiluted mixture. Figure 5.9 shows these simulation results of mixtures with different levels of X_{H_2O}. The positions and amplitudes of the leading shocks are plotted. After the detonation passed through the thin layer, the pressure of the transmitted shock became lower than the VN pressures (represented by the dash lines), similar to the estimation in Table 5.2. For $X_{H_2O} = 0.1$, the pressure of transmitted shock was slightly weaker than VN spike pressure after the thin layer. However, the LS pressure reduction did not cause the decoupling of shock and reaction front, so the LS pressure rose and eventually approached the VN pressure of $X_{H_2O} = 0.1$ mixture. For $X_{H_2O} = 0.4$ and 0.5, the reduction in transmitted LS pressure was big enough to cause the separation of the LS and RF. The cases of $X_{H_2O} = 0.2$ and 0.3 show the mode of mitigation followed by re-initiation. With more H_2O dilution, the transmitted shock is more weakened, causing longer ignition delay and eventually detonation suppression.

Effect of gradient layer thickness

For the same H_2O concentration, the concentration gradient can be altered by changing the size of the gradient layer, which also affects the resulting combustion mode. The results shown in Figure 5.10 are simulations with $X_{H_2O} = 0.2$ and different sizes of the gradient layer, $d = 0.001$ cm, 0.01 cm, 0.1 cm, and 1 cm. For the cases of $d = 0.001$ cm and 0.01 cm, the LS pressure rapidly dropped due to shock reflection, and the magnitude was below the VN pressure of the $X_{H_2O} = 0.2$ mixture. The reduced LS pressure resulted in a detonation mitigation and a following re-initiation process. The mechanism of re-initiation will be

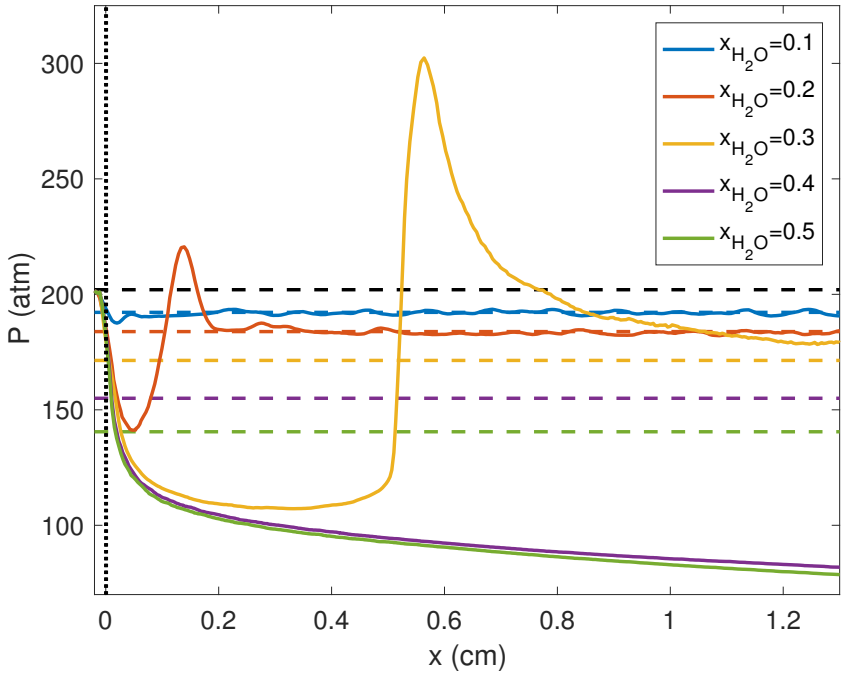

Figure 5.9: Positions and amplitudes of leading shock fronts through thin gradient layers with $X_{H_2O} = 0.1$, 0.2, 0.3, 0.4, and 0.5. Dashed lines are corresponding VN pressures (Black dashed line is P_{VN} without H_2O).

discussed in a latter section. If the size of the layer was increased to 1 cm, the LS pressure dropped gradually and adjusted to the corresponding VN pressure locally.

Since the LS transmission and reflection are seen to be affected by the size of the gradient layer, comparing the gradient layer thickness to the induction length of the CJ detonation, l_{ind}, can be helpful to quantify the LS behaviors. When the RF arrives at the gradient layer, the LS is already inside the layer, ahead of the RF by a distance of the induction length. Figure 5.11 shows schematics of detonation propagation through the gradient layer with different levels of the gradient layer thickness: $d \sim l_{ind}$, and $d \gg l_{ind}$. If the thickness of the gradient layer is about the same order of magnitude as the induction length as shown in 5.11 (a), LS behavior is expected to be like the case of an infinitely thin interface, where the LS strength can be calculated on the basis of specific acoustic impedance change with the maximum X_{H_2O} level. The ignition delay time increases substantially due to the strong LS reflection, and RF tends to separate from LS in this case. Once LS and RF are decoupled, the strength of LS is weakened and the speed of RF is decelerated repeatedly. In the other scenario as shown in Figure 5.11 (b), the thickness of the layer is much larger than the induction length. As the vapor level at the LS is not the maximum X_{H_2O}, the transmitted LS is weakened gradually by reflection. The ignition delay time behind the LS is not increased enough to decelerate the speed of RF, so the LS strength can be supported by the following RF. Therefore, the RF is more likely to keep up with the LS. Based on the above argument,

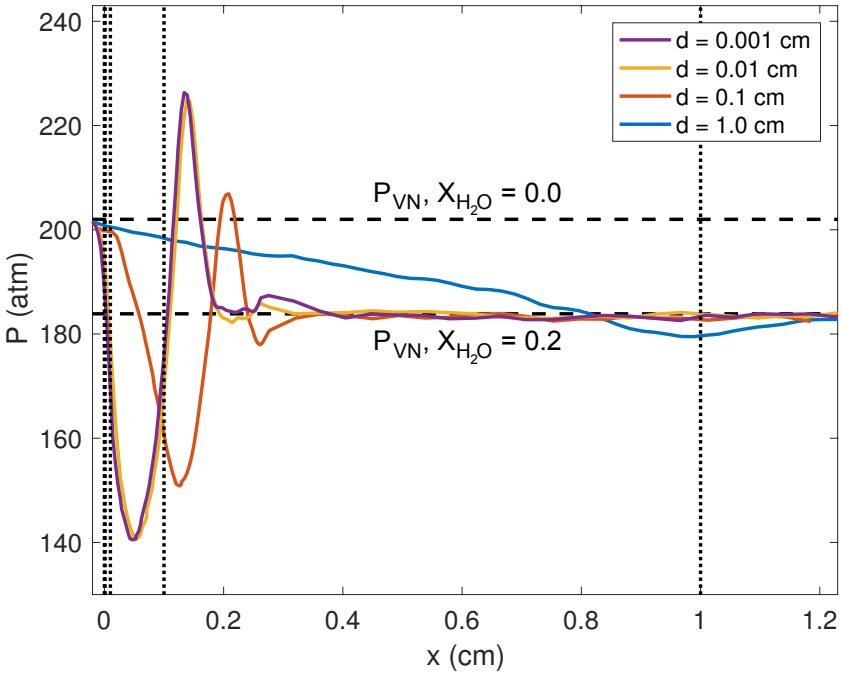

Figure 5.10: Positions and amplitudes of leading shock fronts through gradient layers with $X_{H_2O} = 0.2$ and different layer thicknesses, $d = 0.001$ cm, 0.01 cm, 0.1 cm, and 1 cm. Dashed lines are VN spike pressures of uniform $X_{H_2O} = 0$ and 0.2 mixtures.

the ratio between the gradient layer thickness and the detonation induction length,

$$\eta = \frac{d}{l_{ind}} \tag{5.3}$$

is proposed to describe the gradient of specific acoustic impedance thus identify different combustion modes. Note that l_{ind} in Equation 5.3 is the ZND detonation induction length of the H_2O-containing mixture. When η is large, the effect of LS reflection is modulated to a low level and the detonation propagation approximately follows the local CJ detonation properties. Therefore, the combustion mode tends to be a normal detonation propagation rather than a mitigation or a suppression.

Regime map for detonation propagation modes in vapor concentration gradient

From the results presented above, the specific mode is seen to be influenced by both the normalized ignition delay time including shock reflection effect, ζ, and the ratio of gradient layer thickness to the induction length, η. A regime map was developed by conducting twenty-four cases with various X_{H_2O} and d values. Figure 5.12 presents the results of these simulations with circle markers indicating detonation suppression, triangle markers presenting detonation mitigation and re-initiation, and square markers corresponding to normal

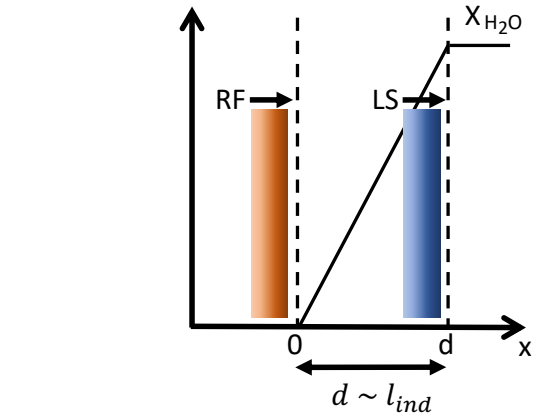

(a) Thinner gradient layer

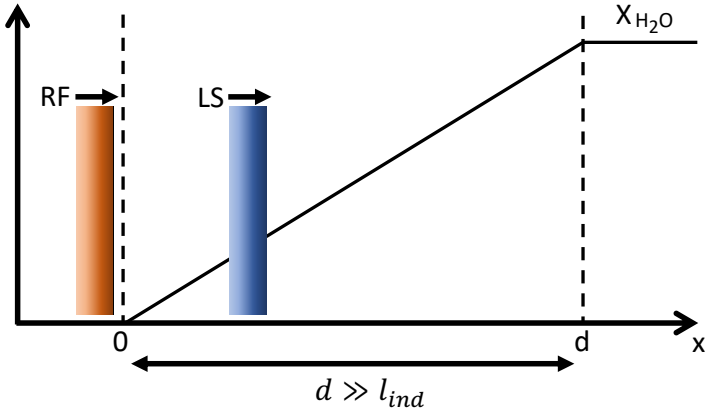

(b) Thicker gradient layer

Figure 5.11: Schematics of leading shock and reaction front passing vapor gradient layers with same amount of water concentration.

detonation propagation using the two non-dimensional factors, ζ and η. The top-left region corresponds to the detonation suppression mode, in which X_{H_2O} is high and LS reflection is able to decouple RF and LS. The middle region is the re-initiation mode, in which the detonation wave becomes mitigated, but another detonation is initiated behind the leading shock. The bottom-right region corresponds to the normal detonation propagation mode, in which the detonation can be "quasi-steadily" approximated by the corresponding local CJ states. The result regime map reveals that both the H_2O concentration and the size of the gradient layer play roles in detonation suppression.

Detonation re-initiation after mitigation

The combustion mode of mitigation and re-initiation were observed between the detonation suppression and the normal detonation propagation modes as shown in the regime map

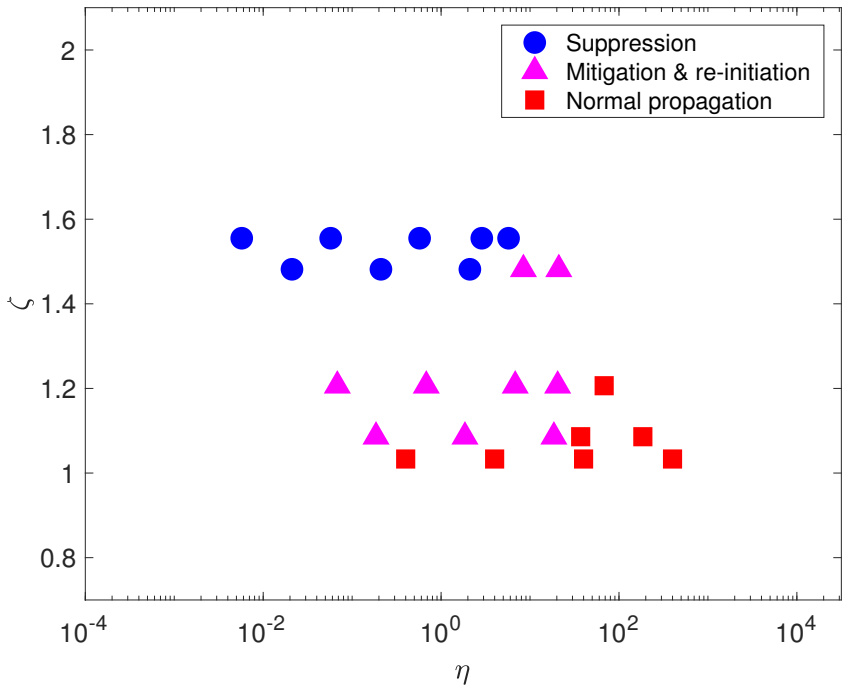

Figure 5.12: Limits of detonation propagation modes through water vapor concentration gradient, in terms of normalized ignition delay time including shock reflection effect, ζ, and ratio of gradient layer thickness to the induction length, η.

(Figure 5.12). The re-initiation process can be understood by considering the reactivity gradient theory (Zel'dovich et al., 1970; Zel'dovich, 1980) and normalized reactivity gradient, ξ (Gu et al., 2003). As discussed in Section 3.2, the transient reactivity gradient can predict the detonation occurrence more precisely (Equation 3.4).

Similarly, this theory can be applied to analyze the current re-initiation process. The region between the LS and the RF may be considered as a hot spot, and the ignition delay times and sound speeds based on the properties between LS and RF can be correlated with the occurrence of the detonation re-initiation. Both τ_i and a in the induction zone depend on temperature, pressure, and X_{H_2O}.

The temporal and spatial profiles of τ_i, u_r, and a for the case of $X_{H_2O} = 0.3$ with $d = 0.1$ cm (Figure 5.6) are shown in Figure 5.13. These variables were calculated using the corresponding local thermodynamic states from the simulation. For each time sequence, only the profiles between LS and RF are shown. The temperature is higher near the RF region, so τ_i is much smaller near the left end of the presented region. Since the relative difference of maximum and minimum acoustic wave velocities is much smaller than those of ignition front propagation velocities, ξ mainly depends on the spatial gradient of autoignition delay times.

If the value of ξ is much larger or smaller than unity, the acoustic wave and the reaction

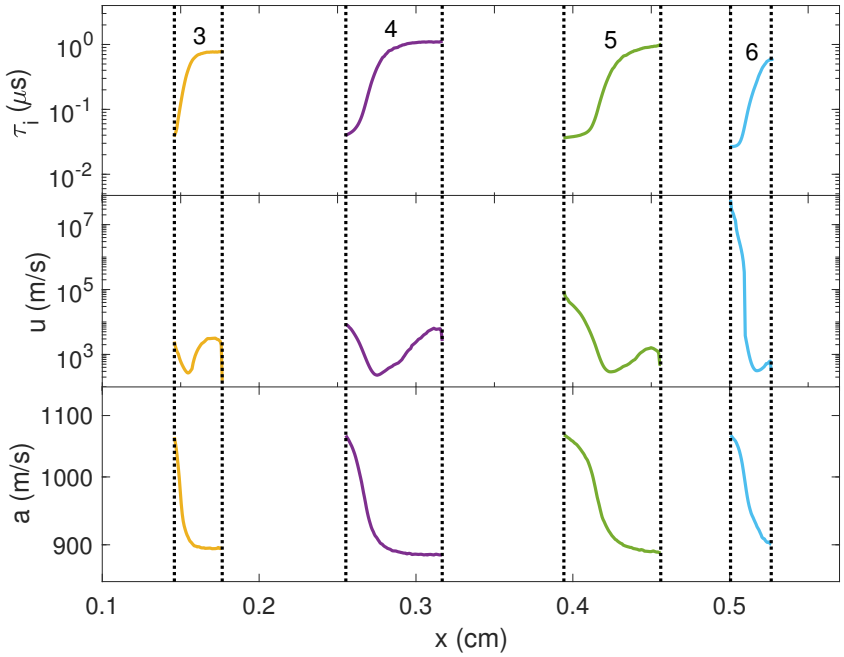

Figure 5.13: Computed profiles of τ_i, u_r, and a between RF and LS for a detonation propagation through 0.1 cm gradient layer with $X_{H_2O} = 0.3$. Time sequence 3: 1.23 μs, 4: 2.23 μs, 5: 3.23 μs, 6: 3.73 μs.

front wave cannot be coupled, then the detonation initiation will not happen. If ξ approaches to unity, a detonation wave is likely to be initiated. For the case of $X_{H_2O} = 0.3$ with $d = 0.1$ cm (Figure 5.6), profiles of pressure, temperature, and ξ over the region between LS and RF are shown in Figure 5.14. At time sequence 3 (1.23 μs), the initial detonation was mitigated, and ξ was on the order of unity so a detonation was expected to develop. The reaction and acoustic waves resonated and formed a new detonation at time sequence 6 (3.73 μs). The average value of ξ between the reaction front and the leading shock front can be used as a indicator of the re-initiation process, and the values were 2.5, 1.5, 1.1, and 1.1 at time sequences 3–6, respectively. As ξ is close to one, there exists a possibility of a new detonation initiation after the mitigation of initial detonation wave.

For the case of $X_{H_2O} = 0.5$ with $d = 0.1$ cm (Figure 5.7), profiles of pressure, temperature, and ξ are presented in Figure 5.15 to illustrate the suppression process without re-initiation. The average values of ξ between RF and LS were 6.8 and 7.0 at time sequences 3 and 4, respectively. As such, the reactivity gradient failed to result in a new detonation initiation.

5.4 Conclusions

Numerical simulations of stoichiometric 50%H_2-50%CO/air mixtures were performed to investigate the combustion modes when a CJ detonation propagates into H_2O-diluted mixture

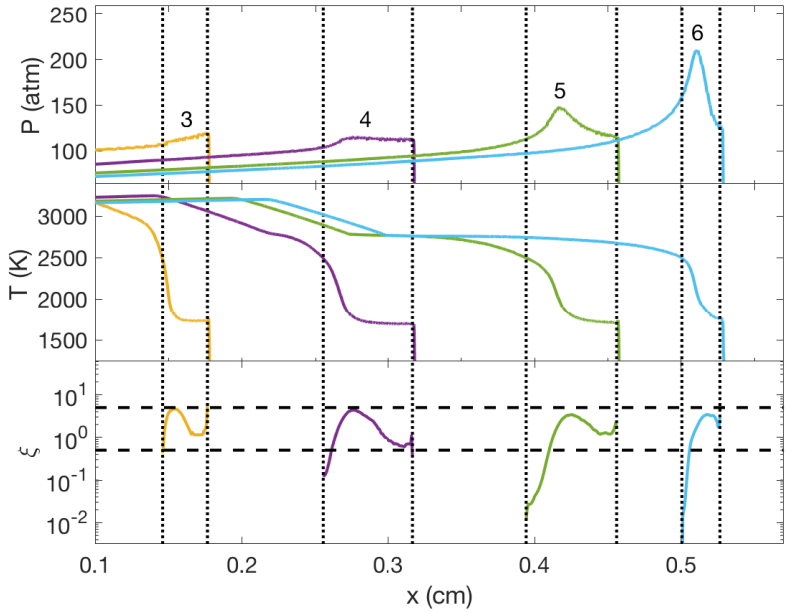

Figure 5.14: Computed profiles of pressure, temperature, and ξ between RF and LS for a detonation propagation through 0.1 cm gradient layer with $X_{H_2O} = 0.3$. Time sequence 3: 1.23 μs, 4: 2.23 μs, 5: 3.23 μs, 6: 3.73 μs. Dashed lines correspond to $\xi = 5$ and 0.5 respectively.

through a composition gradient layer. The following conclusions are drawn:

- Three combustion modes were observed in the numerical simulations: normal detonation propagation, detonation mitigation and re-initiation, and detonation suppression. The H_2O concentration and gradient layer thickness are believed to be the two main factors influencing the modes, and can be expressed using two non-dimensional variables, ζ and η. ζ is the normalized ignition delay time including shock reflection effect, and η is the ratio of the H_2O gradient layer thickness to the induction length of the ZND detonation.

- The shock transmission and reflection across a thin gradient layer were analyzed theoretically using the specific acoustic impedance. The weakening of the transmitted shock due to reflection was observed in transient simulation results. When the thickness of the gradient layer is relatively large compared to the detonation induction length, the impact of LS reflection is reduced thus the RF is able to readjust itself and keep up with the LS, resulting in the normal detonation propagation.

- A regime map for detonation propagation modes through a H_2O concentration gradient was established from numerical calculations for various non-dimensional factors, ζ and

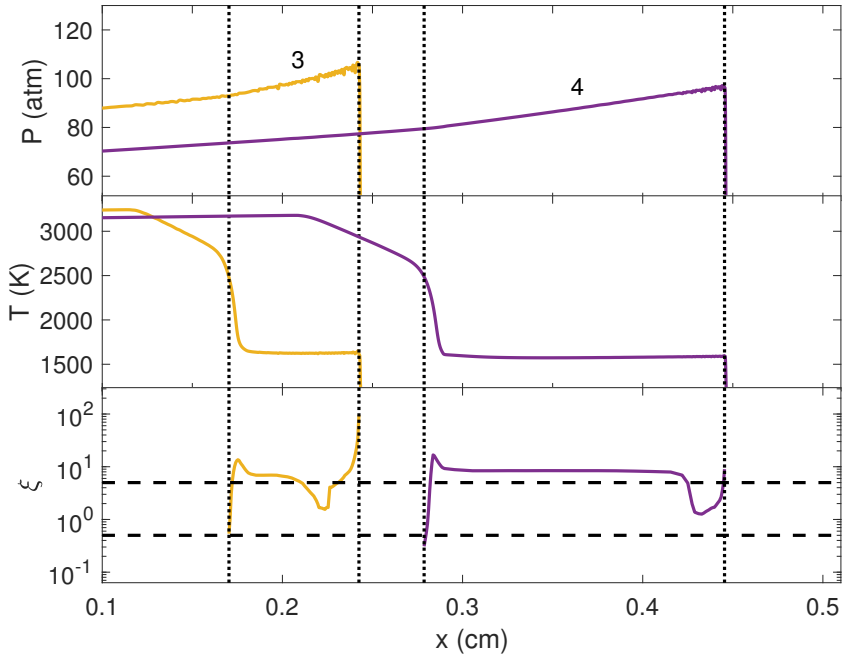

Figure 5.15: Computed profiles of pressure, temperature, and ξ between RF and LS for a detonation propagation through 0.1 cm gradient layer with $X_{H_2O} = 0.5$. Time sequence 3: 1.73 μs, 4: 3.23 μs. Dashed lines correspond to $\xi = 5$ and 0.5 respectively.

η. The incident detonation is more likely to be suppressed with larger ζ and smaller η, representing more reduction in chemical reactivity by the weakening of the LS.

- The ratio of the acoustic wave velocity to the ignition front propagation velocity, ξ, was used as a normalized reactivity gradient for better understanding of a detonation re-initiation behind the mitigated leading shock. Temporal and spatial reactivity gradients were estimated from autoignition delay times using the Zel'dovich theory. If ξ between RF and LS is on the order of unity, a new detonation is expected to develop.

Chapter 6

Concluding Remarks

This chapter summarizes the accomplishments of the presented numerical and theoretical studies. It also provides suggestions for possible future research directions in the field of detonation.

6.1 Summary

Detonation initiation, propagation, and suppression phenomena were studied using various numerical tools and analytic methods. The mechanisms of detonation initiation, propagation, and suppression were proposed and evaluated. In this dissertation, the following conclusions are drawn:

- Multiple numerical tools were employed to study detonation phenomena. The Shock and Detonation Toolbox was used to calculate the ZND structure and CJ properties. SLED were developed to simulate the transient states of detonation as a primary stage. ASURF-Parallel were utilized to perform transient simulations of the detonation phenomena in detail. Using these three numerical tools together seems to be an efficient and reliable way for studies on detonation initiation, propagation, and suppression.
- The Zel'dovich gradient theory is a basic method to predict a detonation initiation. For better prediction, transient reactivity gradient and integral reactivity gradient methods were proposed and evaluated. Without computationally expensive simulations, both methods showed accurate prediction of detonation initiations and DDT with initiation time. Moreover, machine learning techniques were used to develop detonation initiation classification models. The techniques included the logistic regression and CART. Even though the results had limitations due to the small number of data points and gathered independent variables, the models showed a possibility of applying statistical learning techniques into the conventional numerical simulations.

- Detailed numerical simulations were performed to investigate detonation propagation in fuel-stratification layers. The lean-to-rich stratified detonation had deficits in propagation speed and leading shock pressure compared to the corresponding homogeneous detonation, while the rich-to-lean stratified detonation results showed surpluses in both. The shock reflection and transmission model using specific acoustic impedance difference was employed to describe the shock pressure change across the stratification layer. The ZND structure model descried how the mixture distribution in the stratified detonation affected induction length. The effect of fuel was explained by relating properties of fuel to shock reflection and structure models. The overall mechanisms of lean-to-rich and rich-to-lean stratified detonations were proposed, and evaluated with simulation results.

- Modes of detonation wave propagation in water vapor concentration gradients were investigated by the transient numerical simulations with various water vapor concentrations and thicknesses of the gradient layer. From the simulations, three combustion modes were observed: 1) normal detonation propagation, 2) detonation mitigation and re-initiation, 3) detonation suppression. These modes can be well explained by the theory of shock transmission and reflection in a density-varying medium and the reduction in chemical reactivity due to the weakening of the leading shock. A regime map for limits of each mode was established showing that the mode depends on ζ and η, denoting the normalized ignition delay time including shock reflection effect, and the ratio of the gradient layer thickness to the detonation induction length, respectively. A high value of ζ with a low η indicates separation of the leading shock and the reaction front; thus detonation suppression is more probable. In addition, the transient reactivity gradient method was used to understand the detonation re-initiation process after the mitigation of the initial detonation.

6.2 Future work

Even though this dissertation provides tools, models, and analyses to understand detonation initiation, propagation, and suppression, there are still unsolved and challenging problems in the field of detonation. Based on the results of the present work, the following are some recommendations for potential future work to understand detonation phenomena better:

- Due to the stiff chemistry and shock jump in a detonation, better numerical solvers are needed. Current solvers for conservation equations with chemical kinetic models are very reliable and show high fidelity, but computationally expensive. New computational techniques such as the statistical learning can be developed for a compressible reacting flows utilizing existing experiment and numerical result data sets to expedite the simulations.

- Proper chemical kinetic models are not sufficiently valid for detonation simulations. Detonation simulations require chemical kinetic model at high pressure and high temperature. Many models are not correct in this region, especially for heavy fuels. Understanding key reactions for high pressure and temperature condition are needed.

- This work is based on the one-dimensional simulation to understand detonation phenomena without three-dimensional effects. However, in the real phenomena, three-dimensional effects are important. Effects of turbulence, geometry confinement, wall boundary, stretching, shock-shock interaction, and shock-flame interaction are not completely understood yet. Moreover, interactions between these effects are to be studied.

- For initiation, DDT is still not clearly understood. More investigations on DDT are required. For example, one of the possible reason of super-knock in internal engines is a lubricant oil droplet induced DDT. To study this, the model should include phase change of droplet. As typical fuels and lubricant oils include a large number of species, proper reduced chemical kinetic models may be needed.

- For propagation, unsteady detonations are still not fully understood, while the stable (CJ) detonations are relatively well-known. Unsteady detonations are observed when a detonation propagates in inhomogeneous mixtures. Theoretical, numerical, and experimental investigations on strong and weak detonations are needed.

- For suppression, practical techniques to suppress detonation in a very short period is of interest. In this dissertation and previous studies, water vapor or spray was mainly used to suppress the detonation wave. However, if the mechanisms of detonation propagation and suppression are more clear, other methods can be developed.

- Experiments on detonation are extremely difficult. The conditions are not easy to be set, and a physically strong experimental set-up is required to endure high pressure and temperature. The time scale of detonation propagation is very short, so capturing the phenomena is also an issue. Innovative experimental designs should be developed with advanced diagnostic techniques.

- Applications of detonation in energy science and technology are the next step of detonation research. The current understanding including accomplishments of this dissertation is a basis of the detonation applications. Intense endeavors are needed to realize applications of detonation such as rotating detonation engines and optimized controls to avoid super-knocks.

References

Boeck, L.R., Berger, F.M., Hasslberger, J., and Sattelmayer, T., 2016. Detonation propagation in hydrogen–air mixtures with transverse concentration gradients. *Shock Waves*, 26(2), pp.181–192.

Brown, P.N., Byrne, G.D., and Hindmarsh, A.C., 1989. VODE: A variable-coefficient ODE solver. *SIAM Journal on Scientific and Statistical Computing*, 10(5), pp.1038–1051.

Browne, S., Ziegler, J., and Shepherd, J.E., 2004. *Numerical solution methods for shock and detonation jump conditions* (FM2006.006). Pasadena, CA: GALCIT.

Burke, M.P., Chaos, M., Ju, Y., Dryer, F.L., and Klippenstein, S.J., 2012. Comprehensive H2/O2 kinetic model for high-pressure combustion. *International Journal of Chemical Kinetics*, 44(7), pp.444–474.

Bussing, T. and Pappas, G., 1996. Pulse detonation engine theory and concepts. In: S.N.B. Murthy and E.T. Curran, eds. 1996. *Developments in high-speed vehicle propulsion systems, Progress in astronautics and aeronautics*, *Volume 165*. Reston, VA: American Institute of Aeronautics and Astronautics. pp.421–472.

Chapman, D.L., 1899. On the rate of explosion in gases. *Philosophical Magazine Series 5*, 47(284), pp.90–104.

Chen, Y. and Chen, J.Y., 2018. Towards improved automatic chemical kinetic model reduction regarding ignition delays and flame speeds. *Combustion and Flame*, 190, pp.293–301.

Chen, Z., 2009. *Studies on the initiation, propagation, and extinction of premixed flames.* Ph. D. Princeton University.

Chen, Z., Burke, M.P., and Ju, Y., 2009. Effects of Lewis number and ignition energy on the determination of laminar flame speed using propagating spherical flames. *Proceedings of the Combustion Institute*, 32(1), pp.1253–1260.

Dai, P. and Chen, Z., 2015. Supersonic reaction front propagation initiated by a hot spot in n-heptane/air mixture with multistage ignition. *Combustion and Flame*, 162(11), pp.4183–4193.

Dai, P., Chen, Z., Chen, S., and Ju, Y., 2015. Numerical experiments on reaction front propagation in n-heptane/air mixture with temperature gradient. *Proceedings of the Combustion Institute*, 35(3), pp.3045–3052.

Döring, W., 1943. Über den detonationsvorgang in gasen. *Annalen der Physik*, 43, pp.421–436.

Dorofeev, S.B., 2011. Flame acceleration and explosion safety applications. *Proceedings of the Combustion Institute*, 33(2), pp.2161–2175.

Ettner, F., Vollmer, K.G., and Sattelmayer, T., 2013. Mach reflection in detonations propagating through a gas with a concentration gradient. *Shock Waves*, 23(3), pp.201–206.

Fickett, W. and Davis, W.C., 2000. *Detonation: Theory and experiment*. New York, NY: Dover.

Gauntt, R., Kalinich, D., Cardoni, J., Phillips, J., Goldmann, A., Pickering, S., Francis, M., Robb, K., Ott, L., Wang, D., Smith, C., St Germain, S., Schwieder, D., and Phelan, C., 2012. *Fukushima Daiichi accident study* (SAND2012-6173). Albuquerque, NM: Sandia National Laboratories.

Gavrilenko, T.P., Krasnov, A.N., and Nikolaev, Y.A., 1982. Transfer of a gas detonation through an iner gas "plug". *Combustion, Explosion, and Shock Waves*, 18(2), pp.127–131.

Goodwin, D.G., Moffat, H.K., and Speth, R.L., 2017. Cantera: An object-oriented software toolkit for chemical kinetics, thermodynamics, and transport processes (2.3.0). [computer program] Available at: <http://www.cantera.org> [Accessed 6 August 2018].

Grune, J., Sempert, K., Friedrich, A., Kuznetsov, M., and Jordan, T., 2017. Detonation wave propagation in semi-confined layers of hydrogen–air and hydrogen–oxygen mixtures. *International Journal of Hydrogen Energy*, 42(11), pp.7589–7599.

Gu, X.J., Emerson, D.R., and Bradley, D., 2003. Modes of reaction front propagation from hot spots. *Combustion and Flame*, 133(1-2), pp.63–74.

Hawkes, E.R., Sankaran, R., Sutherland, J.C., and Chen, J.H., 2007. Scalar mixing in direct numerical simulations of temporally evolving plane jet flames with skeletal CO/H2 kinetics. *Proceedings of the Combustion Institute*, 31, pp.1633–1640.

Houim, R.W. and Fievisohn, R.T., 2017. The influence of acoustic impedance on gaseous layered detonations bounded by an inert gas. *Combustion and Flame*, 179, pp.185–198.

Hugoniot, H., 1889. Mémoire sur la propagation du mouvement dans les corps et spécialement dans les gaz parfaits. *Journal de l'Ecole Polytechique*, 58, pp.1–125.

International Atomic Energy Agency, 2015. *The Fukushima Daiichi accident* (GC(59)/14). Vienna: International Atomic Energy Agency.

James, G., Witten, D., Hastie, T., and Tibshirani, R., 2013. *An introduction to statistical learning with applications in R*. New York, NY: Springer.

Jeong, K., 2018. New theoretically predicted RDX- and β-HMX-based high-energy-density molecules. *International Journal of Quantum Chemistry*, 118(6), pp.1–7.

Jouguet, É., 1905. Sur la propagation des réactions chimiques dans les gaz. *Journal de mathématiques pures et appliquées*, 6(1), pp.347–425.

Jouguet, É., 1906. Sur la propagation des réactions chimiques dans les gaz. *Journal de mathématiques pures et appliquées*, 6(2), pp.5–86.

Kao, S. and Shepherd, J.E., 2004. *Numerical solution methods for control volume explosions and ZND detonation structure* (FM2006.007). Pasadena, CA: GALCIT.

Kee, R.J., Dixon-Lewis, G., Warnatz, J., Coltrin, M.E., and Miller, J.A., 1986. *A Fortran computer code package for the evaluation of gas-phase, multicomponent transport properties* (SAND86-8246). Livermore, CA: Sandia National Laboratories.

Kee, R.J., Rupley, F.M., Meeks, E., and Miller, J.A., 1996. *Chemkin-III: A Fortran chemical kinetics package for the analysis of gas-phase chemical and plasma kinetics* (SAND96-8216). Livermore, CA: Sandia National Laboratories.

Kessler, D.A., Gamezo, V.N., and Oran, E.S., 2012. Gas-phase detonation propagation in mixture composition gradients. *Philosophical Transactions of the Royal Society A: Mathematical, Physical and Engineering Sciences*, 370(1960), pp.567–596.

Kinsler, L.E., Frey, A.R., Coppens, A.B., and Sanders, J.V., 2000. *Fundamentals of acoustics 4th edition*. New York, U.S.A.: John Wiley & Sons.

Lee, J.H.S., 2008. *The detonation phenomenon*. New York, NY: Cambridge University Press.

Lutz, A.E., Kee, R.J., and Miller, J.A., 1988. *SENKIN: A Fortran program for predicting homogeneous gas phase chemical kinetics with sensitivity analysis* (SAND87-8248). Livermore, CA: Sandia National Laboratories.

MathWorks, 2018. MATLAB (R2018a). [computer program] Available at: <https://www.mathworks.com> [Accessed 6 August 2018].

Pan, J., Shu, G., Zhao, P., Wei, H., and Chen, Z., 2016. Interactions of flame propagation, auto-ignition and pressure wave during knocking combustion. *Combustion and Flame*, 164, pp.319–328.

Parra, T., Castro, F., Méndez, C., Villafruela, J.M., and Rodríguez, M.A., 2004. Extinction of premixed methane-air flames by water mist. *Fire Safety Journal*, 39(7), pp.581–600.

Peters, N., Kerschgens, B., and Paczko, G., 2013. Super-knock prediction using a refined theory of turbulence. *SAE International Journal of Engines*, 6(2), pp.953–967.

Pipeline and Hazardous Materials Safety Administration, 2018. *Significant incident 20 year trend*. [online] Available at: <https://www.phmsa.dot.gov/data-and-statistics/pipeline/pipeline-incident-20-year-trends> [Accessed 26 July 2018].

Qi, C. and Chen, Z., 2017. Effects of temperature perturbation on direct detonation initiation. *Proceedings of the Combustion Institute*, 36(2), pp.2743–2715.

Qi, Y., He, X., Wang, Z., Wang, J., Zhang, H., and Jiang, Y., 2015a. An experimental investigation of super knock combustion mode using a one-dimensional constant volume bomb. *International Journal of Hydrogen Energy*, 40(5), pp.2377–2385.

Qi, Y., Wang, Z., Wang, J., and He, X., 2015b. Effects of thermodynamic conditions on the end gas combustion mode associated with engine knock. *Combustion and Flame*, 162(11), pp.4119–4128.

R Core Team, 2017. R: A language and environment for statistical computing. [computer program] Available at: <https://www.R-project.org> [Accessed 15 December 2017].

Rankin, B.A., Fotia, M.L., Naples, A.G., Stevens, C.A., Hoke, J.L., Kaemming, T.A., Theuerkauf, S.W., and Schauer, F.R., 2017. Overview of performance, application, and analysis of rotating detonation engine technologies. *Journal of Propulsion and Power*, 33(1), pp.131–143.

Rankine, W.J.M., 1870. On the thermodynamic theory of waves of finite longitudinal disturbance. *Philosophical Transactions of the Royal Society of London*, 160, pp.277–288.

Reynolds, W.C., 1986. *The element potential method for chemical equilibrium analysis: Implementation in the interactive program STANJAN version 3*. Stanford, CA: Department of Mechanical Engineering, Stanford University.

Robert, A., Richard, S., Colin, O., and Poinsot, T., 2015. LES study of deflagration to detonation mechanisms in a downsized spark ignition engine. *Combustion and Flame*, 162(7), pp.2788–2807.

Ryu, J.I., Shi, X., and Chen, J.Y., 2018a. Modes of detonation wave propagation in water vapor concentration gradients. *Manuscript submitted for publication.*

Ryu, J.I., Shi, X., and Chen, J.Y., 2018b. Numerical study of detonation propagation in fuel-stratifiaction layers. *Manuscript in preparation.*

Shi, X., 2017. *Fundamental processes in combustion of stratified mixtures.* Ph. D. University of California, Berkeley.

Shi, X., Chen, J.Y., and Chen, Y., 2017a. Laminar flame speeds of stratified methane, propane, and n-heptane flames. *Combustion and Flame*, 176, pp.38–47.

Shi, X., Chen, J.Y., and Chen, Z., 2016. Numerical study of laminar flame speed of fuel-stratified hydrogen/air flames. *Combustion and Flame*, 163, pp.394–405.

Shi, X., Ryu, J.I., Chen, J.Y., and Dibble, R.W., 2017b. Modes of reaction front propagation and end-gas combustion of hydrogen/air mixtures in a closed chamber. *International Journal of Hydrogen Energy*, 42(15), pp.10501–10512.

Smith, G.P., Golden, D.M., Frenklach, M., Moriarty, N.W., Eiteneer, B., Goldenberg, M., Bowman, C.T., Hanson, R.K., Song, S., William C. Gardiner, J., Lissianski, V.V., and Qin, Z., 1999. *GRI-Mech 3.0*. [online] Available at: <http://www.me.berkeley.edu/gri_mech/> [Accessed 14 May 2016].

Sućeska, M., 1999. Evaluation of detonation energy from EXPLO5 computer code results. *Propellants, Explosives, Pyrotechnics*, 24(5), pp.280–285.

Teodorczyk, A. and Benoan, F., 1996. Interaction of detonation with inert gas zone. *Shock Waves*, 6(4), pp.211–223.

Thomas, G.O., Edwards, M.J., and Edwards, D.H., 1990. Studies of detonation quenching by water sprays. *Combustion Science and Technology*, 71(4-6), pp.233–245.

Thomas, G.O., Sutton, P., and Edwards, D.H., 1991. The behavior of detonation waves at concentration gradients. *Combustion and Flame*, 84(3-4), pp.312–322.

Toro, E.F., Spruce, M., and Speares, W., 1994. Restoration of the contact surface in the HLL-Riemann solver. *Shock Waves*, 4(1), pp.25–34.

Turányi, T., 1997. Applications of sensitivity analysis to combustion chemistry. *Reliability Engineering and System Safety*, 57(1), pp.41–48.

Urtiew, P.A. and Oppenheim, A.K., 1966. Experimental observations of the transition to detonation in an explosive gas. *Proceedings of the Royal Society A: Mathematical, Physical and Engineering Sciences*, 295(1440), pp.13–28.

U.S. Energy Information Administration, 2017. *Electric power annual 2016*. Washington, DC: U.S. Department of Energy.

von Neumann, J., 1942. *Theory of detonation waves* (549). Washington, DC: Office of Scientific Research and Development.

von Neumann, J. and Richtmyer, R.D., 1950. A method for the numerical calculation of hydrodynamic shocks. *Journal of Applied Physics*, 21(3), pp.232–237.

Wang, Z., Liu, H., Song, T., Qi, Y., He, X., Shuai, S., and Wang, J., 2015a. Relationship between super-knock and pre-ignition. *International Journal of Engine Research*, 16(2), pp.166–180.

Wang, Z., Qi, Y., He, X., Wang, J., Shuai, S., and Law, C.K., 2015b. Analysis of pre-ignition to super-knock: Hotspot-induced deflagration to detonation. *Fuel*, 144, pp.222–227.

Xiao, J., Breitung, W., Kuznetsov, M., Zhang, H., Travis, J.R., Redlinger, R., and Jordan, T., 2017. GASFLOW-MPI: A new 3-D parallel all-speed CFD code for turbulent dispersion and combustion simulations Part II: First analysis of the hydrogen explosion in Fukushima Daiichi Unit 1. *International Journal of Hydrogen Energy*, 42(12), pp.8369–8381.

Yanez, J., Kuznetsov, M., and Souto-Iglesias, A., 2015. An analysis of the hydrogen explosion in the Fukushima-Daiichi accident. *International Journal of Hydrogen Energy*, 40(25), pp.8261–8280.

Ye, J., Chen, Z., Fan, B., and Xie, B., 2005. Suppression of methane explosions in a field-scale pipe. *Journal of Loss Prevention in the Process Industries*, 18(2), pp.89–95.

Zel'dovich, Y.B., 1940a. On the theory of the propagation of detonations on gaseous system. *Zhurnal Experimentalnoi i.Teoreticheskoi Fiziki*, 10, pp.542–568.

Zel'dovich, Y.B., 1940b. To the question of energy use of detonation combustion. *Zhurnal Tekhnicheskoi Fizik*, 10(17), pp.1453–1461.

Zel'dovich, Y.B., 1980. Regime classification of an exothermic reaction with nonuniform initial conditions. *Combustion and Flame*, 39(2), pp.211–214.

Zel'dovich, Y.B., Librovich, V.B., Makhviladze, G.M., and Sivashinsky, G.I., 1970. On the development of detonation in a non-uniformly preheated gas. *Astronautica Acta*, 15, pp.313–321.

Appendix A

Derivation of Chapman-Jouguet solution

To derive the Chapman-Jouguet solution, Equations 1.1, 1.2, and 1.3 are simplified as

$$\rho_b \left(D - u_b\right) = \rho_u D, \tag{A.1}$$

$$P_b + \rho_b \left(D - u_b\right)^2 = P_u + \rho_u D^2, \tag{A.2}$$

$$c_p T_b + \frac{\left(D - u_b\right)^2}{2} = c_p T_u + \frac{D^2}{2} + q. \tag{A.3}$$

A.1 Rayleigh line

The Rayleigh line can be derived from Equations A.1 and A.2. From Equation A.1,

$$D - u_b = \frac{\rho_u}{\rho_b} D, \tag{A.4}$$

and by substituting this into Equation A.2, Equation A.2 becomes

$$P_b + \rho_b \left(\frac{\rho_u}{\rho_b} D\right)^2 = P_u + \rho_u D^2,$$

$$P_b + \frac{1}{\rho_b} \left(\rho_u D\right)^2 = P_u + \rho_u D^2, \tag{A.5}$$

$$\left(P_b - P_u\right) = -\frac{1}{\rho_b} \left(\rho_u D\right)^2 + \rho_u D^2,$$

$$\left(P_b - P_u\right) = -\left(\rho_u D\right)^2 \left(\frac{1}{\rho_b} - \frac{1}{\rho_u}\right), \tag{A.6}$$

$$\left(P_b - P_u\right) = -\left(\rho_u D\right)^2 \left(v_b - v_u\right), \tag{A.7}$$

which is the same as Equation 1.5.

A.2 Hugoniot curve

The Hugoniot curve is obtained from Equations A.1, A.2, and A.3. As $c_pT = \frac{\gamma}{\gamma-1}Pv$, Equation A.3 becomes

$$\begin{aligned} \frac{\gamma}{\gamma-1}P_bv_b + \frac{(D-u_b)^2}{2} &= \frac{\gamma}{\gamma-1}P_uv_u + \frac{D^2}{2} + q, \\ \frac{\gamma}{\gamma-1}\left(P_bv_b - P_uv_u\right) + \frac{(D-u_b)^2}{2} - \frac{D^2}{2} &= q. \end{aligned} \tag{A.8}$$

Again, by substituting Equation A.4 into Equation A.8,

$$\begin{aligned} \frac{\gamma}{\gamma-1}\left(P_bv_b - P_uv_u\right) + \frac{1}{2}\left(\frac{\rho_u^2}{\rho_b^2}D^2 - D^2\right) &= q, \\ \frac{\gamma}{\gamma-1}\left(P_bv_b - P_uv_u\right) + \frac{1}{2}\left(\rho_u^2D^2\right)\left(\frac{1}{\rho_b^2} - \frac{1}{\rho_u^2}\right) &= q, \\ \frac{\gamma}{\gamma-1}\left(P_bv_b - P_uv_u\right) + \frac{1}{2}\left(\rho_uD\right)^2\left(v_b^2 - v_u^2\right) &= q. \end{aligned} \tag{A.9}$$

The Rayleigh line (Equation 1.5) gives an expression for $\left(\rho_uD\right)^2$ in terms of P and v:

$$\left(\rho_uD\right)^2 = -\frac{P_b - P_u}{v_b - v_u}. \tag{A.10}$$

Using this expression, $\left(\rho_uD\right)^2$ term can be eliminated from Equation A.9 as

$$\begin{aligned} \frac{\gamma}{\gamma-1}\left(P_bv_b - P_uv_u\right) - \frac{1}{2}\left(\frac{P_b - P_u}{v_b - v_u}\right)\left(v_b^2 - v_u^2\right) &= q, \\ \frac{\gamma}{\gamma-1}\left(P_bv_b - P_uv_u\right) - \frac{1}{2}\left(\frac{P_b - P_u}{v_b - v_u}\right)\left(v_b + v_u\right)\left(v_b - v_u\right) &= q, \\ \frac{\gamma}{\gamma-1}\left(P_bv_b - P_uv_u\right) - \frac{1}{2}\left(P_b - P_u\right)\left(v_b + v_u\right) &= q, \end{aligned} \tag{A.11}$$

which is identical with Equation 1.7.

A.3 Chapman-Jouguet condition

Both slopes of the Rayleigh line and the Hugoniot curve should be the same to have the Chapman-Jouguet (CJ) solution. Differentiating Equation A.11 or 1.7 with respect to v_b, the equation becomes

$$\begin{aligned} \frac{d}{dv_b}\left[\frac{\gamma}{\gamma-1}\left(P_bv_b - P_uv_u\right) - \frac{1}{2}\left(P_b - P_u\right)\left(v_b + v_u\right) = q\right], \\ \frac{\gamma}{\gamma-1}\left(\frac{dP_b}{dv_b}v_b + P_b\right) - \frac{1}{2}\left[\frac{dP_b}{dv_b}\left(v_b + v_u\right) + \left(P_b - P_u\right)\right] = 0, \end{aligned} \tag{A.12}$$

$$\begin{aligned}\frac{\gamma}{\gamma-1}\left(\frac{dP_b}{dv_b}v_b+P_b\right)&=\frac{1}{2}\left[\frac{dP_b}{dv_b}\left(v_b+v_u\right)+\left(P_b-P_u\right)\right],\\ \frac{\gamma}{\gamma-1}\left(\frac{dP_b}{dv_b}v_b+P_b\right)&=\frac{1}{2}\left[\frac{dP_b}{dv_b}\left(v_b+v_u\right)+\frac{\left(P_b-P_u\right)}{\left(v_b-v_u\right)}\left(v_b-v_u\right)\right].\end{aligned} \tag{A.13}$$

The slope of the Rayleigh line is simply $\frac{P_b-P_u}{v_b-v_u}$. By substituting $\frac{dP_b}{dv_b}$ for $\frac{P_b-P_u}{v_b-v_u}$ term in the right-hand side of Equation A.13, the CJ condition can be found as

$$\begin{aligned}\frac{\gamma}{\gamma-1}\left(\frac{dP_b}{dv_b}v_b+P_b\right)&=\frac{1}{2}\left[\frac{dP_b}{dv_b}\left(v_b+v_u\right)+\frac{dP_b}{dv_b}\left(v_b-v_u\right)\right],\\ \frac{\gamma}{\gamma-1}\left(\frac{dP_b}{dv_b}v_b+P_b\right)&=\frac{1}{2}\left[\frac{dP_b}{dv_b}\left(2v_b\right)\right],\\ \frac{\gamma}{\gamma-1}\left(\frac{dP_b}{dv_b}v_b+P_b\right)&=\frac{dP_b}{dv_b}v_b,\\ \left(\frac{\gamma}{\gamma-1}-1\right)\left(\frac{dP_b}{dv_b}v_b\right)&=-\frac{\gamma}{\gamma-1}P_b,\\ \left(\frac{\gamma-\gamma+1}{\gamma-1}\right)\left(\frac{dP_b}{dv_b}v_b\right)&=-\frac{\gamma}{\gamma-1}P_b,\\ \frac{1}{\gamma-1}\frac{dP_b}{dv_b}v_b&=-\frac{\gamma}{\gamma-1}P_b,\\ \frac{dP_b}{dv_b}&=-\gamma\frac{P_b}{v_b}.\end{aligned} \tag{A.14}$$

From Equation 1.5 or A.5, the slope of the Rayleigh line is $-\left(\rho_u D_{CJ}\right)^2$. Replacing $\frac{dP_b}{dv_b}$ in Equation A.14 with $-\left(\rho_u D_{CJ}\right)^2$, the condition becomes

$$\begin{aligned}-\rho_u^2 D_{CJ}^2&=-\gamma\frac{P_b}{v_b},\\ \rho_u^2 D_{CJ}^2&=\gamma\frac{P_b}{v_b}.\end{aligned} \tag{A.15}$$

Using the mass conservation equation (Equation A.1) and the relation, $\rho = 1/v$, it can be rewritten as

$$\begin{aligned}\rho_b^2\left(D_{CJ}-u_b\right)^2&=\gamma\frac{P_b}{v_b},\\ \frac{1}{v_b^2}\left(D_{CJ}-u_b\right)^2&=\gamma\frac{P_b}{v_b},\\ \left(D_{CJ}-u_b\right)^2&=\gamma P_b v_b.\end{aligned} \tag{A.16}$$

With the ideal gas law (Equation 1.4) and the sound speed relation, $a = \left(\gamma RT\right)^{1/2}$, the CJ condition can be deduced:

$$\left(D_{CJ}-u_b\right)^2=\gamma RT_b, \tag{A.17}$$

$$D_{CJ}-u_b=a_b. \tag{A.18}$$

A.4 Chapman-Jouguet properties

From Equation A.18 and A.1, the CJ detonation speed can be obtained as

$$D_{CJ} = \frac{\rho_b}{\rho_u} a_b, \tag{A.19}$$

or

$$D_{CJ} = \frac{\rho_b}{\rho_u} \left(\gamma R T_b\right)^{1/2}. \tag{A.20}$$

Then, Equation A.6 of the Rayleigh line becomes,

$$\begin{aligned}
\left(P_b - P_u\right) &= -\rho_u^2 \frac{\rho_b^2}{\rho_u^2} \left(\gamma R T_b\right) \left(\frac{1}{\rho_b} - \frac{1}{\rho_u}\right), \\
\left(P_b - P_u\right) &= -\rho_b^2 \left(\gamma R T_b\right) \left(\frac{1}{\rho_b} - \frac{1}{\rho_u}\right), \\
\cancel{P_b}\left(1 - \frac{P_u}{P_b}\right) &= -\gamma \cancel{\rho_b} \cancel{R T_b} \left(1 - \frac{\rho_b}{\rho_u}\right), \\
\frac{1}{\gamma}\left(1 - \frac{P_u}{P_b}\right) &= -1 + \frac{\rho_b}{\rho_u},
\end{aligned} \tag{A.21}$$

$$\frac{\rho_b}{\rho_u} = \frac{1}{\gamma}\left(1 - \frac{P_u}{P_b}\right) + 1. \tag{A.22}$$

As $P_b \gg P_u$ for a detonation wave, it can be approximated as

$$\frac{\rho_b}{\rho_u} \cong \frac{1}{\gamma} + 1. \tag{A.23}$$

T_b can be obtained by rearranging the energy conservation equation (Equation A.3) with the CJ condition (Equation A.18) as

$$\begin{aligned}
c_p T_b + \frac{\left(D_{CJ} - u_b\right)^2}{2} &= c_p T_u + \frac{D_{CJ}^2}{2} + q, \\
c_p T_b + \frac{a_b^2}{2} &= c_p T_u + \frac{D_{CJ}^2}{2} + q, \\
c_p \left(T_b - T_u\right) &= \frac{D_{CJ}^2 - a_b^2}{2} + q, \\
T_b - T_u &= \frac{D_{CJ}^2 - a_b^2}{2c_p} + \frac{q}{c_p}.
\end{aligned} \tag{A.24}$$

By replacing D_{CJ} using Equation A.19, it can be obtained that

$$\begin{aligned}
T_b - T_u &= \frac{\left(\frac{\rho_b}{\rho_u}\right)^2 a_b^2 - a_b^2}{2c_p} + \frac{q}{c_p}, \\
T_b - T_u &= \frac{a_b^2}{2c_p}\left[\left(\frac{\rho_b}{\rho_u}\right)^2 - 1\right] + \frac{q}{c_p}.
\end{aligned} \tag{A.25}$$

As $a_b^2 = \gamma R T_b$ and $R = c_p - c_v$, the equation becomes,

$$
\begin{aligned}
T_b - T_u &= \frac{\gamma R T_b}{2c_p}\left[\left(\frac{\rho_b}{\rho_u}\right)^2 - 1\right] + \frac{q}{c_p}, \\
T_b - T_u &= \frac{\gamma T_b}{2}\frac{c_p - c_v}{c_p}\left[\left(\frac{\rho_b}{\rho_u}\right)^2 - 1\right] + \frac{q}{c_p}, \\
T_b - T_u &= \frac{\gamma T_b}{2}\left(1 - \frac{1}{\gamma}\right)\left[\left(\frac{\rho_b}{\rho_u}\right)^2 - 1\right] + \frac{q}{c_p}, \\
T_b - T_u &= \frac{\cancel{\gamma} T_b}{2}\left(\frac{\gamma - 1}{\cancel{\gamma}}\right)\left[\left(\frac{\rho_b}{\rho_u}\right)^2 - 1\right] + \frac{q}{c_p}, \\
T_b &= \frac{T_b}{2}(\gamma - 1)\left[\left(\frac{\rho_b}{\rho_u}\right)^2 - 1\right] + \frac{q}{c_p} + T_u, \\
T_b &\left\{1 - \frac{\gamma - 1}{2}\left[\left(\frac{\rho_b}{\rho_u}\right)^2 - 1\right]\right\} = \frac{q}{c_p} + T_u, \\
T_b &= \frac{\frac{q}{c_p} + T_u}{1 - \frac{\gamma-1}{2}\left[\left(\frac{\rho_b}{\rho_u}\right)^2 - 1\right]},
\end{aligned}
$$

$$
\frac{T_b}{T_u} = \frac{\frac{q}{c_p T_u} + 1}{1 - \frac{\gamma-1}{2}\left[\left(\frac{\rho_b}{\rho_u}\right)^2 - 1\right]}. \tag{A.26, A.27}
$$

Then, with the detonation wave approximation as in Equation A.23, T_b can be estimated as

$$
\begin{aligned}
\frac{T_b}{T_u} &\cong \frac{\frac{q}{c_p T_u} + 1}{1 - \frac{\gamma-1}{2}\left[\frac{(\gamma+1)^2}{\gamma^2} - 1\right]}, \\
\frac{T_b}{T_u} &\cong \frac{\frac{q}{c_p T_u} + 1}{1 - \frac{\gamma-1}{2}\frac{\cancel{\gamma^2}+2\gamma+1-\cancel{\gamma^2}}{\gamma^2}}, \\
\frac{T_b}{T_u} &\cong \frac{\frac{q}{c_p T_u} + 1}{1 - \frac{2\gamma^2-\gamma-1}{2\gamma^2}}, \\
\frac{T_b}{T_u} &\cong \frac{\frac{q}{c_p T_u} + 1}{\frac{\cancel{2\gamma^2}-2\gamma+\gamma+1-\cancel{2\gamma^2}}{2\gamma^2}},
\end{aligned}
$$

$$
\frac{T_b}{T_u} \cong \frac{2\gamma^2}{\gamma + 1}\left(\frac{q}{c_p T_u} + 1\right). \tag{A.28, A.29}
$$

To calculate P_b, the Hugoniot curve (Equation A.11 or 1.7) can be rearranged as

$$\begin{aligned}
\frac{2\gamma}{\gamma-1}P_u v_u\left(\frac{P_b v_b}{P_u v_u}-1\right)-P_u\left(\frac{P_b}{P_u}-1\right)v_u\left(\frac{v_b}{v_u}+1\right)&=2q,\\
\frac{2\gamma}{\gamma-1}\left(\frac{P_b v_b}{P_u v_u}-1\right)-\left(\frac{P_b}{P_u}-1\right)\left(\frac{v_b}{v_u}+1\right)&=\frac{2q}{P_u v_u},\\
\frac{2\gamma}{\gamma-1}\left(\frac{P_b v_b}{P_u v_u}-1\right)-\frac{P_b v_b}{P_u v_u}-\frac{P_b}{P_u}+\frac{v_b}{v_u}+1&=\frac{2q}{P_u v_u},\\
\frac{2\gamma}{\gamma-1}\left(\frac{P_b v_b}{P_u v_u}-1\right)-\left(\frac{P_b v_b}{P_u v_u}-1\right)-\frac{P_b}{P_u}+\frac{v_b}{v_u}&=\frac{2q}{P_u v_u},
\end{aligned}\tag{A.30}$$

$$\begin{aligned}
\left(\frac{2\gamma}{\gamma-1}-1\right)\left(\frac{P_b v_b}{P_u v_u}-1\right)-\frac{P_b}{P_u}&=\frac{2q}{P_u v_u}-\frac{v_b}{v_u},\\
\frac{\gamma+1}{\gamma-1}\left(\frac{P_b v_b}{P_u v_u}-1\right)-\frac{P_b}{P_u}&=\frac{2q}{P_u v_u}-\frac{v_b}{v_u},\\
\frac{\gamma+1}{\gamma-1}\frac{P_b v_b}{P_u v_u}-\frac{P_b}{P_u}&=\frac{2q}{P_u v_u}-\frac{v_b}{v_u}+\frac{\gamma+1}{\gamma-1},\\
\frac{P_b}{P_u}\left(\frac{\gamma+1}{\gamma-1}\frac{v_b}{v_u}-1\right)&=\frac{2q}{P_u v_u}-\frac{v_b}{v_u}+\frac{\gamma+1}{\gamma-1},
\end{aligned}\tag{A.31}$$

$$\frac{P_b}{P_u}=\frac{\frac{2q}{P_u v_u}-\frac{v_b}{v_u}+\frac{\gamma+1}{\gamma-1}}{\frac{\gamma+1}{\gamma-1}\frac{v_b}{v_u}-1},$$

$$\frac{P_b}{P_u}=\frac{\frac{2q\rho_u}{P_u}-\frac{\rho_u}{\rho_b}+\frac{\gamma+1}{\gamma-1}}{\frac{\gamma+1}{\gamma-1}\frac{\rho_u}{\rho_b}-1}.\tag{A.32}$$

The approximation of P_b can be deduced from the ideal gas law with Equations A.23 and A.29:

$$\begin{aligned}
P_b&\cong\left(\rho_u\frac{\gamma+1}{\gamma}\right)R\left[\frac{2\gamma^2}{\gamma+1}\left(\frac{q}{c_p}+T_u\right)\right],\\
\frac{P_b}{P_u}&\cong\frac{1}{P_u}\left(\rho_u\frac{\cancel{\gamma+1}}{\cancel{\gamma}}\right)R\left[\frac{2\gamma\cancel{^2}}{\cancel{\gamma+1}}\left(\frac{q}{c_p}+T_u\right)\right],\\
\frac{P_b}{P_u}&\cong 2\gamma\frac{\rho_u R}{P_u}T_u\left(\frac{q}{c_p T_u}+1\right),\\
\frac{P_b}{P_u}&\cong 2\gamma\frac{\rho_u R}{\cancel{P_u}}\cancel{T_u}\left(\frac{q}{c_p T_u}+1\right),
\end{aligned}\tag{A.33}$$

$$\frac{P_b}{P_u}\cong 2\gamma\left(\frac{q}{c_p T_u}+1\right).\tag{A.34}$$

The detonation propagation speed, D_{CJ}, can be calculated using Equation A.20 with the above relation of T_b (Equation A.27) as

$$D_{CJ} = \frac{\rho_b}{\rho_u}\left\{\gamma R \frac{T_u\left(\frac{q}{c_p T_u}+1\right)}{1-\frac{\gamma-1}{2}\left[\left(\frac{\rho_b}{\rho_u}\right)^2-1\right]}\right\}^{1/2},$$

$$D_{CJ} = \frac{\rho_b}{\rho_u}\left\{\frac{\frac{q\gamma R}{c_p}+\gamma R T_u}{1-\frac{\gamma-1}{2}\left[\left(\frac{\rho_b}{\rho_u}\right)^2-1\right]}\right\}^{1/2},$$

$$D_{CJ} = \frac{\rho_b}{\rho_u}\left\{\frac{q\gamma\frac{c_p-c_v}{c_p}+a_u^2}{1-\frac{\gamma-1}{2}\left[\left(\frac{\rho_b}{\rho_u}\right)^2-1\right]}\right\}^{1/2}, \tag{A.35}$$

$$D_{CJ} = \frac{\rho_b}{\rho_u}\left\{\frac{q\gamma\left(1-\frac{1}{\gamma}\right)+a_u^2}{1-\frac{\gamma-1}{2}\left[\left(\frac{\rho_b}{\rho_u}\right)^2-1\right]}\right\}^{1/2},$$

$$D_{CJ} = \frac{\rho_b}{\rho_u}\left\{\frac{q\cancel{\gamma}\frac{\gamma-1}{\cancel{\gamma}}+a_u^2}{1-\frac{\gamma-1}{2}\left[\left(\frac{\rho_b}{\rho_u}\right)^2-1\right]}\right\}^{1/2},$$

$$D_{CJ} = \frac{\rho_b}{\rho_u}\left\{\frac{q\left(\gamma-1\right)+a_u^2}{1-\frac{\gamma-1}{2}\left[\left(\frac{\rho_b}{\rho_u}\right)^2-1\right]}\right\}^{1/2}. \tag{A.36}$$

From the approximated equations of ρ_b/ρ_u and T_b (Equations A.23 and A.29), the approxi-

mated detonation speed can be obtained as

$$
\begin{aligned}
D_{CJ} &\cong \left(\frac{\gamma+1}{\gamma}\right)\left\{\gamma R\left[T_u\frac{2\gamma^2}{\gamma+1}\left(\frac{q}{c_pT_u}+1\right)\right]\right\}^{1/2},\\
D_{CJ} &\cong \left[\frac{(\gamma+1)^{\cancel{2}}}{\gamma^{\cancel{2}}}\gamma RT_u\frac{2\gamma^{\cancel{2}}}{\cancel{\gamma+1}}\left(\frac{q}{c_pT_u}+1\right)\right]^{1/2},\\
D_{CJ} &\cong \left[2\left(\gamma+1\right)\gamma\left(c_p-c_v\right)T_u\left(\frac{q}{c_pT_u}+1\right)\right]^{1/2}, \qquad \text{(A.37)}\\
D_{CJ} &\cong \left[2\left(\gamma+1\right)\gamma\left(c_p-c_v\right)\frac{c_p}{c_p}T_u\left(\frac{q}{c_pT_u}+1\right)\right]^{1/2},\\
D_{CJ} &\cong \left[2\left(\gamma+1\right)\cancel{\gamma}\frac{\gamma-1}{\cancel{\gamma}}c_pT_u\left(\frac{q}{c_pT_u}+1\right)\right]^{1/2},\\
D_{CJ} &\cong \left[2\left(\gamma^2-1\right)c_pT_u\left(\frac{q}{c_pT_u}+1\right)\right]^{1/2}. \qquad \text{(A.38)}
\end{aligned}
$$

Appendix B

Derivation of wave reflection and transmission equations

B.1 Wave equation

When the material derivative can be approximated as the partial derivative, the general differential form of inviscid momentum conservation equation for acoustic wave can be simplified as

$$\rho \frac{\partial u}{\partial t} = -\frac{\partial P'}{\partial x}, \tag{B.1}$$

where P' is the acoustic pressure. The general form of acoustic pressure can be written as

$$P' = c_1 e^{i(c_2 t - c_3 x)}, \tag{B.2}$$

where c_1, c_2, and c_3 are constants. Note that $c_2/c_3 = a$, where a is the sound speed. By substituting Equation B.2 into Equation B.1, the momentum conservation equation becomes

$$\begin{aligned} \rho \frac{\partial u}{\partial t} &= -\frac{\partial}{\partial x}\left[c_1 e^{i(c_2 t - c_3 x)}\right], \\ \rho \frac{\partial u}{\partial t} &= i c_1 c_3 e^{i(c_2 t - c_3 x)}, \end{aligned} \tag{B.3}$$

$$\frac{\partial u}{\partial t} = \frac{i c_1 c_3}{\rho} e^{i(c_2 t - c_3 x)}. \tag{B.4}$$

Integration of Equation B.4 with respect to t yields

$$\begin{aligned} u &= \frac{i c_1 c_3}{\rho} \int e^{i(c_2 t - c_3 x)} dt, \\ u &= \frac{\cancel{i} c_1 c_3}{\rho} \left[\frac{1}{\cancel{i} c_2} e^{i(c_2 t - c_3 x)}\right], \\ u &= \frac{1}{\rho}\left(\frac{c_3}{c_2}\right)\left[c_1 e^{i(c_2 t - c_3 x)}\right], \end{aligned} \tag{B.5}$$

$$u = \frac{1}{\rho}\left(\frac{1}{a}\right)P'. \tag{B.6}$$

Equation B.6 can be rewritten using specific acoustic impedance as

$$u = \frac{P'}{I}. \tag{B.7}$$

B.2 Interface conditions

Assuming there is a interface between two fluid media, medium 1 and medium 2, at rest, and an acoustic wave propagates from medium 1 to medium 2 through the interface. Then, at the interface of two different fluid media, continuities of fluid velocity and acoustic pressure are valid:

$$u_I - u_R = u_T, \tag{B.8}$$

$$P'_I + P'_R = P'_T, \tag{B.9}$$

where u_I, u_R, and u_T are indent, reflected, and transmitted fluid speeds, respectively. Using Equation B.7, Equation B.8 becomes

$$\frac{P'_I}{I_1} - \frac{P'_R}{I_1} = \frac{P'_T}{I_2}, \tag{B.10}$$

$$\frac{P'_I - P'_R}{I_1} = \frac{P'_T}{I_2}. \tag{B.11}$$

Combining Equations B.9 and B.11 with $z = I_2/I_2$ to eliminate P'_T, the pressure reflection coefficient can be written as

$$\begin{aligned} \frac{P'_I - P'_R}{I_1} &= \frac{P'_I + P'_R}{I_2}, \\ z(P'_I - P'_R) &= P'_I + P'_R, \\ (-z-1)P'_R &= (1-z)P'_I, \end{aligned} \tag{B.12}$$

$$\frac{P'_R}{P'_I} = \frac{z-1}{z+1}. \tag{B.13}$$

Then, the pressure transmission coefficient can be deduced from Equations B.9 and B.13:

$$\begin{aligned} P'_I + \frac{z-1}{z+1}P'_I &= P'_T, \\ \frac{z+1+z-1}{z+1}P'_I &= P'_T, \\ \frac{2z}{z+1}P'_I &= P'_T, \end{aligned} \tag{B.14}$$

$$\frac{P'_T}{P'_I} = \frac{2z}{z+1}. \tag{B.15}$$